PROGRESS TOWARD TIME-RESOLVED X-RAY SPECTROSCOPY OF

METALLOPROTEINS

A Dissertation

Submitted to the Faculty

of

Purdue University

by

Scott C. Jensen

In Partial Fulfillment of the

Requirements for the Degree

of

Doctor of Philosophy

December 2018

Purdue University

West Lafayette, Indiana

THE PURDUE UNIVERSITY GRADUATE SCHOOL
STATEMENT OF DISSERTATION APPROVAL

Dr. Yulia N. Pushkar, Chair

      Department of Physics and Astronomy

Dr. Stephan Durbin

      Department of Physics and Astronomy

Dr. Sergei Savikhin

      Department of Physics and Astronomy

Dr. Ken Richie

      Department of Physics and Astronomy

Dr. Paul Muzikar

      Department of Physics and Astronomy

Approved by:

      Dr. John Finley

          Head of the Department of Physics and Astronomy

To parents who inspire curiosity, a wife who matches it and children who cherish it.

ACKNOWLEDGMENTS

TABLE OF CONTENTS

LIST OF TABLES

LIST OF FIGURES

ABBREVIATIONS

3-PGA	Two3-phosphoglyceric acid
ADP	Adenosine diphosphate
AIC	Akaike information criterion
ATP	Adenosine triphosphate
BIC	Bayesian information criterion
BSA	bovine serum albumin
DCBQ	2,6-dichloro-1,4-benzoquinone
DFT	density functional theory
DMSO	dimethyl sulfoxide
EDTA	ethylenediaminetetraacetic acid ENDOR
EPR	electron paramagnetic resonance
EXAFS	extended x-ray absorption fine edge structure
FRET	Forster resonance energy transfer
fs	femtosecond
FWHM	full-width half-maximum
G3P	glyceraldehyde 3-phosphate
HEPES	4-(2-hydroxyethyl)-1-piperazineethanesulfonic acid
KB mirrors	Kirkpatrick-Baez mirrors
NADP+	nicotinamide adenine dinucleotide phosphate
NADPH	reduced form of nicotinamide adenine dinucleotide phosphate
MES	2-(N-morpholino)ethanesulfonic acid
KMnO4	potassium permanganate
LCLS	Linac Coherent Light Source
Mn	manganese
μs	microsecond

ms	millisecond
Nd:YLF	neodymium-doped yttrium lithium fluoride
ns	nanosecond
OEC	oxygen evolving complex
PSII	photosystem II
PQ	plastoquinone
RT	room temperature
SBCA	spherically bent crystal analyzer
SEM	standard error of the mean
Si	silicon
Tyr_Z	tyrosine 161 in D subunit of photosystem II
UV-Vis	ultraviolet-visible light
XANES	x-ray absorption near-edge structure
XAS	x-ray absorption spectroscopy
XES	x-ray emission spectroscopy
XFEL	x-ray free electron laser

ABSTRACT

Jensen, Scott C. PhD, Purdue University, December 2018. Progress Toward Time-Resolved X-ray Spectroscopy of Metalloproteins. Major Professor: Yulia Pushkar.

Metalloproteins, or proteins with a metal ion cofactor, are essential for biological function of both lower and higher level organisms. These proteins provide a multitude of functions from molecular transport, such as the hemoglobin transport of oxygen, to biologically important catalytic processes. As an example case, photosystem II (PSII) is studied as a representative metalloprotein. It was chosen based on the potential impact in the energy sector due to its ability to perform water oxidation using solar based energy. Understanding mechanisms by which the Mn_4Ca cluster inside PSII, also known as the oxygen evolving complex (OEC), can store energy as redox equivalents for splitting water will be essential for future development of analogous artificial systems. By using time resolved x-ray spectroscopy, the electron structure of the metal in the protein was probed through the catalytic cycle. While the applications mentioned herein are based on PSII from spinach, the developments in time-resolved x-ray spectroscopy techniques are also applicable to other metalloproteins.

By creating a new x-ray spectrometer we were able to capture the difference in x-ray emission spectra between two compounds differing in a single metal bound ligand, i.e. Mn^{IV}-OH and Mn^{IV}=O. This both establishes the functionality of the x-ray emission spectrometer and provides useful insight into the expected changes upon an oxygen double bond formation. This change in spectroscopic signal is discussed in context of the OEC which has been hypothesized to form a Mn^{IV}=O state.

A new sample delivery system and further developments to the x-ray spectrometer enabled both time-resolved x-ray absorption and time-resolved x-ray emission of PSII. These experiments show the potential of synchrotron sources for time-resolved x-ray

spectroscopy. From our x-ray absorption measurements we were able to follow the electronic structure changes in time using a single incident photon energy. From the kinetic traces obtained, we show possible alternative interpretations of previous results showing a delay in reduction during the final step in water oxidation. From the x-ray emission spectroscopy (XES) measurements of PSII we were able to reproduce previous results within a limited collection time and give estimates for data size requirements for metalloproteins using this spectrometer. Between the results of both these measurements, we show the improved capability for time resolved measurements at synchrotrons.

The development of x-ray free electron lasers (XFELs) has also opened many opportunities for understanding faster electronic dynamics by providing femtosecond x-ray pulse durations with $\sim 10^{12}$ photons per pulse. While theoretical modeling of distortions to crystallographic data have been performed, little to no work has been done to understand under what conditions such an intense pulse will have on an impact on emission spectra. Here an atomistic model was developed, and data collected, to clarify the effects of sequential ionization, i.e. two single photons absorbed by the same atom at different times during a single pulse. Experimentally we found that XFELs easily achieve flux densities that invoke a different response than is classically observed for single photon absorption and emission for Mn^{II} which was used as a representative case for 3d transition metals in general. We also give parameters by which the onset of this damage can be predicted and an approximation to its effect on 3d transition metals. Additionally this work guides the work of future XFEL facilities as it shows that shorter pulses, currently believed to be able to escape x-ray induced distortions to crystallography data, is not a viable method for overcoming changes in x-ray emission spectra.

1. Overview

As the building blocks of life, proteins enact various functions to sustain life. Some proteins, called metalloproteins, incorporate a metal center to obtain catalytic function for biologically relevant reactions or for molecular transport. These reactions include, but are not limited to, the production of superoxides by the immune system, DNA synthesis, respiration in the mitochondria and photosynthesis. While the static structures for some of these metalloproteins have been obtained through x-ray crystallography, insights into dynamics are often needed to understand the mechanisms of action. Results from time resolved studies, therefore, are crucial for guiding biomimetic approaches. This leaves a need to understand the critical role of the metal center to determine the electronic structure changes necessary for it to carry out its biological function. Time resolved x-ray spectroscopy provides a unique tool for probing element specific metal center and tracking the spectroscopic signatures through time. On a broader scale, this thesis addresses the potential for time resolved room temperature measurements of metalloproteins using x-ray spectroscopy by answering the following:

1. What potential do synchrotrons pose for time resolved measurements of dilute metalloproteins?

2. Can a more effective solution be found to enhance sensitivity and to make time resolved spectroscopy a more routine technique?

3. How to determine the limitations to x-ray emission spectroscopy at x-ray free electron lasers and under what conditions does the traditional interpretation of spectra break down?

4. Are shorter pulses at x-ray free electron lasers able overcome x-ray induced changes to the emission spectra?

In this dissertation, the representative metalloprotein, PSII, is used. This protein is highly studied because of its importance in maintaining an oxgenated atmosphere and as a potential model for artificial based photoinduced water oxidation and hydrogen fuel production. An overview of photosynthesis, with a focus on the Kok cycle, is given in Chapter 2 where the different oxidation states, or S-states, are described. Each transition between S-states is triggered by photon absorption. This cycle involves a careful modulation of oxidation states and ligand types that leads to the most important step of O–O bond formation. From this specific metalloprotein we can also address the following questions:

1. Can time resolved measurements with high S-states advancement be achieved without a preflash (as is currently performed at XFEL sources)?

2. Is the lag seen in the S3-S0 transition of the OEC only explainable by a deprotonation event [1] or can other kinetic models fit the data?

To address all questions presented here, the work in the following chapters is based on x-ray emission and absorption spectroscopy (see Chapter 3) to achieve the following:

- Development of a custom x-ray emission spectrometer prototype (Chapter 4) and demonstrate it's capability (Chapter 5).

- Create a new sample delivery system and an improved spectrometer for time-resolved spectroscopy (Chapter 6)

- Measure the time resolved x-ray absorption spectroscopic signals of Mn in the OEC using the sample delivery system (Chapter 7).

- Record undamaged x-ray emission spectra of photosystem II at discrete time points using the instrumentation in Chapter 6 (Chapter 8).

- Measure time resolved x-ray emission spectra at a x-ray free electron laser source and develop a model to identify the regime where classical emission, or the single photon absorption and emission, interpretation breaks down (Chapter 9).

The results of this research are then reviewed in the conclusions of this document (Chapter 10).

2. Background

2.1 Photosynthesis

Photosynthesis is a process that occurs in plants, algae and cyanobacteria which uses water and light to convert carbon dioxide into sugar and molecular oxygen. This process is crucial in sustaining animal and plant life by converting solar energy into chemical energy and provides the majority of the atmospheric oxygen that is needed to sustain animal life.

Progress toward natural [2] and artificial replication of photosynthetic water splitting has shown potential that could make a large impact on the energy sector through production of hydrogen fuel. Hydrogen based fuel sources provide a renewable and clean energy source that can be stored long term [3, 4] with some storage methods showing promise to have up to $\sim$40% the energy density of gasoline [5]. This is of particular importance as the world becomes more energy dependent with an estimated 1.2% increase in power demands every year and over 75% of energy production coming from non-renewable sources [6].

To aid in the understanding of photosynthetic water splitting, the reactions are categorized into two sections: light dependent reactions and light independent reactions. The light dependent reactions are driven by photoabsorption within chlorophyll pigments to ultimately create the cellular energy molecules, adenosine triphosphate (ATP)and (nicotinamide adenine dinucleotide phosphate) NADPH. The light independent reactions use the energy stored from the light dependent reactions to use carbon dioxide to create sugar during the Calvin cycle.

2.2 Light Dependent Reactions and the Electron Transport Chain

The light dependent reactions are unique because of their ability to drive redox reactions and energy conversion via photoabsorption. This process begins with the chlorophyll pigments. Antenna chlorophyll, or chlorophyll a molecules in photosystem II, capture a photon and transfer the energy, in the form of excitation energy, between chlorophyll molecules through a resonant dipole-dipole interaction known as Förster Resonance Energy Transfer (FRET). As the energy transfers between chlorophyll it eventually finds its way to a chlorophyll dimer known as P680, or the special pair, within photosystem II (PSII). When this dimer receives energy through FRET or direct photoabsorption, it undergoes charge separation through an electron transfer (ET) event and the donated electron goes to a nearby acceptor, thus starting the electron transport chain. As an electron leaves P680 to follow the electron transport chain, tyrosine 161, Y_Z, in the D1 subunit of PSII donates an electron to fill the hole, becoming oxidized. The tyrosine is in turn reduced by the oxygen evolving complex or its surrounding ligands. The energy stored from these oxidation events is used to drive water splitting described in Section 2.2.2.

After the electron in the special pair is donated to pheophytin, it continues to follow the energetically favored transitions, see Figure 2.2, to Q_A then Q_B both of which are plastoquinones. The transfer process from Q_B does not continue until it has received two electrons from Q_A and two protons from the stroma, after which it is released into the quinone pool where it diffuses to cytochrome b6f complex to transfer the electrons. Here the protons are transported to the lumen side (see Figure 2.1) of the thylakoid membrane and one of the electrons is transferred to photosystem I via plastocyanin while the other goes to a plastoquinone bound to the stroma side of the cytochrome b6f where it collects another electron and two protons before entering the Q-pool.

The electron transported to PSI then receives more energy from the excited state of another special pair, P700, which was excited either by the transfer of energy

Electron Transport Chain
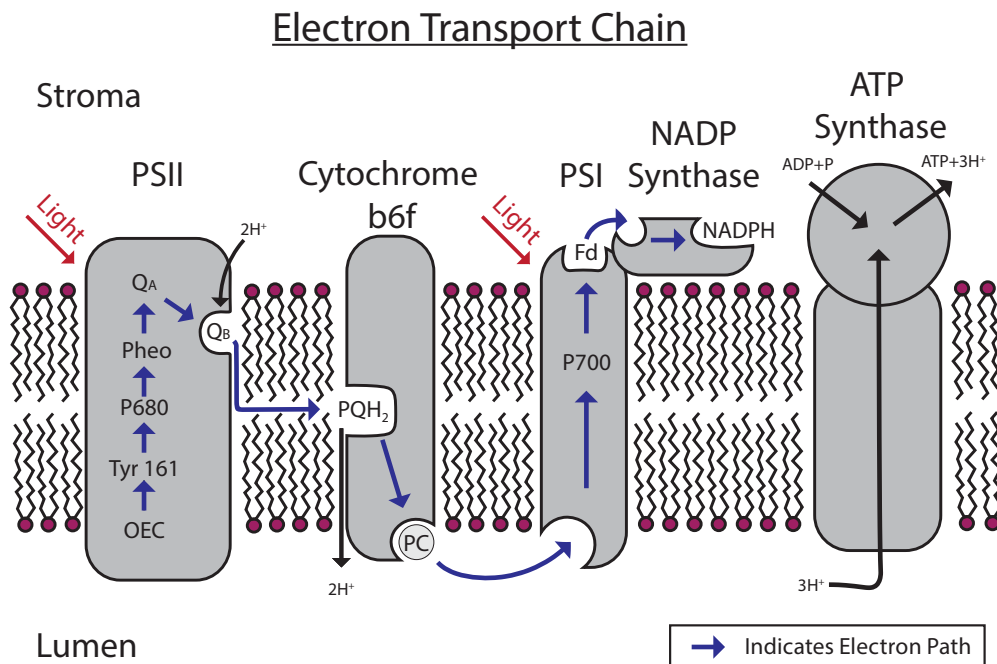
Figure 2.1. The electron transport chain is depicted with the electron starting with waters (not shown) in the OEC and follows the blue arrows to form NADPH. Light is also used at the locations of PSII and PSI which is depicted in red.

through FRET from the chlorophyll attached to PSI or direct absorption of light. The electron can then enter a cyclic transport where the excited electron is reused for creating a proton gradient across the thylakoid membrane, a process which has been suggested to be important for protecting the stroma from over reduction [7], or it can continue in the electron transport chain to ferrodoxin. After ferrodoxin the electron is used by a NADP reductase to reduce NADP and H+ to NADPH. As the protons travel through the proton pump across the concentration gradient to the stroma, part of the complex will rotate. The rotation process is used to drive the phosphorylation of ADP to ATP. The ATP and NADPH are then used in the light independent reactions.
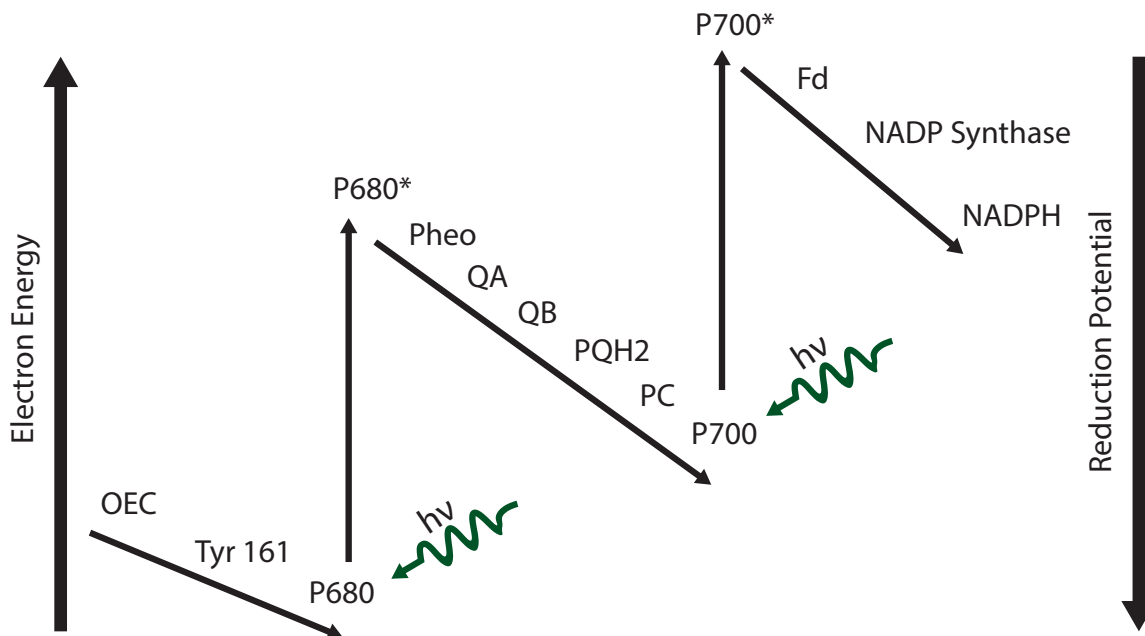
Figure 2.2. The Z-scheme is shown with the general trend of increasing reduction potential after each electron transition and a lower potential transition after photon absorption.

2.2.1 Light Independent Reactions

The light independent reactions together comprise the Calvin cycle. This cycle generates carbon-based chemical energy storage (carbohydrates) out of carbon dioxide, NADPH and ATP. For simplicity this cycle is split into three sub groups which are mentioned here in brief: carbon fixation, reduction and regeneration.

- During carbon fixation the carbon dioxide binds to ribulose 1,5-biphosphate (RuBisCo) creating a 6 carbon intermediate molecule. Two 3-phosphoglyceric acid molecules or 3-PGA, are formed after the newly formed complex breaks down.

- In the reduction phase ATP and NADPH are used to convert the 3-PGA molecules to glyceraldehyde 3-phosphate, G3P.

- Finally, 3 RuBisCo, Ribulose-1,5-bisphosphate carboxylase/oxygenase, molecules are regenerated from 5 G3P in the final stage using ATP to ADP conversion. The extra G3P created out of three carbon dioxide molecules will be used in a separate process to form sucrose, glucose, cellulose or another carbohydrates.

2.2.2 Oxygen Evolving Complex

The oxygen evolving complex (OEC) is a Mn cubane structure that enables water splitting during the photosynthetic process. Splitting water in this way was first reported to be a 4 step process with each accumulating additional charges in a trapping center [8]. The process became known as the Kok cycle and the trapping center was found to be the OEC. Although much progress has been made to improve the structural and electronic understanding of this system, many of the transitions or intermediates involved in water oxidation by the OEC reduction have not been identified. These transitions occur on a time scale of tens of microseconds to over a millisecond. Each transition is unique and provides insight into the mechanism of water splitting, di-oxygen formation and local energy storage.

The OEC cluster comprises four manganese (Mn) atoms, one calcium atom and several oxygen atoms in a cubane structure [9–11]. Within this complex and in the surrounding ligand environment, oxidation equivalents are stored for the splitting of water.

With the OEC as the catalyst, water is split into electrons, protons, and oxygen. The electrons are used to replace the electron given away by the reaction center special pair. The protons are used to generate ATP through ATP-synthase. The oxygen is contained, potentially as a ligand, until it can be released safely as diatomic oxygen after a series of four photoabsorption events. Kok first suggested the existence of five different states with four light induced oxidative transitions with the positive charge stored in a trapping center [8]. These states were denoted S states and are used to
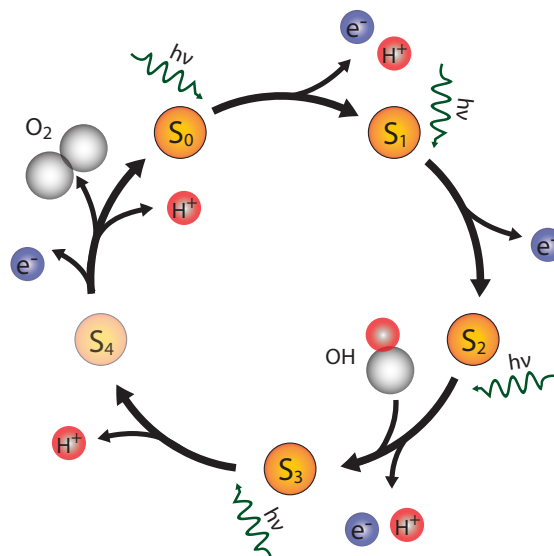
Figure 2.3. The Kok cycle with time transition times as measured by time resolved x-ray absorption with the S4 state partially faded to emphasize the unknown nature of the S3-S0 transition [1].

delineate the steps in the cycle where energy is stored within the oxygen evolving complex.

2.3   The S States

Below is a brief description of each of the different S-states. In each header is the respective S-state and the oxidation state of the Mn atoms in the OEC according to the high oxidation model (which is strongly supported by x-ray spectroscopy). Some of the x-ray spectroscopic techniques are mentioned here without description, for a brief introduction see Chapter 3. Many of the other S-state measurements have been done at low temperature to reduce damage or to freeze the sample in a particular state. This approach, though common, has be shown in some cases to give varying results from those of room temperature [12]. For this reason time resolved room temperature measurements are emphasized in this section. Additionally, diffraction models have

been obtained using x-ray free electron lasers (XFEL) for the S1 [9, 10, 13, 14], S2 [13] and S3 [10, 11, 14] states.

2.3.1   S1 - (Mn^{III}_2 Mn^{IV}_2)

Of the S-states S1 is the best characterized. This is mainly due to S1 being the dark adapted state, meaning when left in the dark all other S-states have been shown to transition back to this state [15]. Even S0, the most reduced state, transitions to S1 by oxidizing a nearby tyrosine. This allows for easier measurements since no laser pump is required to reach this state. This state is also the most pure state since almost all of the OEC's in a sample will be in this state, whereas with laser excitation double hits (two advancements) or misses (single absorption that leads to no advancement) will cause a convolution of states [16].

The oxidation state of the manganese atoms in the S1 state has been supported by several techniques including X-ray spectroscopy [17, 18]. Possible structure of the S1 state has been greatly narrowed by the seminal work of Umena et al. in 2011 where the structure of photosystem II from Thermosynechococcus volcanus was determined to a resolution of 1.9 angstroms [19]. This work showed that the Mn_4CaO_5 cluster makes a closed cubane structure with an additional Mn and O atom forming a back, much like the form of a chair. It also shows 2 substrates (assumed to be waters) on both the Mn4 and the Ca atoms with an oxygen binding the two metal centers (note that Mn and O atoms are numbered according to convention shown in Figure 2.4). While arguments have been made that the OEC is photoreduced due to x-ray damage, this was nonetheless an important discovery which allows a refined interpretation of other spectroscopic results.

Extended x-ray absorption measurements in particular have found that the bond distances were slightly different from those in the diffraction model, thus leading to some variations in the proposed structure [20]. A free electron laser was used to obtain what is reported to be a damage free diffraction patterns [13, 14, 21], which
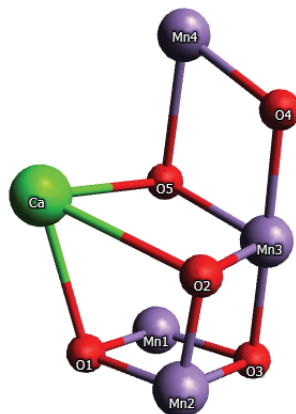
Figure 2.4. The approximate oxygen evolving complex structure as determined by Suga et. al. showing the open cubane and the dangle atoms for the S1 State [9].

were later obtained with a much higher resolution of 1.95 angstroms [9]. A more recent room temperature crystallographic structure at 3 angstroms obtained at an x-ray free electron laser source [10] did not find differences in structure with their lower resolution data, though the authors argue that the large Mn1-O5 distance indicates there is no bond so that the OEC is an open cubane. Alternatively, room temperature measurements in extended x-ray absorption fine structure (EXAFS) showed some variations in bond distances suggesting refinement may be necessary [22]. While some debate still exists on the bonding of the O5 atom, an equally important piece of missing information is about local protonation states of the OEC and protein. This information will hopefully be achieved in future work involving neutron diffraction.

2.3.2 S2 - ($Mn^{III} Mn^{IV}_3$)

After the first flash in dark adapted PSII, the oxidation state of one of the manganese atoms changes. This has been shown using the inflection point shift and spectral shape of the second derivative of the X-ray absorption near edge structure (XANES) for the Mn K-edge. Additionally, oxidation state changes in Mn has been shown with the first moment of the x-ray emission line $K\beta_{1,3}$ peak shift and difference

plots between the S1 and S2 states. The low dependence on pH and H2O/D2O exchange indicates that proton transfer is unlikely in this transition [23]. The structure is believed to be very similar to that of S1 in Mn-Mn bond distance as shown by EXAFS spectroscopy [24]. This state has an electron paramagnetic resonance (EPR) signal that has been used to define laser excitation turnover efficiency for each of the S-states [25]. It has also been used as an indication that the S2 state is in reality an inter-convertible state with the dangler Mn atom binding to an open cubane structure or a Mn atom dangling via a μ-oxo bridge to a closed cubane [26].

2.3.3 S3 - ($Mn^{III} Mn^{IV}_3$ or Mn^{IV}_4)

At this stage in the cycle the formal oxidation state of Mn is unclear. X-ray absorption (emission) spectroscopy have shown only slight changes in inflection point (first moment) that are on the order of $\sim 1/3$ that of the expected signal from an oxidation state change in one of the metal centers [17,18,20], though not all researchers agree [27]. Interpretation of the mixed x-ray spectroscopic results can be difficult in the case of the S2-S3 transition due to the strong changes in local structure, making the spectral positions susceptible to changes in coordination [28]. Both XANES and x-ray emission spectroscopy (XES) are shown to have some dependence on the ligand environment and coordination of the metal center which could explain the small shifts, see Chapters 3,5. Furthermore, experimental evidence of structural changes have been reported for the S2-S3 transition [20,29,30]. Complicating matters further, electron paramagnetic resonance (EPR) measurements have taken the opposite view, indicating a Mn centered oxidation does occur [31], thought this claim has not gone without dispute [32]. While unclear if Mn centered oxidation or ligand oxidation advancements in understanding this state continue to move forward. The structure in the S3 state has been captured using diffraction at a XFELs, where PSII protein crystals were exposed to 2 laser flashes and diffraction data was collected [10, 11, 14]. Young et al. has shown that the structure of the OEC is likely in an open

cubane structure [10] while a later diffraction model suggested an oxygen atom was incorporated near O5 [11, 33] between Mn4 and Mn1 (see Figure 2.4 for numbering assignment). This extra oxygen has long been predicted by Dr. Per Siegbahn using density functional theory (DFT) to show it's energetically favorable incorporation into the OEC [34]. This oxygen is important as it is likely involved in the formation of the O–O bond as discussed in Section 2.3.6.

2.3.4   S3-S0 Transition

The S3-S0 transition occurs on the ms time scale and is widely believed to include the formation of the O–O bond. It has also been reported that there is a lag in absorption changes for x-rays, ultraviolet (UV) and infrared (IR), which has been reported as a potential deprotonation event creating a transient state, S4, before oxygen release and Mn reduction [1, 23, 35, 36]. While there is still much unknown about this transition, it is clear that $Yz^{+\bullet}$ must be reduced and molecular oxygen formation must occur during this transition. Information regarding transition states and O–O bond formation mechanisms are highly sought after but remains fairly elusive due to it's transient nature.

2.3.5   S0 - ($Mn^{III}_3 Mn^{IV}$)

This state is the most reduced of the 4 states. While it is not the dark adapted state there are ways to force the OEC into this state and prevent advancement to the S1 state. While the S1 state is believed to be similar to S0, the S0 state has been shown to have a unique EPR signal [37] and one longer Mn-Mn bond distance than that of S1 [38]. The protonation state of the OEC or its ligand environment is also suggested to be altered since the S0-S1 transition is also believed to include a deprotonation event [39, 40].Support for the different oxidation state has also been presented [36].

2.3.6 Suggested Models for the O–O Bond Formation

One of the most important details of the Kok cycle is the formation of the O–O bond and ultimately O_2 release. This process has persistently eluded experimental scientific scrutiny in all but time resolved studies. While still highly debated, several models have been proposed to predict the location and mechanism of the O–O bond formation within the S3-S0 transition. Some of the main current models include nucleophilic attack or radical coupling. Nucleophilic attack involves the donation of an electron pair from one chemical species, nucleophile, to another, electrophile, to form bonding. As the Nucleophile and electrophile bond, the previous bonds the electrophile had are released. In the case of PSII, the nucleophile is an OH^- group that attacks an oxo ligand in the Mn cluster. While this mechanism has had some support [41], recent updates to structure allow for a more thorough DFT analysis which strongly opposes this mechanism [42].

Radical coupling is as it's name suggests and involves two chemical species with unpaired electrons. The electrons then form a bond between the two speicies. In the case of PSII, two oxygen radicals would come together to create a bond. While the locations of the O–O bond formation are still debated, recent reports of an additional oxo or hydroxyl group near the location of O5 [11, 33] is very suggestive. This oxygen is not present in S1 or S2 and is therefore incorporated at some point during the S2-S3 transition and is removed before reverting back to S1. Radical coupling between these two oxygens is therefore likely and has even been reported prior to the recent crystallograpic findings [43]. This is in agreement with previous findings using crystallographic data of ammonium substituted S3 state. There they showed that ammonium is likely taking one of the water locations around Mn3 but it still evolves oxygen. This suggests at least one of those is not involved in O–O formation. The location of the more favorable water binding locations indicate a water bound to Ca would react with O5 or a Mn4 would bind with O4 to create the O–O bond.

While most mechanisms address the S3 state in a particular configuration to advance, a more recent computational study based on previous time resolved x-ray emission studies and DFT [12] has shown that the S3 state could include an peroxo-isoform which was labeled S3OO [44]. This state was found to be energetically accessible for models with a Mn^{IV}=O formation in the S3 state.

2.3.7 Transition Times for the S-States

There have been several time-resolved measurements of the S-states and their associated time constants. This includes transient absorption of x-rays as a probe the Mn oxidation state [1], transient absorption of 295 nm ultra violet (UV) light measuring oxidation or electron transfer to the Tyrosine from the OEC [35], infrared (IR) absorption using 1400 and 2500 $cm^{-}1$ measuring vibrations of carboxylate groups and polarizable protons [45], and photothermal beam deflection measuring volume changes in PSII [46].

Table 2.1.
S-state kinetic time constants determined experimentally using a continuous x-ray probe for oxidation state changes in the OEC μs. PSII membrane fragments were used.

X-ray Absorption Spectroscopy							
Sample	S0-S1	S0-S1 Lag	S1-S2	S2-S3 Lag	S2-S3	S3-S0 Lag	S3-S0
pH 6.2^a [1]	<50		100		277	300	1612
pH 6.3^{ab} [47]	52(8)		89	26	317	153	1538
pD 6.3^{ab} [47]	66(6)		108	117	568	380	2208

^{a} These were the pH of the solution before 30% dehydration of samples.

^{b} Errors types were not explicitly stated and thereby excluded.

Table 2.2.
S-state kinetic time constants determined experimentally using a continuous UV probe for oxidation state changes in the OEC in μs. PSII membrane fragments were used except where otherwise noted. Errors given when reported.

Sample	S0-S1	S0-S1 Lag	S1-S2	S2-S3 Lag	S2-S3	S3-S0 Lag	S3-S0
pH 6.5 [48]	35		45		170	900	
pH 6.5^a [48]	42		55		180	3188	

^{a} PSII Core Complexes were used

Table 2.3.
S-state kinetic time constants determined by index of refraction changes upon light exposure (assigned to deprotonation and structural rearrangement) μs. PSII membrane fragments were used except where otherwise noted. Errors given in parenthesis as one standard deviation when reported.

Photothermal Beam Deflection							
Sample	S0-S1	S0-S1 Lag	S1-S2	S2-S3 Lag	S2-S3	S3-S0 Lag	S3-S0
pH 5.5 [46]		155(20)	105(10)	55(10)	300(F)	120(40)	1875(100)
pH 6.0 [46]		120(20)	95(10)	40(10)	290(F)	290(90)	1590(100)
pH 6.2 [46]		100(15)	95(10)	35(10)	270(90)	25(10)^a	1605(100)
pH 6.5 [46]		105(20)	90(10)	30(10)	280(F)	30(10)	1560(100)
pH 7.0 [46]		110(20)	90(10)	20(10)	270(F)	15(10)	1640(100)
pD 6.2 [46]	25(10)	255(40)	135(10)	150(20)	510(90)	425(90)	2030(100)

^{a} Also a 250 μs kinetic was inferred

3. Methodology

3.1 X-ray Sources

X-ray tubes were first invented over a century ago as the worlds first artificial x-ray source. While primitive in the beginning, x-ray tubes have become more powerful, delivering a higher photons flux than ever before. Other sources, such as synchrotrons and x-ray free electron lasers (XFELs), have also been developed and are the sources used for the work contained herein. As it is outside of the scope of this research to describe in detail how x-rays are generated at synchrotron or free electron laser sources, only a brief overview of these sources is described here. Parameters involved once the x-rays are delivered to the beamline are discussed in the experimental section of the corresponding chapters.

Synchrotron x-ray sources, and more recently XFELs, have far surpassed that of bremsstrahlung based x-ray tubes in many parameters important for spectroscopic measurements. These source can have a much higher monochromatic flux, pulse intensity and smaller divergence. These improvements have been characterized by one parameter, brilliance, which is defined as the flux per mm^2 per milliradian^2 of solid angle where photons are within a 0.1% bandwidth in photon energy, which can be written as

$$Brilliance = \frac{Photons\ in\ 0.1\%\ energy\ bandwidth}{mm^2\ mrad^2\ sec}. \tag{3.1}$$

The brilliance of x-ray sources has increased by more than 8 orders of magnitude over the last several decades and continues to increase. This is achieved through the different methods of generating x-ray pulses.

The Advance Photon Source (APS), a synchrotron at Argonne National Lab, uses a linear accelerator and a booster ring in order to accelerate electrons to high relativistic speeds of >0.99999999c (Lorentz factor of ~14,000). These energetic electrons,

7-GeV, are kept in a storage ring where they continue to travel in an approximately circular pattern with straight and bent trajectories. The bends in the circle are made of bending magnets which employ a strong magnetic field to change the trajectory of the electrons. The electrons that undergo this acceleration will radiate high energy photons in the form of x-rays. Downstream elements can then be used to collimate, monochromate, focus, and shape the x-ray beam before being delivered to the sample of interest. In addition to bending magnets, insertion devices are designed to create x-ray radiation in regions where it is unnecessary to steer the electrons in a different direction. Insertion devices are instead used in straight segments of the electron path and emit x-rays by forcing an electron to oscillate in strong alternating magnetic fields. This method of producing x-rays is preferred for many experiments as they often produce a higher photon brightness.

Free electron lasers employ a similar technology as that of the insertion device. An intense bunch of relativistic electrons radiate photons as they oscillate in the alternating magnetic fields. As the electric field from the emitted photons gets strong enough, electrons start to arrange themselves into small bunches at every half wavelength of emitted light. This bunching is a result of the force of the electric field from the x-rays on the electron. As the electrons bunch, the radiated x-rays become increasingly coherent and the electric field will amplify with the same frequency, narrowing the electron bunching further. This results in coherent x-rays in a very narrow energy range. Pulses from these sources can be ultrafast, on the order of 1-100 fs, and can be very intense, $>10^{12}$ photons/pulse.

3.2 X-ray Spectroscopy

Hard x-rays, or x-rays with an energy >5keV, have energies comparable to the core electron energy level for many atomic species. When an x-ray of sufficient energy is absorbed it can promote a core electron to an empty orbital or ionize it to the continuum (see Figure 3.1). The hole created can then be filled with another bound

electron and the release of energy in the form of a photon (fluorescence) or as another ionized electron (Auger decay).
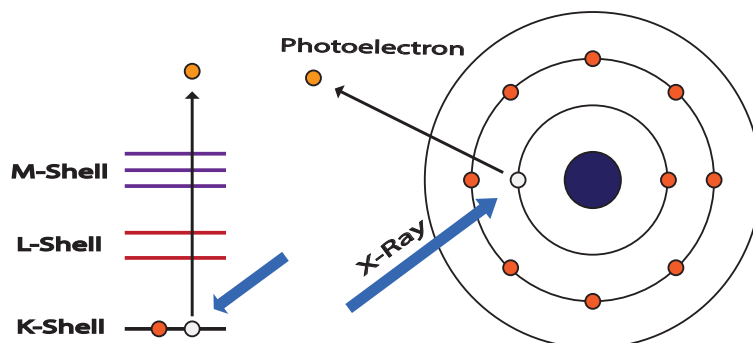
Figure 3.1. A pictorial version of core-hole ionization is given with shell energy levels (left) and the physical picture is also given (right) with the dark blue center representing a nucleus with orange electrons surrounding.

Two forms of x-ray spectroscopy are addressed, x-ray absorption spectroscopy (XAS) and non-resonant x-ray emission spectroscopy (XES). Interpretation of these techniques relies on the quantization of allowed electron energy levels around a nucleus. These energy levels are characteristic to each element and give rise to specific absorption edges and emission lines that can be used to probe the average electronic state of a specific element in the sample. Each one provides a different insight into the electronic structure surround the target atom.

The naming convention for the electron energy levels surrounding a positively charged nucleus is different in spectroscopy than that typically used in chemistry or physics. When referring to the principal quantum number of the system, n, the energy levels are not numbered but given letters starting with K and continuing through the modern English alphabet (e.g., n=1,2,3 relates to K, L, M respectively). This naming convention was created when x-ray fluorescence was first being characterized [49] and due to common usage, the nomenclature remains.

3.2.1 X-ray Absorption Spectroscopy

X-ray absorption is a photoexcitation process where a tightly bound electron, typically in the K or L levels, absorbs a photon and is either promoted to an unoccupied energy level or is completely ejected from the host atom. In x-ray absorption spectroscopy (XAS) the ratio of incident to x-rays absorbed by a sample is measured as a function of incident photon energy. This is either done directly by measuring transmission (see Figure 3.2), with a detector before and after the sample measuring photon flux, or indirectly by measuring a secondary process such as partial fluorescence yield or electron yield, where the incident photons are recorded and the number of photons/electrons emitted are used as a basis for x-ray absorption by the sample.
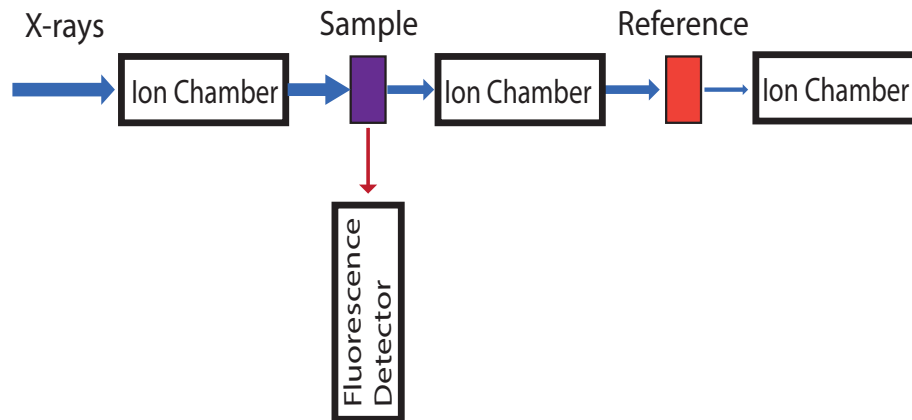
Figure 3.2. Diagram of the typical setup for a simple transmission setup with each of the ion chambers recording the number of x-rays passing through. Blue arrows indicate incident and transmitted x-rays, whereas the red arrow indicates x-ray fluorescence from the sample.

A typical transmission setup at a synchrotron beamline consists of gas proportional detectors before and after the sample to measure the number of incident and transmitted photons. The number of incident photons, I_0, and transmitted, I_t, can then be used in Beer's law,

$$I_t = I_0 e^{-\mu_{total}(E)x} \tag{3.2}$$

where $\mu_{total}(E)$ is the absorption coefficient and x is the sample thickness. The absorption coefficient can be written as

$$\mu_{total}(E) = \frac{1}{V} \sum_i (\sigma_i n_i) \tag{3.3}$$

where V is the volume of the sample being exposed to x-rays, σ_i is the atomic total absorption cross section $(cm^2/atom)$ of the element i at a given incident photon energy and n_i is the atomic density of the same element $(atoms/cm^3)$. This coefficient is then found in transmission as,

$$\mu_{total}(E)x = ln(I_0/I_t). \tag{3.4}$$

Note that this is valid when the thickness is constant throughout the measurement and the absorption coefficient changes with incident energy. In this case the equation can be written with the constant only depending on a normalization factor during processing, as the following proportionality

$$\mu_{total}(E) \propto ln(I_0/I_t). \tag{3.5}$$

This simple result is only valid for transmission measurements which are viable under a range of certain conditions. If the sample is not uniform, the sample is thick with a low concentration or if the sample is a thin concentrated sample, then using partial fluorescence yield measurement will often produce better results.

In a typical partial fluorescence yield measurement, the fluorescent signal is measured using an energy resolving detector instead of a gas proportional counter in transmission. This indirect approach assumes the number of x-rays absorbed by the target element is considered to be directly proportional to the number of fluorescent photons emitted. This proportionality can then be written in terms of absorption, or (I_0-I_t), such that

$$I_f \propto I_0 - I_t = I_0(1 - e^{-\mu_{total}(E)x}) \tag{3.6}$$

Now in the limit where $\mu(E)x << 1$, which is true for very thin samples, the exponential can be expanded using a Taylor series and keeping the first order term, the absorption becomes

$$\mu_{total}(E)x \propto I_f/I_0. \tag{3.7}$$

Here we can drop the constant sample thickness, x, as part of the proportionality

$$\mu_{total}(E) \propto I_f/I_0. \tag{3.8}$$

The same result of Equation 3.8 can be found for dilute thick samples for partial fluorescence yield measurements (after subtracting a slowly varying function) [50].

Both transmission and partial fluorescence yield measurements will depend to some degree on the absorption of the entire sample. The absorption from elements with that do not contain an absorption edge in the energy range used in XAS ($\Delta E \sim 1$keV) will have a nearly linear dependence on the incident energy. The decrease from these elements, and other factors in the proportionality of Equation 3.8, are approximated from the extended x-ray absorption fine structure (EXAFS) region and region before the edge or pre-edge. These values are used to subtracted a background and normalize the absorption spectra. The processed data will then closely reflect the absorption of the element of interest.

The change in the absorption coefficient versus incident x-ray photon energy gives rise to the absorption spectrum, shown in Figure 3.3. X-ray absorption spectra are evaluated in two regions, the x-ray absorption near-edge structure (XANES) region and the EXAFS region. The XANES region can have a pre-edge feature and also includes the rising edge, which result from electron promotion into an unoccupied orbital or to the continuum respectively. This region then continues past the ionization energy by 30-50eV and energies beyond that are considered to be in the EXAFS region. Both regions provide different information, and when recording EXAFS, typically both areas are measured.
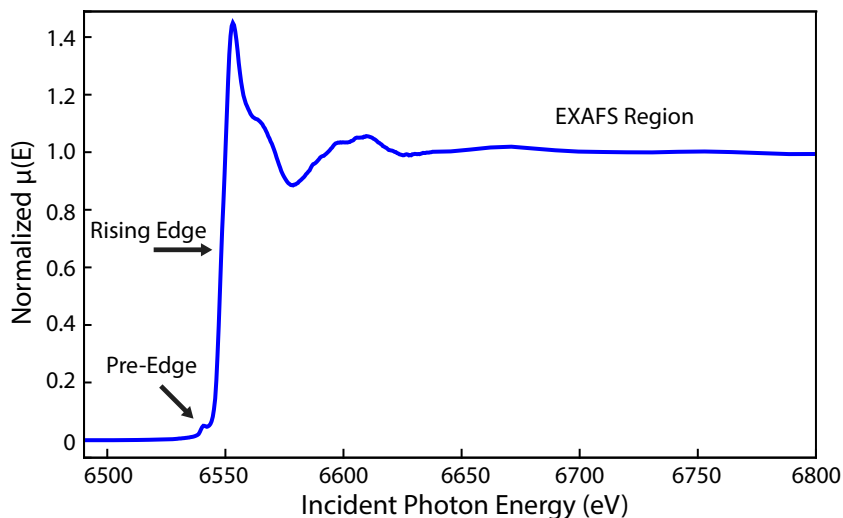
Figure 3.3. A background subtracted and normalized absorption spectra of $MnCl_2$ is shown with each of the main features labeled. Both the rising edge and the pre-edge are part of the XANES spectra.

3.2.2 XANES

The XANES region of the absorption spectrum consist of the pre-edge and rising edge features shown in Figure 3.3. The pre-edge feature for the first row transition metals can include a transition between the $1s$ to the $3d$ orbital when exciting the K-edge. The normal dipole selection rule, $\Delta l = \pm 1$, doesn't allow this transition but a quadrupole excitation, $\Delta l = \pm 2$, does. Since quadrupole transitions are much less likely to occur, the intensity of this feature is about 2 orders of magnitude weaker. This amplitude difference can be compensated for by distortions to the isolated atomic orbitals such as metal d-orbital mixing with s and p ligand orbitals, which will provide some dipole-allowed contribution [51].

Once the incident photon energy is sufficiently high, dipole allowed transitions become possible. For the first row transition metals it can be seen that from the $1s$ transition the electron can enter into unoccupied $4p$ orbitals or other higher states until the electron is so weakly interacting with the system that it will be ejected into

the continuum. At this energy there is a large rise in the x-ray absorption due to the metal atom which forms a feature known as a white line or absorption edge which exhibits a sharp rise in absorption.

Both the pre-edge and edge features can be used as an estimate of the average oxidation state of an element in the sample. When a 3d transition metal is ionized (i.e. loses a valence electron) the core electrons become more tightly bound to the atom due to the reduced electron repulsion but equal positive charge, raising the amount of energy needed to ionize the electron. These changes can be analyzed using the shift in position of the rising edge in comparison to similar compounds of known oxidation states [52]. This is an easy and quick analysis, though not always accurate since there are more factors involved than oxidation state alone that affect the electronic energy levels. Modeling of pre-edges, though more difficult, can be used to identify additional information such as bonding characteristics and coordination number [53].

3.2.3   EXAFS

In the EXAFS region the electron can be used to probe the local structure around the element of interest. When an x-ray is absorbed it will scatter off neighboring atoms creating interference between it and the initial outgoing wave. These changes in absorption will show up as oscillations in the extended region of the absorption spectrum. These changes can be plotted as the EXAFS function,

$$\chi(E) = \frac{\mu(E) - \mu_0(E)}{\Delta\mu_0(E_0)} \tag{3.9}$$

where $\mu(E)$ is the experimental values for the absorption coefficient, $\mu_0(E)$ is the absorption of an isolated atom (fit as a smooth function), and $\Delta\mu_0(E_0)$ is the "edge jump" which is the change in the total absorption before and after the rising edge.

The x-ray absorption coefficient for a particular atom can be modeled using the probability of absorption. The probability, obtained from Fermi's golden rule, models the probability of quantum transitions given a time dependent Hamiltonian to a new steady state (e.g. absorption of a photon to create a core hole and a photoelectron).

A full derivation of the EXAFS equation is not given here, the reader may refer to another reference for an in depth discussion of the equation [54].

As the EXAFS equation is dependent on the wave number of the photoelectron, k, we define this value in terms of the kinetic energy of the electron as,

$$k = \sqrt{\frac{2m_e(E - E_0)}{\hbar^2}} \tag{3.10}$$

where E_0 is the ionization energy, E is the energy of the absorbed photon, m_e is the mass of the electron and $\hbar$ is the reduced Planck's constant. The theoretical EXAFS equation is then given as a model with fit parameters as follows,

$$\chi(k) = S_0^2 \sum_i \frac{N_i f_i(k)}{k R_i^2} e^{-2k^2\sigma_i^2} sin(2kR_i + \delta_i(k)) \tag{3.11}$$

where $S_0{}^2$ can be thought of as the overlap between the spectator electron initial and final state, N_i atoms at radius R_i involved in the photoelectron scattering and incorporates the probability of scattering off N atoms and with re-absorption f_i(k). It also accounts for phase changes corresponding to scattering off a nearby atom δ_i(k) and σ_i is the mean atomic displacement.

Models for the atomic structure are then used as initial guesses for finding the best fit to the parameters in the EXAFS equation. The fit can then refine models based on the statistical support for the bond distances and atoms used in the fit.

3.2.4 X-ray Emission Spectroscopy (XES)

X-ray emission spectroscopy is very similar to that of absorption spectroscopy except XANES information comes from transitions to the unoccupied electron states and XES provides information based on transitions from the higher occupied levels. This can be seen in Figure 3.4 where it shows a core-level electron being excited to an unoccupied state or the continuum (absorption) and relaxation of a $2p$ or $3p$ electron into the hole made during absorption (emission). The electron relaxation into a lower energy hole can cause fluorescence which is measured for emission spectroscopy. Non-resonant XES uses incident photons well above the ionization energy of the absorbing

electron to create the core hole. Resonant inelastic x-ray scattering (RIXS) occurs when the electron is only promoted to an unoccupied state. This means that the probed electronic system is left in an excited state of equal energy to the photon since an electron was not emitted during this process. The final state in RIXS is similar to that of the initial only with a small amount of energy and momentum transferred to the system.

3.2.5   Non-Resonant XES

Non-resonant XES occurs after core hole ionization during electron filling of the core hole. An example case for K-shell ionization is shown in Figure 3.4.
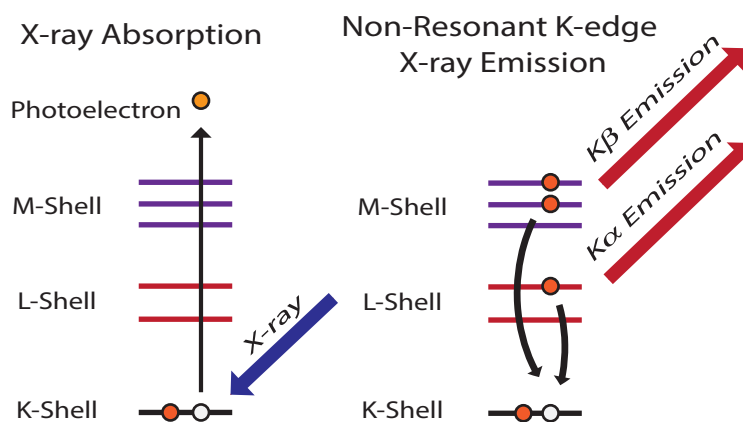
Figure 3.4. Core-hole ionization is given with shell energy levels (left) and the resulting fluorescing transition (right).

The most common fluorescence pathway involves a $2p$ electron to fill the hole which results in $K\alpha$ emission lines. For $3d$ transition metals the $K\beta_{1,3}$ and $K\beta$' emission lines can also occur and involve a $3p$ electron filling the core hole, where these $K\beta$ lines together are the mainlines. These lines are indirect measures of the valence $3d$ electrons through an exchange interaction which causes the splitting between the two mainlines depending on the spin of the electron undergoing a transition from the $3p$

to the $1s$ and the total spin of the $3d$ electrons. When the spin of the electron in the initial $3p$ state is parallel to the $3d$ electrons a Kβ' emission is observed otherwise, in the antiparallel case, K$\beta_{1,3}$ is emitted. If the state (high or low spin) of the system is known, then the oxidation state can be estimated indirectly from the splitting of these two emission lines. Example of the emission lines is shown in Figure 3.5.
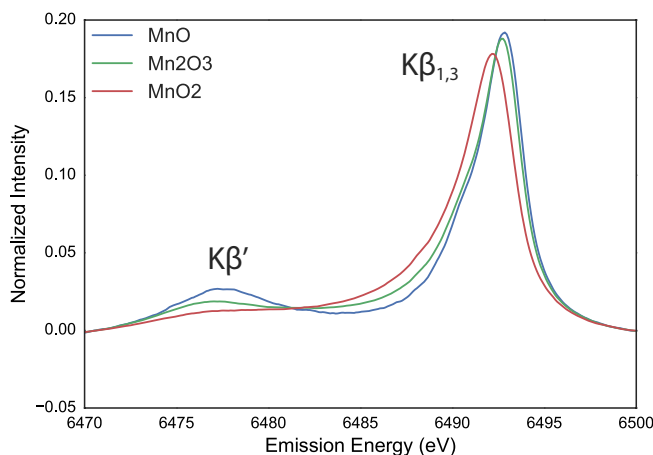
Figure 3.5. Emission spectra of Mn Oxides with the K$\beta_{1,3}$ and Kβ' emission lines shown.

For direct measurement of the valence electrons in $3d$ transition metals the valence-to-core, or satellite peaks, K$\beta_{2,5}$ and Kβ" can be recorded. The lines reflect the emission from an electron transitioning from the $3d$ to $1s$ which, as a dipole forbidden transition, are much weaker that the other lines. When ligands are present on the central transition metal, the orbitals will mix making these lines direct probes to orbital mixing and ligand types [55]. This is particularly useful for low Z element ligands such as O, C, and N where other methods, such as EXAFS and diffraction are limited. For ligand transitions, the K$\beta_{2,5}$ and Kβ" correspond to $1s$ filling from ligand p or ligand s orbitals respectively [56]. While all Kβ emission lines are important for spectroscopic tools, the Kβ mainlines are approximately 100 fold more probable than that of the satellite transitions. This limitation of the valence to core transition can

exclude certain systems since the signal will be lower than the detection limit. This is the case for time-resolved measurements of photosystem II.

The analysis of the Kβ mainlines can be difficult and a variety of approaches have been taken. For a simple oxidation analysis, other contributing factors to the fluorescent lines are usually ignored, and effects of the spin state on the peak position or the first moment of the K$\beta_{1,3}$ can be analyzed. The first moment is defined as

$$First\,Moment = \frac{\sum_i E_i I_i}{\sum_i I_i} \tag{3.12}$$

where E$_i$ and I$_i$ are the emission energy and intensity at each point i respectively.

The peak position or first moment is generally compared to standards and model compounds. Since the splitting between the two mainlines is dependent on the net spin of the 3d electrons, a high-spin system undergoing oxidation will lower in spin and reduce the spacing between the two lines. This means the K$\beta_{1,3}$ first moment will shift to lower energy and can give semi-quantitative information on oxidation state changes. Additionally, an alternative method involves using a standard of a known spin and comparing the integrated absolute difference (IAD) [57] between the spectra from an unknown and known sample. As it's name suggests, this is done by simply summing of the absolute value of the residuals between the sample of interest and a standard, or itself in a dynamic case, with the area of consideration is normalized to unity for all data sets. A linear scale can then be made with other spin state compounds (usually oxides) using the same standard to obtain IAD values for each compound. A linear trend is then made with the IAD values and know spins. An estimate the nominal spin of the unknown compound is then found given the function of the linear fit. While these methods are more reliable than those of XANES estimation of oxidation state, the emission lines are still affected by factors other than $3d$ spin alone. Shifts have been observed from structural changes, covalency and ligand types, though these shifts are often small in comparison to an oxidation-induced shift while XANES has been shown to have large shifts due to both oxidation and structure [55, 58].

3.2.6 X-ray Emission Spectroscopy at XFEL Sources

An x-ray free electron laser (XFEL) source differs from that of the more conventional synchrotron source in that the temporal resolution of the pulse is on the order of fs and each pulse contains $\sim 10^{12}$ photons. These shorter pulses have enabled crystallography measurements of nanocrystals [59] with the hopes of moving to large single particle reconstruction [60]. More relevant for this work, fundamental process such as electron transfer, bond dynamics and chemical reactions have also been studied [61–64]. While one could envision both XAS and XES being undertaken at XFEL sources, the uncertainty in the incident photon energy makes XAS a much more challenging measurement. Non-resonant XES on the other hand, is not dependent on the excitation energy and can circumvent these issues making it the prevalent measurement type at these facilities.

XES conducted at XFEL sources can result in a number of processes not achievable at synchrotron sources. For synchrotron sources, the process of non-resonant XES is that which is described in the previous section. This occurs when a single electron is ionized through photoabsorption and the hole created is filled by a nearby electron with more energy during photoemission. This process is referred to as **classical** XES in this document for clarity. This process is typically used for understanding the electronic structure surrounding a metal center. Beyond the classical x-ray emission spectra, non-linear effects are also achievable at XFEL sources which can give completely different information or cause spectroscopic misinterpretation. Some of these effects include:

- Sequential photoabsorption: Multiple single photon absorption events by a single atom [65].

- Electron cascade effects: Electrons freed during x-ray exposure interact with other electrons cause secondary ionization.

- Stimulated emission: A population inversion is created in a core orbital through x-ray ionization. Normal emission is then amplified as the emitted x-rays cause stimulated emission in the surrounding atoms [66–68].

These processes are a subset of nonlinear effects found [21, 69–78] but are the main ones considered for this research. Such effects allow new, previously unattainable states and interactions with matter to be studied experimentally, however, they also illustrate the difficulty in appropriately interpreting spectroscopic results.
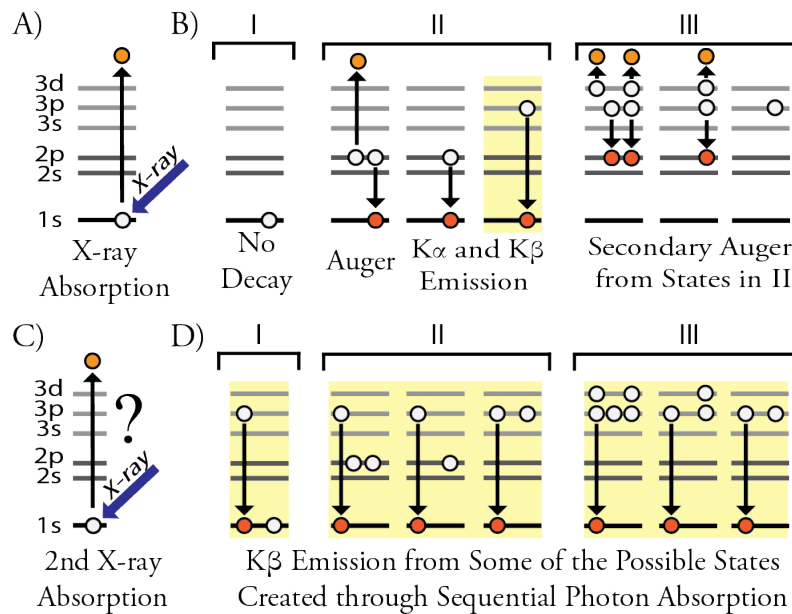
Figure 3.6. The sequential single photon absorption in the K-shell of a transition metal is depicted. A) Core-hole ionization via x-ray absorption, B) possible electron configurations based on time A and C with I) no relaxation, II) 1s decay, III) 2s and 2p decay, C) absorption event with possible electronic configurations represented by the question mark and shown in B), and D) Kβ emission in the presence of many possible electronic configurations. Note that only a subset of possible configurations are shown for Auger transitions and that for pulse durations used in this dissertation, B-III are most likely configurations to occur.

For the atomistic model of sequential photoabsorption see Figure 3.6. Depicted is an atom absorbing a photon, potentially undergoing electronic relaxation (referred

to as electronic decay, or just decay, in this dissertation), absorbs another photon then undergoes relaxation. In this figure only Kβ decay is shown during the second decay for clarity since this is the signal we record. The Kβ measured is then shown in the presence of several ionization states depending on the decay pathway and time between the two absorption events. Each of these configurations will result in a different spectroscopic signature, leading to a convoluted sum of final states.

4. An X-ray Emission Spectrometer Design

4.1 Introduction

To obtain high-quality emission spectra, a high energy resolution detection system must be used. In the ideal case both the collection and energy discrimination could be done by the detector. Currently, energy resolving detectors, such as silicon drift detectors, only have an energy resolution of $\sim$100 eV for hard x-rays and most area detectors are much worse. To overcome this limitation, superconducting detectors [79] are being developed to obtain $\sim$2 eV but these detectors are limited in availability, detector element size, count rates and overall detector size. Because of these limitations in current x-ray detector design, an x-ray spectrometer is required to spatially separate photons by energy before they are recorded by a detector. For high energy x-rays this can be done using Bragg reflections off a crystal surface, following Bragg's law.

$$\sin(\theta) = \frac{n\lambda}{2d} \tag{4.1}$$

where θ is the angle from the crystal plane to the incident photon direction, n is a positive integer and λ is the x-ray wavelength.

There are two main types of x-ray spectrometers: scanning and dispersive. The ideal scanning crystal, Johansson [80], is a spherically bent crystal analyzer which has a lattice bent to a radius of 2R but the surface is ground to a radius of R. Here the radius R is the radius of what is known as the Rowland circle. When a point source is located on the Rowland circle, all the x-rays will diffract off each point of the analyzer with the same Bragg angle and focus on the opposite side of the circle where they can be recorded (see Figure 4.1). In this way, a scanning optic can focus a very tight range of photon energies to a small spot. The optic is then scanned to reflect different Bragg angles to create a full spectrum from the fluorescent x-rays.
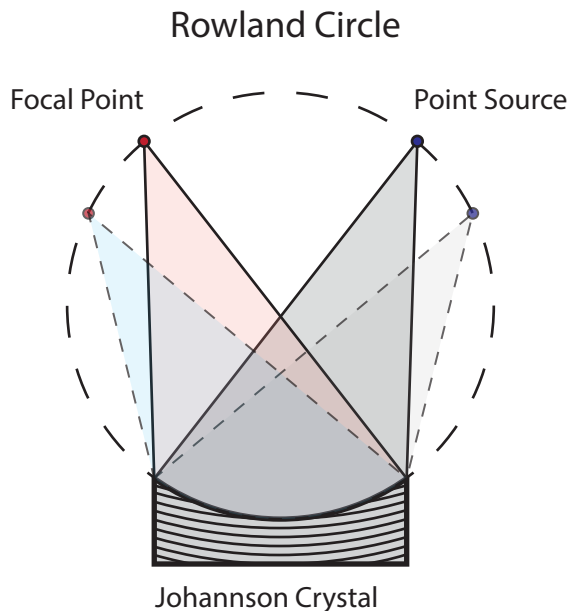
Rowland Circle

Figure 4.1. Two different point sources on the right side of the Rowland circle. The lines from each source simulate ray tracing of the emitting x-rays where all rays from a single point will all have the same angle relative to the 2R lattice plane of of the Johansson optic. Due to Bragg's law all x-rays will be of the same energy and, by design of the curved surface, the x-rays will also focus onto a single point on the other side of the Rowland circle (which has radius R).

A Johann optic [81] is similar to the Johansson except the lattice and surface both have a radius of 2R. This leads to a wider range of energies reflected onto the detection surface decreasing the energy resolution of the system. This deficiency can be overcome by using diced crystals which follow a simulated curve by using the dispersive separation of energy of each diced segment [82].

The spherically bent analyzers generally have high background rejection because of the tight focal point with apertures and typically large radius of curvature which increases the path length and decreases scattered x-rays. The large working distances of these analyzers ($\sim$0.5-10m radius) also have the advantage of improving the energy resolution. One major disadvantage when using crystals in scanning mode in time resolved studies is that a full energy spectrum cannot be recorded at the same instance

in time. This forces a larger number of repeated measurements for each time point recorded. Any shot to shot variations will also affect the generated spectra distorting the emission data making this approach less than ideal.

In the dispersive geometry, a spectrometer will spatially separate the entire collected energy range onto a position sensitive x-ray detector which can then be converted to a spectrum. In the simple case of a single flat crystal can be used to separate the photons by energy [83], though it is inefficient at fluorescence capture and leaves little room for apertures to reduce background. A more common and practical design is based on the von Hamos geometry [84]. A von Hamos analyzer consists of a cylindrically curved crystal which diffracts x-rays of different energies along the unbent width of the crystal and focuses in the curved direction (see Figure 4.2). This is similar to the flat analyzer except the curved surface will focus all x-rays of a single energy to a single point along the spectral line on the detection surface. This design allows for a full spectrum to be recorded simultaneously on a shot-by-shot basis.

A variation of the typical cylindrically bent von Hamos design is a diced, or segmented [85], von Hamos geometry. Such a design is very similar only the diffracting crystal is not bent to a cylindrical shape, instead the cylindrical surface is approximated stepwise with flat strips. This design has the benefit of avoiding any localized strain or imperfections during the bending process of the wafer, leading to an increased resolution. Unfortunately, there will also be a small loss in solid angle from the spacing between the diced strips of wafer as well as an increased spectral line focus which will be approximately twice the width of the diced strips.

4.2   Theoretical Energy Resolution (von Hamos)

The theoretical energy resolution is approximated as the full-width half-maximum (FWHM) of the energy distribution recorded in each energy bin used in the spectrum. For a von Hamos spectrometer detection system, this is generally calculated with three different sources of error, namely the Darwin rocking curve, the sample/x-ray inter-
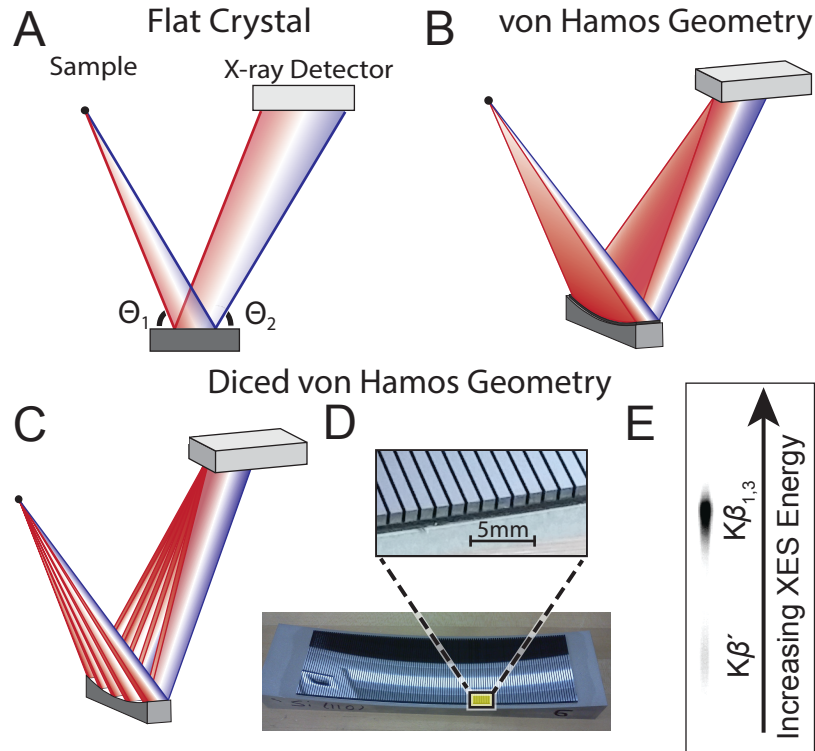
Figure 4.2. X-ray dispersive analyzers are shown as (A) a flat crystal, (B) the cylindrically curved von Hamos geometry with the characteristic focal line, and (C) a diced von Hamos analyzer with the final focal width twice the crystal strip width. (D) A diced von Hamos analyzer fabricated in our lab with a 1 mm strip width and (E) the recorded Pilatus image from MnO.

action spot size and the detector pixel width. Note that there is some inconsistency in some of the equations reported in literature [85–88]. Here these contributions are presented individually with clear definitions. An additional error term associated with diced crystals is also discussed.

Each of the different contributions is first found in terms of a range of Bragg angles, then combined as uncorrelated errors to obtain the total error,

$$\Delta\Theta_{Total} = \sqrt{\Delta\Theta^2_{Darwin} + \Delta\Theta^2_{Spot} + \Delta\Theta^2_{Det} + \Delta\Theta^2_{Diced}} \qquad (4.2)$$

where $\Delta\Theta_{Total}$ is the FWHM of the angular resolution, while $\Delta\Theta_{Darwin}$, $\Delta\Theta_{Spot}$, $\Delta\Theta_{Det}$ and $\Delta\Theta_{Diced}$ are the Darwin rocking curve, spot size, detector pixel size and diced crystal contributions respectively. The combined angular range is used in Bragg's law to find the equivalent range of energy.
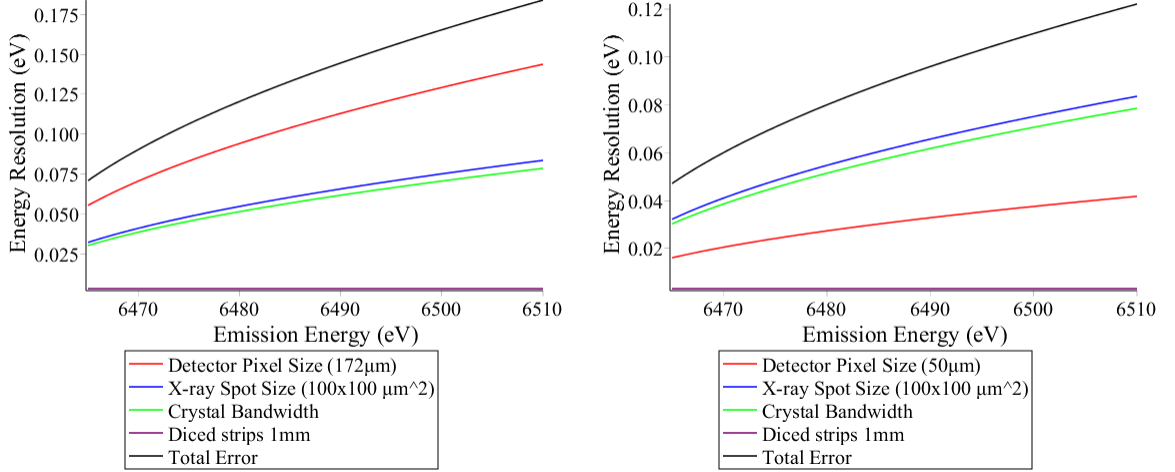
Figure 4.3. The individual energy resolution contributions and the total energy resolution is shown using the Pilatus 100k (left) and the Mythen 1K (right) detectors.

Theoretical energy resolution at different Bragg angles is given for the spectrometer as shown in Figure 4.3 as a function of the emission energy.

4.2.1 Darwin Error

The rocking curve, or Darwin width, is the range of angles reflected off a crystal surface when exposed to a monochromatic beam of fixed energy. The range of angles for a typical pure crystal is from 10-100 μradians. Equivalently, this can be understood as a range of photon energies that can reflect at each Bragg angle in a crystal, making the reflection at each angle not perfectly monochromatic. The Darwin width contribution is then solely represented as the FWHM of the theoretical rocking curve,

$$\Delta\Theta_{Darwin} = FWHM(Rocking\,Curve). \tag{4.3}$$

The FWHM of the rocking curve is an intrinsic property of the crystal type and purity level.
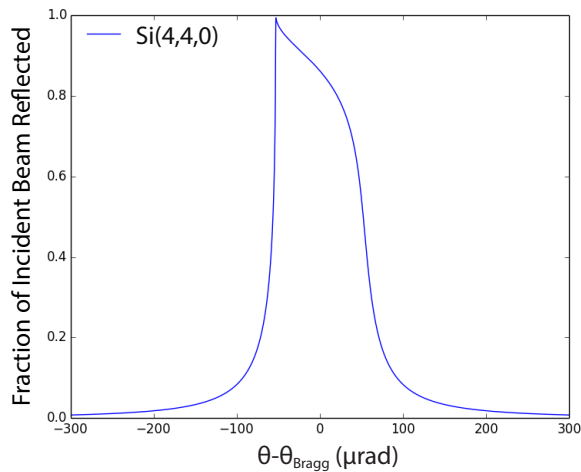
Figure 4.4. The fraction of incident beam reflected as a function of the difference between the Bragg angle and the actual incident angle for an x-ray photon energy of 6490eV. These values are calculated using the software package XOP [89] for a Si(440) reflection.

4.2.2 X-ray Spot Size

The source, or the x-ray fluorescing region of the sample, is not a perfect point source so x-rays with a range of diffracted angles from the sample will converge on the detection surface. This range of Bragg angles subtended by the sample from any point on the detector is treated as the error term for this contribution.

This leads to the equation for the angle error $\Delta\Theta_{Spot}$,

$$\Delta\Theta_{Spot} = \frac{(Spot\,Size)\sin(\theta_{Bragg})}{2R} \tag{4.4}$$

where R is the radius of the von Hamos crystal curvature. This simplifies when the Bragg angle is close to back scatter to be

$$\Delta\Theta_{Spot} \approx \frac{Spot\,Size}{2R}. \tag{4.5}$$

Here the spot size refers to the diameter of x-ray beam spot size. Note that this doesn't include factors such as sample thickness which may be important depending on the orientation of the spectrometer. For the spectrometer mentioned herein, the spot size is a good approximation for the range of angles in the dispersion direction (i.e. along the axis of curvature of the x-ray crystal) that will converge on a single spot on the detection surface, or x-ray spot size contribution to the error.

4.2.3 Detector Pixel Size

The detector pixel size has a similar contribution, only the reverse geometry is considered. The range of Bragg angles used here is that subtended by a single pixel from a single point on the sample. This error simply follows the previous and is approximated for large Bragg angles as

$$\Delta\Theta_{Det} \approx \frac{Pixel\,Size}{2R} \tag{4.6}$$

where the pixel size is the width of the pixel in the direction of energy dispersion. The only difference in this case is that the detector is typically perpendicular to the incoming x-rays which makes the approximation more exact.

4.2.4 Diced Von Hamos Errors

The final error discussed is only associated with diced von Hamos used in a focused geometry. The first part can be easily understood as the range of angles reflecting off the diced crystals of width d_w. The x-rays diffracting off the center of the crystal will have different Bragg angles than those hitting the side. The range of angles across the width can be found geometrically to be the difference between the central reflection and the reflection off the edge, which can be written as

$$\Delta\Theta_{Diced} = \theta_{Bragg} - \arctan\left(\frac{R}{\left(\left(\frac{R}{\tan(\theta_{Bragg})}\right)^2 + \left(\frac{d_w}{2}\right)^2\right)^{\frac{1}{2}}}\right) \tag{4.7}$$

This error becomes negligible as the dicing width gets small and R gets larger.

This error becomes more complicated when considering multiple diced strips whose reflective surfaces are not parallel to the detector surface. This means x-rays will travel a further/shorter distance, and at different Bragg angles, to the same point on the detection surface depending on which side of the analyzer the x-rays are reflected. While this error term becomes quite complicated symbolically, calculations for the FWHM for this spectrometer with an incident energy of 6490 eV shows a negligible energy error of <0.002 eV for the one crystal spectrometer described in this chapter.

4.3   Analyzer Fabrication

The fabrication process for the finely diced von Hamos analyzer is here described and outlined in Figure 4.5. The fabricated x-ray analyzer used a 200 mm diameter polished Si(110) wafer that was 1.5 μm thick. The wafer was diced to the 180 mm x 45 mm shape then glued to a 1/16" polycarbonate sheet that is slightly larger in area than that of the wafer. The glue used was a non-expanding epoxy (Epotek 301 parts A and B) that requires 3 days minimum drying time at room temperature. Care was taken to eliminate bubbles or particles from affecting the bonding. After the glue was in place, a parallel plate press was used to maintain the appropriate pressure to form a very thin uniform layer of glue between the two surfaces.

After the glue was dried, the plastic substrate was mounted to a thin tape for dicing. This was done with a minimal amounts of heat to prevent surpassing the glass transition temperature of the epoxy, 65°C. The wafer was diced parallel to the dispersion direction (in this case the 45 mm length direction) using a dicing saw, cutting completely through the thickness of the wafer but leaving the plastic material underneath uncut or minimally scarred. Each of the diced strips were 1 mm in width with a 300 μm kerf, or cut width, between strips. Note that the resulting spectral line width will minimally be twice the width of the diced strips and that the kerf width doesn't contribute to the overall collection efficiency. When determining the wafer thickness, a balance must be met between the wafers being thick enough to not break
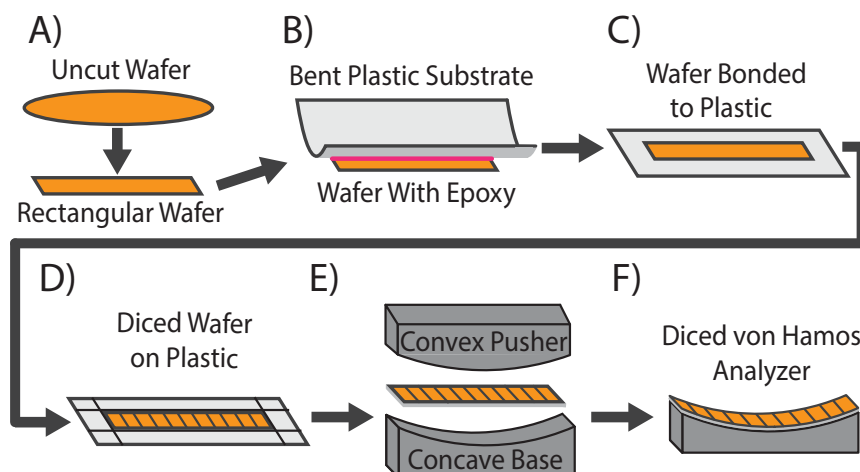
Figure 4.5. The general process of making a diced von Hamos analyzer is outlined starting with a A) wafer diced to shape, B) glueing the plastic substrate to plastic by bending and attaching to a wafer to reduce air bubble formation, C) binding to plastic, D) diced into strips and E) and F) fixed to an Al base. B) highlights the process of creating a layer of epoxy between the plastic and wafer without bubbles (glue is shown as red) by bending the plastic and pressing onto the wafer.

or flex in the pressing process, but not so thick that a wider dicing blade is required, increasing the kerf. Once the final dicing is done, the plastic bound wafer strips will have the flexibility to form a cylindrical base.

Wire electrical discharge machining (EDM) aluminum was used to obtain a top pusher and base at the correct radii. While attempts to use plastic pushers/bases were used, they were found to have too much flex during the pressing procedure.

The wafer was then sandwiched between the wire EDM pusher, with the desired radius, and the base which it would be glued to, with an adjusted radius for the wafer and plastic thickness. While in the press, the glue between the base and the plastic allowed the diced wafer to take the final form. Various protocols were tested to isolate the glue from the top pusher to prevent the silicon from bonding to the pusher. The final procedure included a uniform 4μm Kapton film over the pusher with a Leadership Performance Sustainability (LPS) brand lubricant spray applied

to the mating surface of the top pusher. The Kapton with lubricant could then be removed after the glue between the plastic and aluminum based is dried.

We also note that this process does not require deep reactive-ion etched silicon on insulator wafers [90] or a scar and break process for diced analyzers [85]. While the deep reactive ion etching can create smaller cuts, it is also requires more technical equipment, is limited to materials that can be used in this process and result in very fragile wafers. The breaking process leaves some uncertainty in reproducibility and unlikely to achieve finely diced strips obtained here or with deep reactive-ion etching.

4.4   Diced von Hamos Spectrometer Design

Previous PSII time resolved x-ray emission Spectroscopy (TR-XES) measurements by our group incorporated the miniXS [91–93] spectrometer which has ten crystals to simulate the von Hamos geometry similar to that of a diced crystal. This series of flat crystals are only partially aligned (to within 0.5 degrees) and are only positioned using a 3-D printed surface. The energy error from misaligned spectral overlap between crystals is overcome by recording each reflection at a distance from the sample where each reflection is both out of focus and isolated.

The miniXS has proven to be quite versatile, partly due to its straightforward alignment and easy integration into most beamlines. While in many ways this detector is advantageous over other dispersive spectrometers, TR-XES measurements of dilute samples, such as PSII, result in low signal. This makes the shifts in PSII spectra, ≤ 0.06 eV, difficult to identify even with several beamtimes of data collection.

In order to detect the weak signals, a new spectrometer was specifically designed, and is described herein, for the TR-XES of dilute samples.

The new spectrometer incorporates a single large analyzer as shown in Figures 4.6 and 4.2. This particular design uses a fixed diced von Hamos analyzer that diffracts, according to Bragg's law, both the Mn $K\beta_{1,3}$ and $K\beta$' emission onto a dispersive focal line of ~ 2 mm width. The whole spectrum is read out by an a stripline or
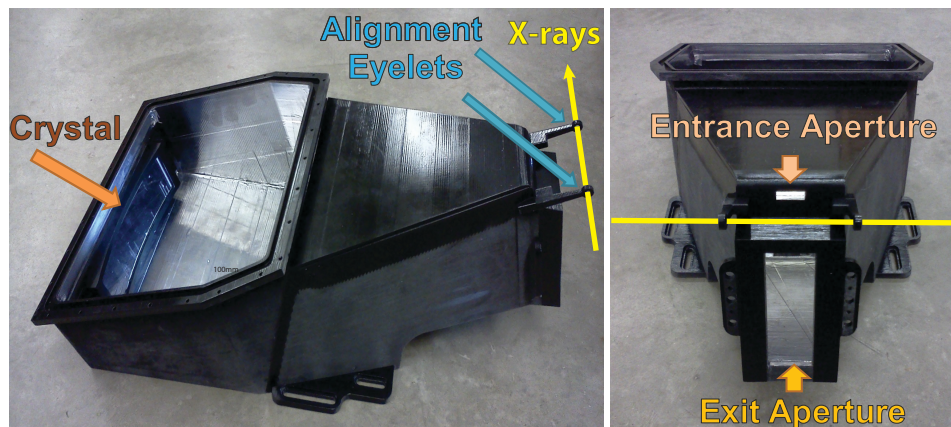
Figure 4.6. A new 3-D printed spectrometer is shown with the crystal mounted to the back face in the horizontal orientation, as shown, with two removable eyelets to align the spectrometer to the x-ray beam (left). A removable plate seals to the back half of the spectrometer to maintain a He environment and allow access inside (plate not shown). The entrance and exit apertures are shown from the front without the internal shielding in place.

2-D position sensitive x-ray detector. The background x-ray counts are reduced in the current spectrometer geometry by using anisotropic nature of the elastic scatter. The minimum scatter occurs in the plane of x-ray polarization, which is the plane where the electric field of the x-rays are oscillating. In this plane, and at an angle of 90 degrees from the incident x-ray beam, the theoretical elastic scatter off a point source goes to zero. This spectrometer design is built around that angle to reduce the number of scattered photons accepted into the entrance aperture. The tight focus eliminates background signal by using internal apertures and an area detector to reject photons outside of the focal line. A single large x-ray optic ensures that tight internal apertures can be used while maintaining the large solid angle 23.6 mSr.

Because of the large collection angle and focusing geometry, the spectrometer increases the recorded signal and increases the speed of elastic scatter calibration which was previously prohibitive. Like the miniXS, this system is easily integrated into most beamlines by a simple two-step process of 1) aligning two eyelets (see Figure

4.6) to the x-ray beam and 2) scanning the sample upstream and downstream to find the center alignment for the entrance aperture. The second step can be replaced by a short focal depth camera and a 3-D printed mid-plane alignment tool which uses the same dowel pin holes as the alignment eyelets.

The spectrometer was 3-D printed using VeroBlackPlus RGD875 material, which does not to have any detectable x-ray fluorescence at 10keV. The space inside of the spectrometer is isolated from the environment using a thin Kapton window for the entrance and exit apertures and a constant He flow.

Total production costs for the analyzer was <$500 U.S., most of which is in the cost of the aluminum base, whereas the solid angle equivalent would require ∼4 spherical analyzers, 100 mm diameter with 1 m radius curvature, each typically costing approximately $10,000 commercially. This setup also does not require the additional cost for motors since the single optic is left stationary. While the helium chamber was printed using prototype (i.e. 3-D printing) technology for more flexibility and adaptability, cheaper methods could also be employed in future designs. Both the miniXS and this spectrometer feature a cost effective design, with this spectrometer having the additional compatibility with stripline detectors, such as the Mythen 1k. Stripline detectors are usually much cheaper ($23,000 U.S. Dollars for Mythen 1k) than the 2-D area sensitive pixel detectors ($65,000 for the Pilatus 100k). This further lowers the cost of the complete detection system.

4.5   Methods

Measurements were taken at the Advance Photon Source beamline 20-ID-C. Here the x-rays were first conditioned after the undulator by high heat load slits which reduce x-ray flux and protect downstream elements from thermal damage. A long toroidal mirror was then used at a glancing angle to focus the beam which then goes through two Si(111) crystals to make a monochromatic beam with an energy resolution of $\frac{\Delta E}{E}$=1.33x10^{-4}. The beam position from the monochromator is monitored

by a diamond beam position monitor from Sydor Technologies. This gives real-time feedback to the monochromator so as to maintain the incident angle of the beam. The stabilized beam was then shaped using slits then focused using a set of Kirkpatrick-Baez (KB) mirrors to a size of $\sim$100x100μm^2. The beam spot size was verified using a YAG crystal with a Prosilica camera. The beam intensity was $\sim$5$\times$10^{12} photons/sec at 7500 eV.

Calibration of the monochromator was done using a potassium permanganate (KMnO$_4$) which has a sharp absorption pre-edge feature at 6543.3 eV. Elastic scatter from the sample was used to calibrate the emission spectrometer in 2-3 eV steps according to a previously established procedure [92]. The incident beam was tuned to 7500 eV for all non-resonant measurements and a Pilatus 100k was used to collect the emission spectra.

All oxides used were purchased from Sigma Aldrich including KMnO$_4$, MnO, MnO$_2$ and Mn$_2$O$_3$. KMnO$_4$ was used as a powder sealed between two layers of Kapton tape while MnO, MnO$_2$ and Mn$_2$O$_3$ were prepared as pellets with a concentration of boron nitride as a binder of 0%, 10% and 12% by weight. These were sealed between a Kapton tape on the back side and a 4 μm polypropylene window on the front. A thin plastic sheet, $\sim$0.5 mm in thickness, was used for energy resolution measurement using elastic x-ray scatter . All samples were positioned at 45 degrees relative to the incident beam and the spectrometer entrance aperture.

4.6   Results

The energy resolution of the monochromator, $\frac{\Delta E}{E}$=1.33x10^{-4}, was then used to find the resolution of the detection system using the equation

$$E_{res} = \sqrt{(FWHM)^2 - (E_{mono})^2}.$$
(4.8)

The energy resolution at 6490 eV was found to be 0.13 eV which is consistent with the theoretical error of 0.14 eV obtained using the energy resolution equations described in this chapter.

Spectrometer parameters of other Mn spectrometers are herein compared to previous designs in Table 4.1 including the miniXS [91] and a 16 crystal von Hamos analyzer built at the Linac Coherent Light source [88].

Table 4.1.
The spectrometer design is reported with an experimental energy resolution and calculated solid angle. Alignment details, focus geometry are discussed elsewhere (Section 4.7)

	Current Spectrometer	miniXS [91]	LCLS - 16 Analyzers [88]
Analyzer Material	Si(4,4,0)	GaP(4,4,0)	Si(4,4,0)
Energy Resolution @ 6490 eV	0.13 eV	0.3 eV	0.55 eV
Solid Angle	23.6 msr	12 msr	165.6 msr
Focused Geometry	Yes	No	Yes
Quick Alignment	Yes	Yes	No
Approximate Cost (U.S.)	<$1,500	~$1,000	~$300,000+

A series of Mn compounds were measured using the new spectrometer. A few Mn standards are shown in Figure 4.7 which can be compared to those recorded previously with the miniXS at the Advanced Photon Source beamline 14-ID-B.

4.7   Discussion

The spectrometer described in this chapter has several advantages when compared to other von Hamos configurations. Some of the main features involved include background rejection, energy resolution, solid angle, cost, alignment and focus geometry.
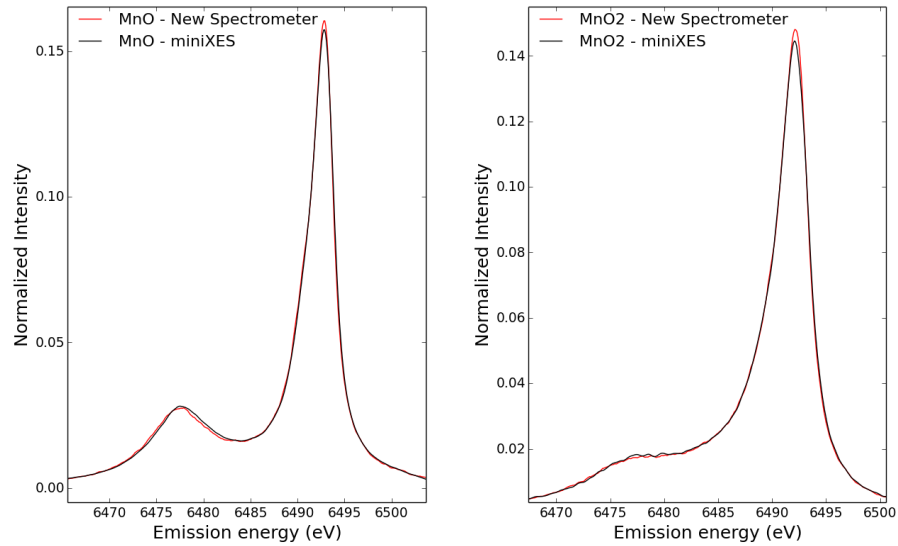
Figure 4.7. Comparison of the new detection system to that of the miniXS using Mn Oxides. Both graphs are normalized by area between 6470-6500 eV making spectra with a higher energy resolution and lower background have a higher peak value.

The energy resolution of this particular spectrometer was found to be $\frac{\Delta E}{E} = 2 \times 10^{-5}$ at 6490 eV and can be further improved by using a Mythen detector with 50 μm pixel strips (see Figure 4.3) or by using a smaller spot size until it is limited by the bandwidth of the crystal.

The solid angle of the spectrometer is largely increased due to the fabrication process which enables large wafers to be used. As can be seen in Table 4.1 the solid angle is $\sim$2x that of the miniXS design. The solid was calculated to be twice that of the miniXS at 23.6 msr which is extremely high for a single crystal spectrometer. While the solid angle is smaller than that of large multi-crystal spectrometers [86,88], multi-crystal von Hamos systems generally suffer from reduced energy resolution, costs, difficult alignment, also provide little space for any apertures to reduce background. As these multi-crystal setups can be quite large, occupying a large space in the beamline hutch or vacuum chamber, they are not very easy to deploy into

different time resolved beamlines based or on multipurpose beamlines unless they are strongly considered in the permanent setup. This new spectrometer, however, shows the same simplicity of easy beamline integration as the miniXS designs [91].

One of the main features of the miniXS spectrometers was the cost, since there are only diced wafers placed on a 3-D printed scaffold, the majority of the price is the prototyping material. Similarly, this spectrometer has few costs due to the fixed geometry and the fact that it only uses a single large analyzer. This design is also 3-D printed and the fabrication protocol is simple and effective. This simple design also allowed for a larger unobstructed space around the sample, allowing a liquid jet to be used, whereas the previous miniXS did not accommodate such improvements.

While Mn oxides showed the proof of concept of the spectrometer, the ability to measure small shifts in FM of dilute samples was also tested at room temperature. Two samples, $[\text{Mn}^{\text{IV}}(\text{OH})_2(\text{Me}_2\text{EBC})]^{2+}$ and $[\text{Mn}^{\text{IV}}(\text{O})(\text{OH})(\text{Me}_2\text{EBC})]^+$ [94], were measured to give insight into the changes that occur to a central metal atom when the ligand character has small changes (i.e. OH^- to O). These subtle changes were used to understand shifts in more complex system using non-resonant XES as outlined in Chapter 5.

4.8 Conclusions

The spectrometer outlined in this chapter allows for the recording of dilute samples by higher solid angle capture of fluorescence, high energy resolution and high background rejection. This system is also an effective tool for integration into most beamlines using a simple method of alignment. As a cost effective solution this spectrometer can be used at synchrotron, as part of the user equipment or for multipurpose beamlines, or with lab-based sources. Costs are further reduced for the complete detection system as this spectrometer only requires a 1-D position sensitive x-ray detector, or stripline detector, which are a fraction of the cost of 2d position sensitive x-ray detectors. As a prototype, the solid angle is a factor of 2 higher than

the miniXS spectrometer designed to record Mn Kβ emission. This system also allows for more space around the sample for easier integration of new sample delivery methods.

5. XES of Biomimetic Compounds and Validation of Spectrometer Performance

The spectrometer discussed in the previous chapter was designed to improve efficiency for measure dilute metalloproteins (such as PSII) by increasing the solid angle that captures emission while maintaining a high energy resolution. However, due to the spectroscopic signal of PSII being extremely dilute, we chose to first test the spectrometer's capability by measuring the two biomimetic compounds, $[Mn^{IV}(OH)_2(Me_2EBC)]^{2+}$ and $[Mn^{IV}(O)(OH)(Me_2EBC)]^+$. Through the measurements of these two biologically relevant compounds, we verified the performance of the spectrometer when recording samples of limited volume which result in small spectroscopic shifts, while identifying changes between $Mn^{IV}OH$ vs $Mn^{IV}{=}O$.

5.1 Introduction

X-ray emission spectroscopy is often used as a probe of oxidation state changes for a specific element in a sample. This can be important for metalloproteins in particular as the metal content is low but can still be probed directly. Time resolved measurements following oxidation state changes enable the capturing of transient states or to understand the mechanisms at play during their function. For example, the OEC is the catalytic center in PSII responsible for splitting water in plants. As has been mentioned in previous chapters, gaining a clearer understanding of the changes in the electronic structure of this Mn_4Ca cluster, is essential to the future design of efficient artificial photosynthetic systems.

As the OEC in PSII has four separate Mn atoms, changes in oxidation of any one atom will result in a comparatively small shift in the $K\beta_{1,3}$ mainline. To test the feasibility of detecting such a small shift reliably, we use two standard compounds

$[Mn^{IV}(OH)_2(Me_2EBC)]^{2+}$ and $[Mn^{IV}(O)(OH)(Me_2EBC)]^+$. As these compounds had a significantly higher Mn content than metalloproteins this enabled a faster feedback for the system.

Additionally, through measurements of these two samples we can estimate the changes a single deprotonation event can have in the emission signal for PSII as the two compound are identical except that the first compound contains a $Mn^{IV}OH$ fragment while the second contains a $Mn^{IV}=O$ fragment. Of particular note is the report of the possibility of the $Mn^{IV}=O$ fragment being involved in the role of oxygen formation during water splitting [12]. By comparing the spectroscopic signatures of previously obtained PSII and the biomimetic compounds, we see that a similar nominal spin is obtained in both cases.

5.2 Methods

5.2.1 Sample Preparation

Using the spectrometer described in Chapter 4, x-ray emission spectra were collected at room temperature from two Mn complexes namely $[Mn^{IV}(OH)2(Me_2EBC)]^{2+}$ (**1**) and $[Mn^{IV}(O)(OH)(Me_2EBC)]^+$ (**2**) [95, 96] (Me_2EBC = 4,11-dimethyl-1,4,8,11-tetraazabicyclo[6.6.2]hexadecane), see Figure 5.1A in the results section. Each sample was delivered in 8 mM solution via a liquid jet of diameter $\sim 500\mu$m. The method published by Yin et al. [96] for creating Compound (**1**) was followed, then the resulting precipitate was dissolved in water at pH4.4 and adjusted with NaOH to generate (**2**) at pH 8.4.

All of the oxides used in this experiment were acquired from Sigma Aldrich including MnO (Cat. No. 377201), Mn_2O_3 (Cat. No. 463701), MnO_2 (Cat. No. 243442) and $KMnO_4$ (Cat. No. 22346). The powder $KMnO_4$ was sealed between two layers of Kapton tape. The other oxides, MnO, MnO_2 and Mn_2O_3, were prepared as 1cm diameter pellets with boron nitride composing 0%, 10% and 12% by weight respectively. These pellets were sealed between a 4 μm polypropylene window and Kapton

tape. Mn oxide pellets were oriented at an angle of 45 degrees relative to the incident beam and the entrance aperture of the spectrometer.

5.2.2   Beamline Parameters

XES measurements were taken at the Advanced Photon Source beamline 20-ID-C. Focusing of the beam was done using a long toroidal mirror. A monochromatic beam with an energy resolution of $\Delta E/E = 1.33 \ 10^{-4}$ was created using two cryogenically cooled Si(111) crystals. A potassium permanganate ($KMnO_4$) was used to calibrate the monochromator by using the pre-edge feature at 6543.3 eV.

5.2.3   Sample Delivery and Data Collection

The sample was delivered as a liquid jet which cycled 15 mL of the sample volume every 15 seconds. This was done with both samples (**1**) and (**2**) at room temperature. The XES measurements were collected within the first 10 seconds of continuous x-ray exposure as a series of 100 exposures of 100 ms. Subsequent cycles of the jet were used for an *in situ* spectrometer calibration using 2 eV steps of the monochromator beam. The x-ray beam spot was slit down to $\sim$100$\times$100 μm^2 was and an incident flux of $\sim$5$\times$10^{12} photons/sec was used for the oxides and an Al film was used to attenuate the beam to $\sim$5$\times$10^{11} photons/sec for samples (**1**) and (**2**). The incident photon energy for all XES measurements was 7.5 keV. To limit x-ray induced changes to the electronic structure, samples received a dose of only 140 Gy (a factor of 100 less than that required to damage the sensitive PSII) [97].

5.3   Results

5.3.1   X-ray Emission Spectra

The XES spectra of the two Mn compounds exhibit a slight shift of 0.07eV, Figure 5.1. This provides critical information of how other factors besides the formal
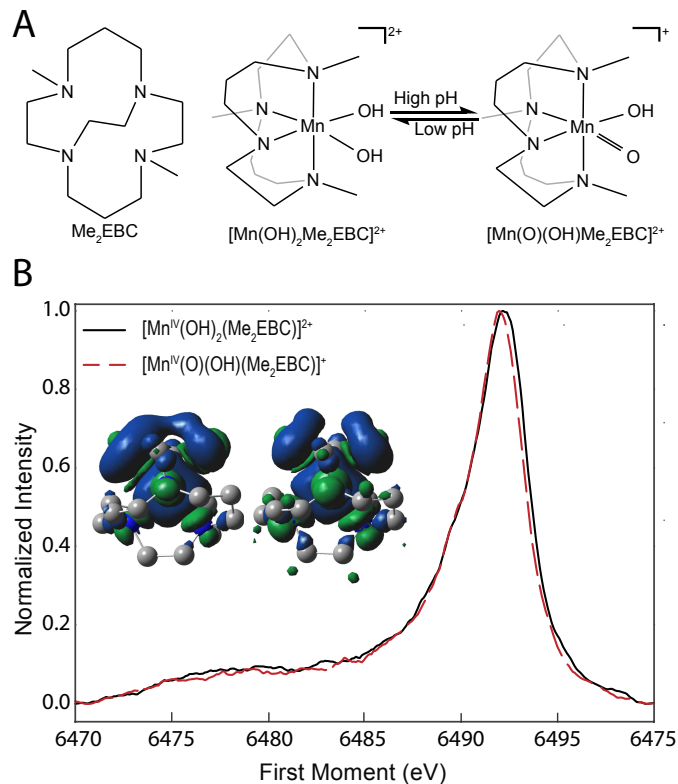
Figure 5.1. (A) Diagrams of the Me$_2$EBC ligands, [Mn^{IV}(OH)2(Me$_2$EBC)]$^{2+}$ (**1**) and [Mn^{IV}(O)(OH)(Me$_2$EBC)]$^{+}$ (**2**). (B) Room-temperature Mn Kβ XES spectra of (**1**) at pH = 4.4 and (**2**) at pH = 8.4 in aqueous solvent. Inset are the spin densities of those compounds (from DFT), which show a shift of electron density to the oxygens upon deprotonation. This difference in electron density gives rise to the observed spectral shift.

oxidation state affect the MnKβ spectral positions. This is evidence that upon deprotonation, the electron density shifts which changes the observed spectra.

5.3.2 Nominal Spin Assignment

XES is commonly analyzed by changes to a first moment. The first moment stems from shifts in the Mn K$\beta_{1,3}$ line and are calculated as FM= $\Sigma_i I_i E_i / I_i$, where E$_i$ is the emission energy and I_i is the intensity of the spectrum at that energy. The K$\beta_{1,3}$
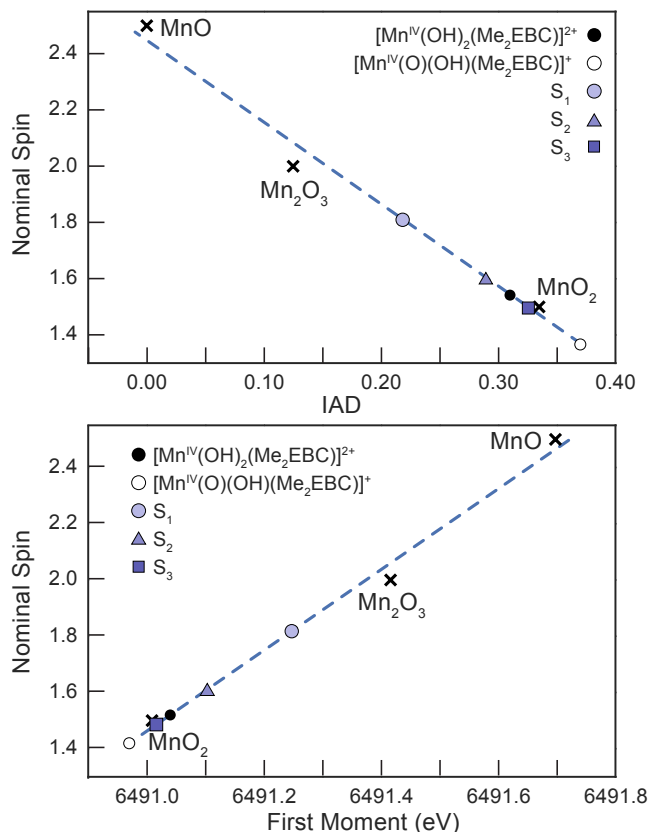
Figure 5.2. To understand the relationship between the nominal spin and the first moment energy (or IAD), a linear fit is created from the known values of Mn oxides in three different oxidation states. With each fit, the nominal spin of selected S states and the complexes (**1**) and (**2**) were found.

spectral feature is in the 6485-6495 eV range. All spectra were smoothed using 9-point boxcar averaging which corresponds to a 0.9 eV range. A linear background was then subtracted across the energy range of 6470-6500 eV by using a linear fit to the first and last five data points in the range (0.5eV). Similar to the first moment analysis, another measure of the data is the integrated absolute difference (IAD). For the IAD values reported here, MnO was used as the reference see Section 3.2.5 for further discussion of IAD. The values for both the first moment and the IAD data are listed in Table 5.1.

The IAD and the first moment analysis have been shown to be a good estimator of the nominal spin of a sample [57]. By carrying out a linear least-squares fit to Mn oxide data, a linear relationship can be formed between the first moment or IAD value and the known nominal spin, Figure 5.2. The linear fits obtained had an R^2 = 0.99 for the first moment and R^2 = 0.98 for. This linear dependence was used to predict the nominal spins for (**1**) and (**2**), Table 5.1. The expected spin value for each of these Mn^{IV} ions is S=3/2. The nominal spin value for(**1**) is in good agreement with the expected value of 1.5 for a Mn^{IV} ion (1.52 or 1.53 for first moment and IAD respectively); however the nominal spin value of (**2**) starts to deviate significantly from this value (1.41 or 1.36 for first moment and IAD respectively).

5.3.3 Comparing Results with DFT

To better understand the the different spin values for the two compounds despite their identical oxidation state, DFT calculations following the methodology outline previously [95], were calculated (see atomic positions in Appendix B). Formation of the Mn^{IV}=O fragment was shown to result in a redistribution of charge and spin in the complex.

Recognizing that different ligands affect the nominal spin (and thereby the energy spectrum) of a compound isn't new. Previously, two Mn compounds with Mn^{III}/Mn^{IV} oxidation states showed a first moment difference of ∼0.14 eV based on their ligand environment [98]. DFT calculations were used to attribute the difference to a nominal average spin difference of 0.07 eV between the two compounds. Here, DFT analysis closely matches our experimental results by confirming a significant difference in the calculated nominal average spin for $[Mn^{IV}(OH)_2(Me_2EBC)]^{2+}$ (ρ=2.98; 1.49) and $[Mn^{IV}(O)(OH)(Me_2EBC)]^+$ (ρ=2.54; 1.27) (See Figure 5.2, Table 5.1).

Here we note that the Mn Kβ XES results represent different yet complementary results to those obtained earlier during XANES analysis [95]. XANES analysis of the pre-edge region showed considerable differences between the two compounds. A

sharp pre-edge feature was shown to exist for the $Mn^{IV}=O$ fragment due to the strong mixing of the oxygen p orbitals with those of the Mn 3d orbitals as is typical found for $Mn^{IV}=O$ fragments [99, 100]. Contrary to the sharp changes in the pre-edge feature, the rising edge for Mn K-edge XANES of (**1**) and (**2**) are nearly indistinguishable, based on the lack of change in oxidation state. Mn $K\beta$ XES, however, does change according to the nominal spin of the Mn center, Figure 5.2, Table 5.1. The change in first moment of 0.07 eV then corresponds to the formation of a $Mn^{IV}=O$ with reduced nominal spin. As a result of this $Mn^{IV}=O$ fragment, the main line of the Mn $K\beta$ emission spectrum is shifted to a detectably lower energy.

Table 5.1.
Experimental values for the first moment and IAD calculations based on the Mn $K\beta_{1,3}$ XES and DFT results. Errors in parenthesis are standard errors of the mean with a sample population of 100 (i.e. the first moment was calculated for each exposure). Errors in spin are calculated using the linear fit and the error in measurement.

	First Moment		IAD		DFT
	Experiment	Spin*	Experiment	Spin*	Spin
1	6491.04 (0.02)	1.52 (0.03)	0.31 (0.003)	1.53 (0.009)	1.49
2	6490.97 (0.007)	1.41 (0.01)	0.37 (0.001)	1.36 (0.003)	1.27
Δ	0.07 (0.02)	0.11 (0.03)	0.06 (0.003)	0.17 (0.009)	0.22

*Spins are predicted from fits shown in figure 5.2.

5.4 Interpretation of spectroscopic signal

These results are interesting in the context of water oxidation mechanisms. In Ru-based water oxidation catalysts, a highly oxidized Ru=O species plays an important role in O-O bond formation [101–105]. Many have anticipated a similar mechanism in photosynthesis, yet a $Mn^{IV}=O$ intermediate has not yet been detected for the OEC.

The S3 state is the most oxidized state of the Mn4Ca cluster, and EXAFS) [29,30] and femtosecond crystallography, [10,11,14] have indicated that the S3 state is associated with many structural changes, but less is understood about its electronic structure.

Based on a small first moment shift in the recorded Mn Kβ XES spectra, Messinger et al. concluded that the S2-S3 transition must involve a ligand-centered oxidation rather than a Mn-centered oxidation [18]. Similarly, recent room temperature XES measurements of the S3 state have been interpreted as oxidation of the five coordinate Mn^{III} to a six-coordinate Mn^{IV} during the S2-S3 transition [28] but there is still much debate about this state, see Section 2.3.3.

For comparison purposes, previous results of the first three S states of room temperature PSII [106] are added in Figure 5.2. Results for the S3 state lie in between the values for compounds (**1**) and (**2**). This indicates that an all Mn^{IV} redox configuration is plausible for the S3 state, Figure 5.2. Additionally, the formation of a Mn^{IV}=O is still plausible given a similar shift in XES between the S2 to S3 state, shown in Figure 5.2, in the same direction. While combining oxidation to the Mn^{IV} state and Mn=O formation would create a larger shift than the formation of Mn^{IV} by itself, the possibility of the simultaneous changes are not excluded given the reduced magnitude of shift for a system in which one in four Mn atoms being affected by the change and simultaneous changes in structure (possibly coordination) which will also result in a change in localized spin density.

5.5   Conclusions

The impact of this experiment is two-fold:

- To improve our interpretation of spectroscopic signals when measuring Mn-based metalloproteins such as PSII.

- To show the efficacy of the spectrometer described in the previous chapter.

By measuring the two similar biomimetic complexes [Mn^{IV}(OH)$_2$(Me$_2$EBC)]$^{2+}$ and [Mn^{IV}(O)(OH)(Me$_2$EBC)]$^+$, we were able to verify the ability of the new spectrome-

ter in measuring small spectroscopic shift. The small shift of 0.07 eV between the two compounds confirms that ligand environment affect the local spin density which in turn affects the spectroscopic signal. While it remains unconfirmed, our data suggest an all Mn^{IV} OEC in S3 is plausible and a model containing a $Mn^{IV}=O$ redox configuration in the S3 state of photosystem II is also possible, though a simultaneous reduction in localized spin density through structural rearrangement would have to occur.

The XES spectra of the two compounds show a small shift of 0.07 eV, Figure 5.1. As described in the previous chapter, the benefits of this spectrometer include more background rejection and better energy resolution for the recorded energy range of Mn x-ray emission. More importantly, however, is the 2 fold increase in solid angle capture that a single analyzer spectrometer was able to achieve. This success of this prototype led to the development of multiple analyzer spectrometers as is discussed in the next chapter. Additionally, the sample delivery method would not have been achievable using the previous spectrometer design. This is due to the lack of space between the x-ray/sample interaction point and the reflected x-rays from the crystal surfaces. This increase in sample space opens new possibilities for an a simple automated design for sample delivery of metalloproteins.

6. Time Resolved X-ray Spectroscopy Instrumentation

6.1 Introduction

As explained earlier, X-ray emission spectroscopy (XES) is a valuable technique that can give bulk information about the electronic structure and, depending on the emission lines recorded, can be used to identify the oxidation state, ligand type and covalency of specific elements [57, 107, 108]. The development of X-ray free electron lasers (XFELs) [109–114], more advanced synchrotron beamlines [115–117] and high power benchtop laboratory based sources [118–120], has greatly increased the availability and options of using XES to probe electronic structure. As the number of sources has increased, so has the demand for X-ray emission detection and sample delivery systems that are cost effective and customizable.

Though useful, XES is not without its challenges. Signals are inherently weak due to fluorescence being a secondary process, analyzer dispersion limiting throughput and small solid angle capture. This is problematic in and of itself but this issue is only amplified in cases where samples are dilute or x-ray sensitive (typically both in the case of metalloproteins). In an effort to improve the signal, large arrays of crystal analyzers have been used to maximize solid angle capture [121]. While this method is useful for facilities with dedicated setups and larger budgets, this is unrealistic for smaller laboratories with limited funding and/or physical space. In some cases energy resolution can be sacrificed by using highly annealed pyrolytic graphite analyzers with increased reflectivity but this comes at the cost of a dramatic loss of energy resolution [122, 123]. These systems then become a delicate balance between trying to have the capacity to measure a spectrum and the resolution to interpret the spectrum.

Here a spectrometer designed to maintain a high energy resolution and still collect high amounts of signal using new cost effective analyzer fabrication process described

in Chapter 4 is outlined. We created a new cost effective analyzer fabrication process that increased the solid angle collection. After our success with a single analyzer spectrometer, we then improved our original design to increase the detection area even more by using multiple analyzers in the spectrometer without the need for motor alignment of each crystal.

Another common problem of TRXES is the ability to reliably replace sample. The most common method of replenishing photoactive samples measured at XFELs is the use of a liquid jet. As the sample jets towards the interaction region, the sample is excited with a laser pulse. The x-ray probe delay is adjusted by adjusting the timing sequence and the distance above the x-ray interaction region the laser excites the sample. This method of delivering sample can be extremely wasteful with large portions of the sample passing the X-ray interaction region without measurement. A newer system previously developed overcomes many of these deficiencies by using an acoustic droplet ejection system to deposit drops of sample on a thin film [124]. The film is then moved to a predetermined location for both the pump and probe excitations. We improved upon that design and created a system with a much lower price point and doesn't require acoustic ejection. Our system is fairly compact and can be easily transported and integrated into hard X-ray beamlines or with sources in the lab. Applications of this system are particularly useful for liquid samples that are X-ray sensitive, or limited in volume

6.2   Multi-Analyzer X-ray Emission Spectrometer

While the previous prototype worked for most samples, metalloproteins are known to be dilute and give exceptionally weak signal, so a spectrometer with three analyzers was designed. The new spectrometer was built in a similar manner to the previous spectrometer [125], see Chapter Spectrometer, with the distinction that the 3D printed case has built in locations for three analyzers, Figure 6.1. These crystals are oriented such that the reflections of each crystal are parallel, but do not overlap,

on the detection surface. The crystals are fixed inside the spectrometer so that no motorized alignment is required. This limits the spectrometer to a single emission range, Mn Kβ in this case, however it also improves the ease of integrating into any beamline since the system is independent of internal motors and is already fixed at the optimized geometry. The entrance and exit apertures are covered with a thin Kapton film to reduce scattering and absorption but maintain a He environment inside. A large access port in the back is sealed with an O-ring and a thick plastic cover. The holes around the gasket were filled with metal inserts to obtain 2-56 threaded holes. In order to reduce the x-ray scattering by gas inside the spectrometer, a low constant flow of Helium is supplied. To record the data of a three crystal spectrometer, a 2D position discriminating X-ray detector is required. For our Mn Kβ spectrometer, we used a Pilatus 100k (Dectris).
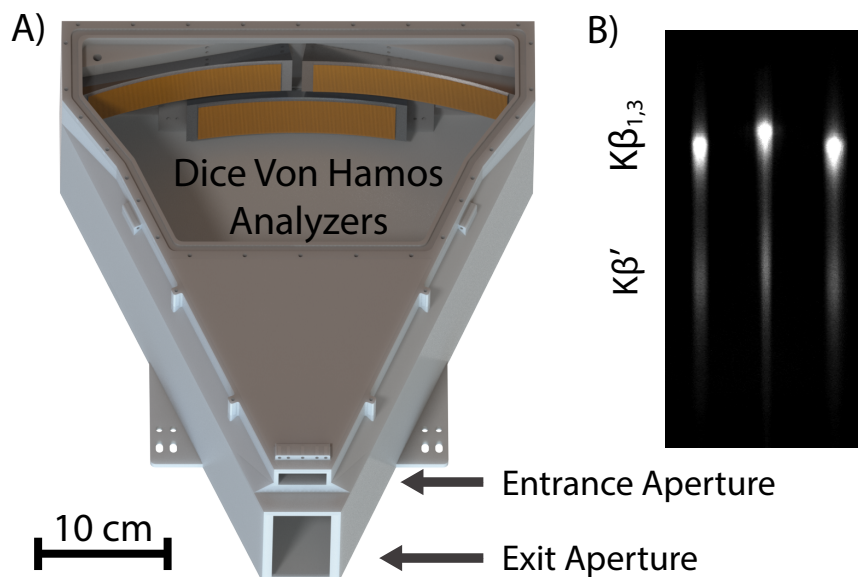
Figure 6.1. A) A picture of our 3D printed spectrometer with the three von Hamos Analyzers inside. Analyzers are colored orange for easy discernment. B) Emission spectra from MnO taken with Pilatus 100k. The two outside spectra were dispersed by analyzers with 100 μm strips and the center spectra was dispersed by analyzers with 75 μm strips.

6.3   Sample Delivery System

To improve our ability to efficiently and reliably deliver PSII sample in our experiments, we developed a new sample delivery system. This system can be run in two different modes: 1) deposit nanoliter droplets of liquid sample on a thin film (similar to a system used at the Linac Coherent Light Source [124]), or 2) deposit a continuous stream of liquid. This system is particularly useful for samples with small volumes or where the sample is easily damaged during measurement, similar to PSII. This cost effective design of this delivery system makes it a practical solution for liquid based samples. This system's simple automation makes it a great resource for experiments using both synchrotrons and benchtop based sources. The physical system can be described in three distinct parts: 1) the syringe pump, 2) deposition system and 3) film replacement. For stepper motor (StepperOnline part #17HS19-0406S and 17HM19-0406S) control and timing, an Arduino microcontroller was used.

6.3.1   Syringe pump

The syringe pump system uses a stepper motor mounted to a trapezoidal thread lead screw to convert rotation (0.9 degree per step) into a linear motion. The syringe is firmly mounted to the base plate and the plunger was pressed by the L beam with each micro step taken (see Figures 6.2 and 6.3). The sample was then transported to the deposition system nozzle using a 19 gauge PTFE tubing with Luer lock connector (Hamilton item # 90619). A smaller diameter nozzle (0.016 in. ID 0.035 in. OD) was taken from a plastic syringe needle (JensenGlobal part number # JG22-0.5XPRO) and glued inside the end of the tubing to produce smaller droplets.
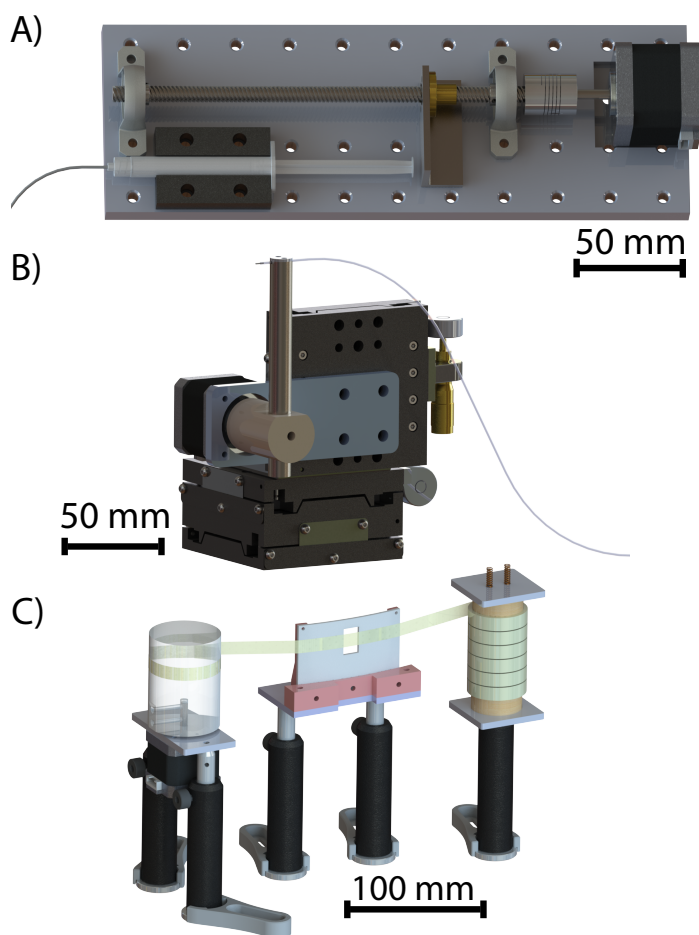
Figure 6.2. A) Top view of syringe pump system including a stepper motor driving a lead screw which translates a metal L-beam to push the plunger on the syringe. Rigid clamps on the syringe and motor not shown for clarity. B) Side view of the tapper assembly (also called the deposition system) is shown with the rotary arm mounted to a three axis stage and holding the plastic nozzle that deposits the sample (in the thin tube) onto the film. C) Side view of the roller assembly is shown with a roll of thin film (right), a Teflon sheet with 25 cm radius of curvature, and the motorized roller for collecting the film (left).3D printed pieces (red) give the Teflon its curvature. Also, springs are shown on top of the thin film roller which can be compressed to vary the tension in the film.

6.3.2 Deposition system

The deposition system uses a stepper motor to rotate an arm which holds the nozzle, Figures 6.2 and 6.3. When depositing individual nanoliter droplets (rather than a continuous stream), the aluminum arm rotates in and the plastic nozzle lightly taps against the thin film (impact of the nozzle should be barely visible). The sample adheres and a small droplet is left as the arm returns to its original position. The nozzle size, the syringe pump step size and rate all determine the sample spot size which we tuned to be approximately 400 μm in diameter. When running with a continuous stream, the nozzle is left in place so that it only lightly touches the substrate. For alignment purposes, the arm/stepper motor system is mounted on a manual 3 axis stage. This allows fine adjustments to the sample position on the film without the need of moving the whole system, and thereby possibly changing the plane in which the film is maintained. This also allows minor adjustments to be made to ensure a soft contact between the nozzle and film.
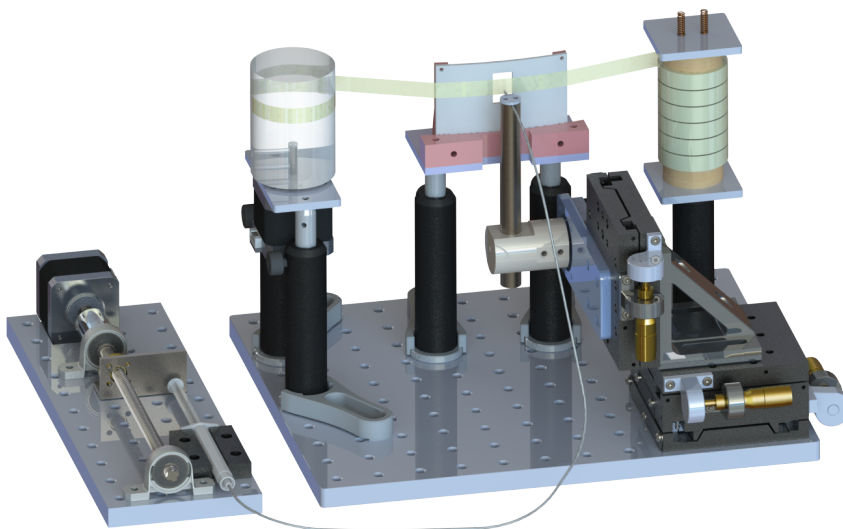
Figure 6.3. The complete sample delivery assembly is shown.

6.3.3   Film Replacement

A thin film of 3.6 μm was used as the substrate for sample transport. Either Mylar or polypropylene was found sufficient. The film was purchased (Chemplex) in 63.5 mm wide rolls. Each roll was cut using a razor blade firmly mounted to a lathe using slow speeds. The resulting strips were 1-1.5 cm wide. Once cut, the roll is placed over a rod whose diameter is slightly smaller than the internal diameter of the film roll. The film is pulled so that it rubs against a Teflon sheet. The sheet is forced to a 0.25 m radius of curvature by mounting it to a 3D printed piece. A 12 mm x 20 mm window in the Teflon was cut as the interaction point where the nozzle deposits the sample on the film. The curvature of the Teflon ensures the film is tight as it is slowly pulled around a winding spool. The spool rotation is actuated by a stepper motor. The winding spool has a large diameter which ensures only slight variations to the spool width as the film is collected over time, thus preventing film loss due to over stepping. Each roll of film contains 6 strips of $\sim$10 mm strips which corresponds to 0.25-0.5 million drops. During measurement these films gave virtually no visible x-ray scattering.

6.3.4   Software control

The Arduino Uno was used for timing the sequence of events during sample delivery. Motor stepping was also controlled by the Arduino with an Adafruit Motorshield with a 12 V powersupply. For our setup, the Arduino activates a sample delivery sequence when it receives a high TTL signal. The sequence consists of 5 stages: 1) the syringe pump is activated, the thin film is moved and the nozzle starts to rotate simultaneously, 2) the arm rotation speed is reduced so that the nozzle makes a soft impact with the film after all other motors finish, 3) after sample deposition, the nozzle returns to its original position 4) a TTL signal is optionally sent to open any optical or X-ray shutters which were closed by the same TTL received initially by the Arduino to start the sequence and 5) wait for another signal to repeat. For

the current setup, sample delivery can be operated at 10 Hz. Faster frequencies are possible if the nozzle arm motion is reduced or if the motorshield, which is limited by the I2C communication, is replaced by a faster system. Microstepping throughout this sequence was necessary to reduce vibrations and control the nozzle impact. The syringe pump should also be set to microstep if nanoliters droplets are desired.

6.4   Conclusions

As the availability of x-ray sources capable of XES continue to increase, so will the demand for x-ray spectrometers and sample delivery tools. A 3D printed x-ray emission spectrometer was developed with von Hamos analyzers fabricated following the protocol outlined in Section 4.3. This spectrometer system is a cost-efficient way to detect x-ray emission lines with high efficiency (factor of 6 greater solid angle over miniXS). This design permits advanced customization while maintaining a low price point and by using the analyzer protocol, can be reproduced for any energy range, given the availability of crystal wafers. By using a fixed geometry inside a He chamber, this system easily integrates into beamlines and laboratory sources for XES. The space around the sample interaction region also allows for the compatibility of a larger range of samples, sample environments and sample delivery systems.

A new automated sample delivery system was also developed. With this setup, sample can be delivered as nanoliter droplets or as a continuous stream or onto a thin film for measurement. This system eliminates waste of liquid samples, automatically replaces spent sample with fresh sample and provides no background scattering, all useful when dealing with metalloproteins. The subsequent chapters will give insight into the capability and results of using these new tools.

7. Time Resolved X-ray Absorption Spectroscopy of Photosystem II

7.1 Introduction

In this chapter a system for performing time resolved x-ray absorption spectroscopy (TRXAS) and its application to PSII is outlined. The setup described enables μs recording of the absorption spectrum using the partial fluorescence yield methodology(see Chapter 3). In this manner, kinetic traces were obtained for x-ray absorption using a single incident x-ray energy at a time. These traces are useful in observing electronic structure changes in the target atom *in operando*. This is particularly useful for metalloproteins as they are often involved in catalytic functions and the element specificity of this measurement type allows the isolated spectroscopic measure of metal centers inside a large organic framework.

As mentioned in Chapter 2 the Kok cycle in PSII consists of a series of distinct oxidative states and results in the splitting of two waters to form diatomic oxygen. The OEC and its surroundings in each S-state transition, triggered by photon absorption, donates an electron to a nearby tyrosine. The system cycles through a series of four flashes (1F-4F) before returning to the initial state. A Mn centered oxidation occurs during the S1-S2 majority, or 1F, transition and debate has arisen about the nature of oxidation in the 2F transition. The only redox effects during the 3F reported by TRXAS has been that of reduction back to the original state (S0 majority) after an initial lag phase. Here we examine each of these transition using TRXAS of the Mn K-edge using 1μs time resolution to achieve the following goals:

1. Prove the functionality of the sample delivery system for time resolved measurements of metalloproteins in solution.

2. Evaluate the validity of time resolved studies of photosystem II without the use of a preflash.

3. Verify the previous results for redox behavior during the Kok cycle.

4. Compare models for different kinetics not considered in the previous reports. [1, 47]

7.2   Experimental Setup

7.2.1   Beamline Parameters

TR-XAS measurements were performed at the beamline 20-ID-C at the Advanced Photon Source. The x-ray beam first goes through high heat load slits which will protect downstream elements from damage. After that, a long toroidal mirror was used to focus the beam which was monochromated by two Si (111) crystals. The beam position from the monochromator was monitored by a diamond beam position monitor from Sydor technologies. The feedback system was used to automatically adjust for minor temporal variations, such as d-spacing changes from temperature. The stabilized beam was slit to a spot size of $\sim$300x300 μm^2. The beam spot size was measured using a YAG crystal with Prosilica camera focused on the x-ray spot. Beam intensity was monitored by the diamond beam position monitor and ion chambers filled with He gas both upstream and downstream of the sample. The beam was attenuated to prevent sample damage by using thin aluminum foils upstream of the beam shaping slits. Damage studies were performed to ensure that the x-ray illumination of the sample will not induce changes in edge position during the exposure period. Previous work done to estimate the damage threshold was used to estimate our maximal dose delivery [97]. Damage studies were also verified with *in situ* measurements for each beamtime. An x-ray energy of 6551 eV was used for all studies shown here.

Calibration of the monochromator was done using potassium permanganate (KMnO4) which has a sharp absorption pre-edge feature at 6543.3eV. The calibration was stored and used to align excitation energies from different beamtimes.

7.2.2 Sample Delivery

At the beamline, the thylakoid membrane fragments stored as a pellet at -80 c (see appendix A) were mixed with a 1 to 1 volume sucrose buffer (pH 6.0) with 500 μM PPBQ. The pellet was resuspended with a paint brush and loaded into a 3 mL syringe. The sample was filled and delivered according the the sample delivery system outlined Chapter 6. The sample was replaced after a full kinetic trace was completed while x-rays and laser shutters were closed by the Arduino. While the sample replacement was carried out in 220 ms for these measurements, it was later optimized to perform sample delivery in under 90 ms allowing for 10 Hz continuous operation. Another improvement made to the sample delivery system after these measurements was the injector nozzle. In earlier versions a tapered plastic nozzle with a 250 μm diameter hole was used instead of a short section of the plastic needle tip with a 400 μm diameter hole as described previously.

7.2.3 Timing

This setup requires synchronization of the laser, stepper motor to refresh the sample, laser diode, and x-ray detector as depicted in Figure 7.2. Typically our measurements were recorded in the 324 bunch mode used at the APS, which means there were 11.37 ns between x-ray pulses. Since our measurements were recorded with 1 μs resolution, synchronization to x-ray pulses was not required. To achieve synchronization, a function generator was used to create a 10 Hz clock which drives the system. This 10 Hz signal was used to trigger the laser's flash lamp and delay generators which trigger the Q-switch (laser output), stepper motor (for sample refreshing), and gate for the 1 MHz signal that provides 1 μs resolution for data collection. X-rays
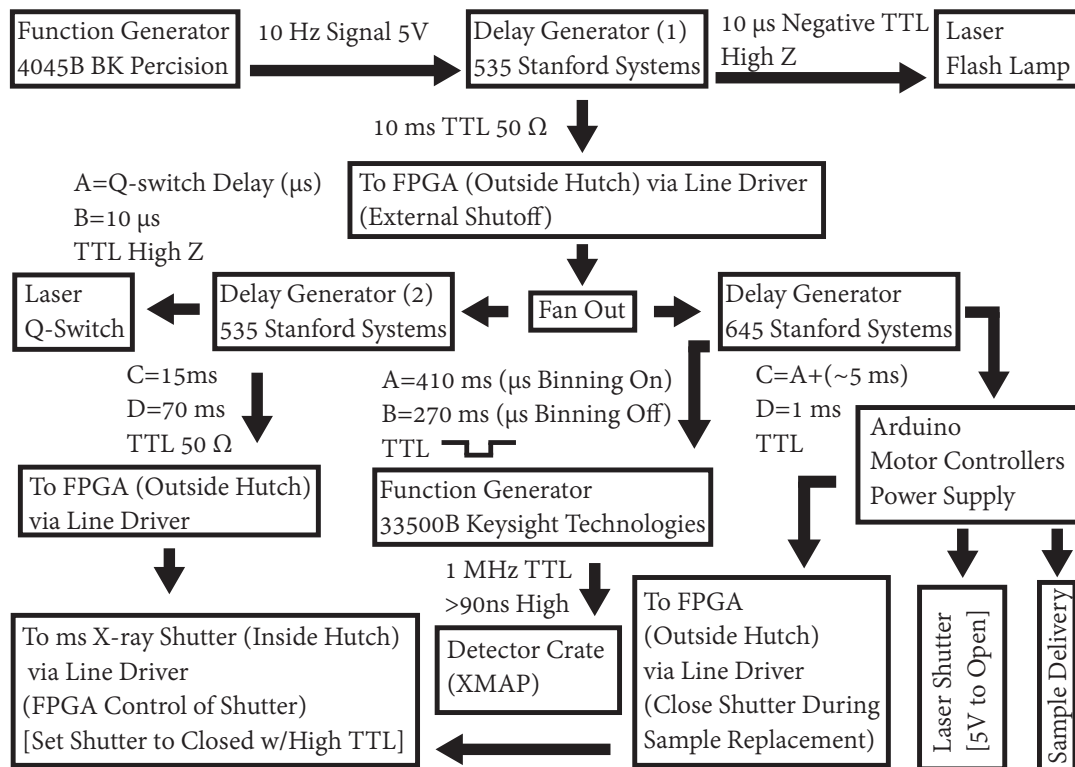
Figure 7.1. Diagram of the electronic timing setup with the 10 Hz Function Generator setting the clock used for all timing.

were recorded using silicon drift detectors and laser pulses were recorded by an optical diode. These signals were recorded using synchronized digital pulse processors, known as an xMap card, and stored as time-stamped photons which can be used to reconstruct kinetic traces. Synchronization with the motor was verified by stopping the 1 MHz clock used to time-stamp photons, creating a single bin with a longer dwell time and photon count, immediately before motor motion.

7.2.4 Excitation Scheme/Laser setup

The laser illumination was done using 2 fiber optics focused to a FWHM ~500 micron diameter focal spot on the sample with a power output of ~500 μJ (4 mJ/mm^2)

each during a 5-8 ns pulse. Both sides were illuminated with an angle of incidence of the laser being ∼10 degrees offset from the x-rays. The front laser/x-ray overlap was verified using a YAG scintillator with an optical camera. Additionally a second fiber optic coupled from the same laser was positioned to overlap with the position of the first and x-rays using a piece of burn (photoactive) paper. Overlap on the sample with the same vertical height as the x-ray beam ensures overlap between the three beams. The interaction region was fixed in space using a short depth of focus (∼50 µm) camera. The sample deposition was easily adjusted to deposit in the interaction region for the laser/x-ray overlap using the manual stage, see Section 6.3. During measurement, the sample stayed in a lead tape covered nozzle which rotated in to deposit the sample just before measurement.
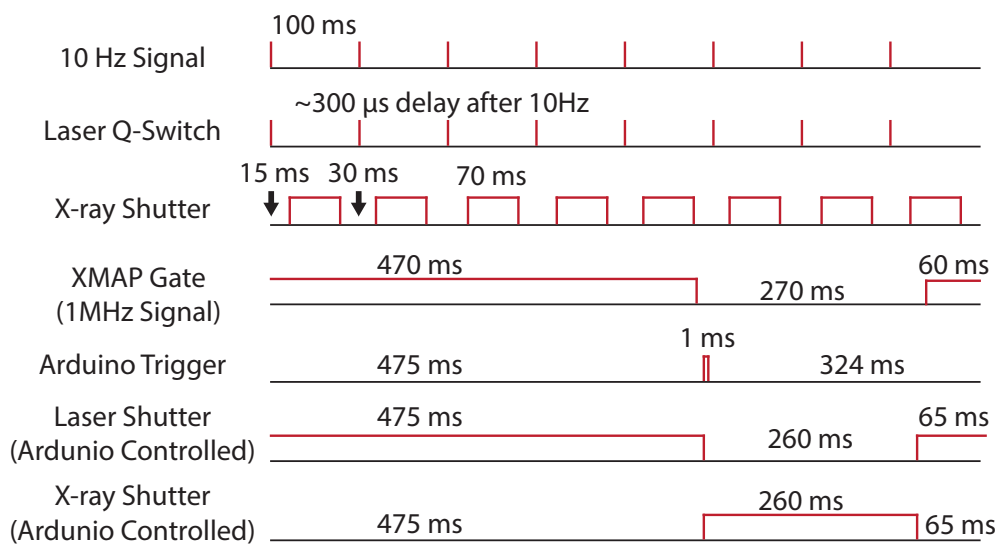
Figure 7.2. Diagram of the timing sequence that runs the experimental setup. Note that the laser shutter is open when high and the x-ray shutter closes when either of the two signals are high (5 V).

7.3   Data Processing

The raw kinetic trace of absorption was collected with a resolution of 1 μs with each trace being aligned by the signal from the diode recording the laser flash. Data processing of the traces consisted of 4 steps: 1) Data were binned (20 μs) 2) An estimation for the variance in the signal was calculated, 3) a linear background was subtracted and 4) offset was incorporated. The data were binned by summing the data around the center point and splitting the endpoints to their nearest neighbors. Estimation of the variance in the signal was done using 1000 points (1 ms) of data just before each corresponding laser flash. The linear background was found by a least squares fit to 5 ms of data after the initial kinetics (considered to be 3 ms for all data except 3F, which used 6 ms) and subtracted from the signal. The zero point for each fit was defined as the average of the 1000 points (1 ms) just before the laser flash and was used as the initial point for the kinetic traces. The models were then fit to the first 3 ms of data after the flash for all transitions except 3F, which used 6 ms.

7.4   Models Considered

Here we considered five models to explain the 3F transition, S3-S0 state transition majority, kinetics. The first consideration was an obvious one consisting of a transition of a sample population A to that of B. The rate equation for this model was then simply written as

$$A \xrightarrow{k_1} B \tag{7.1}$$

where k_1 is the rate constant for the transition, or one over the time constant τ_1, of a population from state A to state B. The fractional population in state A was then found by solving the differential equation

$$\frac{dA}{dt} = -k_1 A \tag{7.2}$$

whose solution can be easily found to be

$$A = e^{-k_1 t} \tag{7.3}$$

The population B is then simply 1-A given given the conservation of the entire population

$$B = (1 - e^{-k_1 t}) \tag{7.4}$$

The change in fluorescent intensity between state A and B is, ΔI_{B-A}, can be written as

$$\Delta I_{B-A} = I_B - I_A \tag{7.5}$$

where I_x is the fluorescence of the x state. Here it is important to note that population A is a distribution of S-states and not all S-states change in going from A to B.

With this we can rewrite the intensity predictions of model 1 as

$$I_{M1} = \Delta I_{B-A}(1 - e^{-k_1 t}) \tag{7.6}$$

Note that this model, and all others considered, were offset such that the initial intensity, I_A, is zero and all the OEC centers in the initial state A at time t=0, or at the time of the 3rd laser flash This kinetic model would suggest that the transition is actually a one step process from S3 to S0 triggered by the oxidized tyrosine Y_Z becoming reduced.

The second model used was very similar to the first except it considers two independent first order reactions including Equation 7.1 and

$$C \xrightarrow{k_1} D \tag{7.7}$$

In this case Model 2 is written as

$$I_{M2} = \Delta I_{B-A}(1 - e^{-k_1 t}) + \Delta I_{D-C}(1 - e^{-k_2 t}) \tag{7.8}$$

One interpretation of this model is the mixing of two different populations, S2 and S3, leading to two independent initial and final states, S2-S3 and S3-S0, which are both triggered at the same time.

Both models three and four involve three populations with one intermediate. Here we assumed a similar system of rate equations with three populations, A, B and C with two rate equations k_1 and k_2 as shown:

$$A \xrightarrow{k_1} B \xrightarrow{k_2} C \tag{7.9}$$

where population A was the initial state, B was an intermediate necessary for the formation of C. These lead to the following differential equations:

$$\frac{dA}{dt} = -k_1 A \tag{7.10}$$

$$\frac{dB}{dt} = -k_2 B + k_1 A \tag{7.11}$$

$$\frac{dC}{dt} = k_2 C \tag{7.12}$$

These equations were then solved to find the fraction of the total population in each of these states. Assuming k_1 not to be equal to k_2 the differential equations then become the following:

$$A = -e^{k_1 t} \tag{7.13}$$

$$B = \frac{k_1 (e^{-k_1 t} - e^{-k_2 t})}{k_2 - k_1} \tag{7.14}$$

$$C = 1 + \frac{k_1 e^{-k_2 t} - k_2 e^{-k_1 t}}{k_1 - k_2} \tag{7.15}$$

From these populations we can form two different models. One where the the intermediate doesn't play an active role in the absorption of the Mn atoms,

$$I_{M3} = \Delta I_{C-A}(1 + \frac{k_1 e^{-k_2 t} - k_2 e^{-k_1 t}}{k_1 - k_2}) \tag{7.16}$$

and one where it does,

$$I_{M4} = \Delta I_{B-A}\frac{k_1 (e^{-k_1 t} - e^{-k_2 t})}{k_2 - k_1} + \Delta I_{C-B}(1 + \frac{k_1 e^{-k_2 t} - k_2 e^{-k_1 t}}{k_1 - k_2}) \tag{7.17}$$

In the case of model 3 a passive, in terms of electronic structure, intermediate has been interpreted as a deprotonation event [1] while results of model 4 were not reported or discussed.

One last model was considered which included the passive intermediate for the S3-S0 and a single first order reaction that matched the fit of 2F-3F written as

$$I_{M5} = \Delta I_{C-A}(1 + \frac{k_1 e^{-k_2 t} - k_2 e^{-k_1 t}}{k_1 - k_2}) + \Delta I_{E-D}(1 - e^{-k_2 t}) \qquad (7.18)$$

where D is treated as the population distribution in 1F, or S2 state majority, such that the change in absorption during 1F-2F were used to constrain the time constant to be no more than 2 sigma from the best fit found for the 1F-2F, S2-S3 state majority, transition.

7.4.1 Fitting procedures

Fitting of the data included the following methods. The python library LMFIT was used to find the best fit given an input function [126]. The best fit was found by minimizing the sum of the residuals squared, nonlinear least square fit, while adjusting the free parameters. The first four models considered were not constrained during fitting with the exclusion of the time constants being forced to be positive non-zero values. The final model was constrained based on parameters found for the 2F-3F state change and is discussed later.

The error for the free parameters in the best fit for each model was then evaluated using an F-test regression analysis. This was done by comparing the best fit model with an alternative model where one of the free parameters is fixed. The fixed parameter in the alternative model was then tested under a range of values. This continues until the two models differ enough such that they can no longer be reconciled by the reduced degrees of freedom and that the models are considered different within some confidence interval. For the data reported in this chapter, the confidence interval corresponds to a one σ variation (68%) for each parameter. The F-test value is expressed as

$$F = (\frac{\chi^2_{fixed}}{\chi^2_{bestfit}} - 1)\frac{N - P}{P_f} \qquad (7.19)$$

where F is the confidence that the two models are statistically different, χ^2_{fixed} and $\chi^2_{bestfit}$ are the chi-squared values for the model with a fixed point and the best fit respectively, N is the number of data points, P is the number of free parameters in the best fit and P_f is the difference in the number of free parameters in the best fit and fixed models. It was also important to note here that the F-test does not exhibit the same dependence on the way the variance was calculated since variance cancels out in the ratio of χ^2 values.

7.4.2 Evaluation of Fits

The comparison of the quality of fit between the presented models were measured by both Akaike information criterion (AIC) and Bayesian information criterion (BIC) [127]. While a reduced χ^2 can also be used to judge fit quality, the value of this parameter was found to be dependent on the range of points used to calculate the variance. While this led to small variations in the uncertainty, this difference could offset one model or another to be closer to the ideal value 1, thus requiring a more robust method for model comparison. While both AIC and BIC depend on the χ^2 value, the dependence on the variance will cancel when comparing the difference. While AIC will find the best fit more often, the more conservative (in terms of a higher penalty for free parameters) BIC can help against over fitting. Typically both AIC and BIC are used together and a difference of 4 between the two models is good indication that the lower value model is a better representation of the data, a value of more than 6 is strong evidence (95%) in favor for the lower fit.

$$AIC = N \ln(\frac{\chi^2}{N}) + 2N_{var} \tag{7.20}$$

$$BIC = N \ln(\frac{\chi^2}{N}) + \ln(N)N_{var} \tag{7.21}$$

Where N is the number of data points, and N_{var} is the number of variable parameters used in the fit. The equation for χ^2 is given as

$$\chi^2 = \sum_{i=1}^{N} \frac{(O_i - F_i)^2}{\sigma_i^2} \tag{7.22}$$

where O_i and F_i are the ith observed and fit values respectively and σ^2 is the variance.

7.5   Results
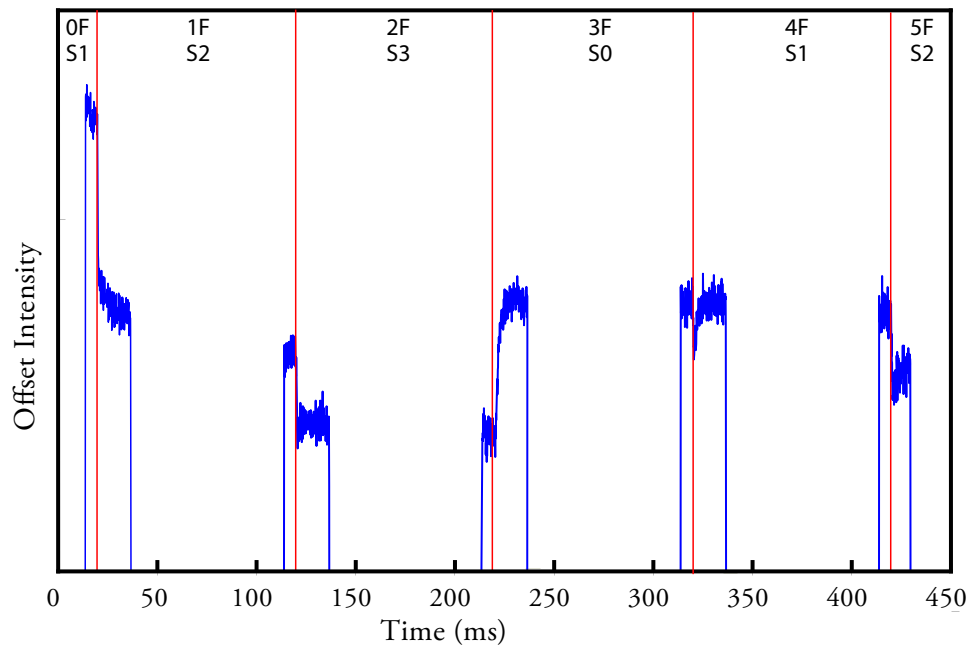
Figure 7.3. Time traces binned to 50 μs showing the transitions between the different states from two beamtimes. The red line indicates the timing of the laser flash as recorded by the diode and the blue shows the offset Mn Kα fluorescence intensity. Gaps in data represent where the x-ray shutter was closed. Flash number is shown as xF where x is the number of laser pulses. The majority S-state is also shown.

A kinetic trace of undamaged PSII was taken with 1 μs resolution is shown in Figure 7.3. Across the kinetic trace 5 flashes (1F-5F) of light were used to advance the sample through all S-state transitions and returning to the S1-S2 majority transition.

Clearly visible are the different s-state transitions with the prominent S1-S2 majority transition, or 0F to 1F transition, being the first transition recorded.

This setup is very different than the methodology used previously where a very large series of wells were individually filled and each one was only used to measure one S-state transition [1]. Instead we have a constant delivery of fresh PSII to the interaction point where all S-state transitions are recorded once for each sample. This greatly reduces the burden of sample preparation for metalloprotein delivery. We note here that while two beamtimes were used to collect the data shown, less than one beamtime worth of measurement is represented here. This is due to technical issues at the beamline and the need for on-the-fly adjustments to the prototype sample delivery design. The more consistent and stable form of the sample design resulting from these adjustments is reported in Chapter 6.

To evaluate the advancement of the sample a fifth flash was recorded. By using the cycle of flashes we were able to cycle through the different S-state majorities until the initial S1-S2 is reached. By comparing the amplitude of the absorption changes in the two transitions we can estimate the percent of the initial population transitioning from the 0F to 1F that also shows up in the 4F to 5F transition four flashes later. By assuming each state has the same probability of advancement, P, we find

$$\Delta I_{5F-4F} = \Delta I_{1F-0F} P^4 \tag{7.23}$$

where ΔI_{5F-4F} is the fluorescence intensity change from 4F to 5F and ΔI_{1F-0F} is the fluorescence intensity change from 0F to 1F. Since the transitions just before 5F either have slow opposite changes in absorption, 2F-3F, or have only weak changes, 3F-4F, the contribution to the change in overall fluorescence based on the convolution of 4F-5F with either of these is ignored.

Given that the intensity changes from 4F to 5F found were between 42-52% of 0F to 1F, an advancement of 81-85% was found. We do note that our data were measured without a preflash. The importance of a preflash is to obtain nearly 100% in the S1 state [128]. When left in the dark, both the S2 and S3 transition back to S1 [15]. The population initially in S0, however, will remain in S0 without advancement. For

samples without a preflash, if we assume a random initial distribution of S-states then about 25% of the dark adapted population will be in S0 and 75% will be in S1. When illuminated both the S0 and S1 PSII centers will advance with the S2 and S3 states transitioning back to S1. This creates a high percentage of S1 as the initial state. Here we show the convolution of all S-states based on this advancement in Table 7.1. Here we note, that according to this model we achieve nearly the same S3-S0 state transition percent, 43%, in the third flash as the data obtained previously [1], 47%, despite a preflash being performed. This is due to a large population of PSII centers in that report that do not advance past S2. While it is unclear the cause of such a high population of states that didn't advance, it is clear that the method for advancement and sample preparation is at least matched with previous data for this important transition.

Table 7.1.
S-state population percentages based on number of flashes is shown. The advancement model assumes 83% advancement for all states, no double hits and the initial population of 1F is as shown. All values are rounded such that slightly more/less than 100% population is found for some states.

S-state Convolution by Flash				
	S0	S1	S2	S3
0F	25	75	0	0
1F	4.3	33.5	62.3	0
2F	0.7	9.2	38.4	51.7
3F	43.0	2.2	14.2	40.1
4F	41.0	36.1	4.2	18.7
5F	22.5	40.2	30.6	6.7

In Table 7.2 the fits for a single kinetic transitions are given. Here our results are in good agreement with that reported in literature for time resolved measurements. This supports the idea of a single step toward oxidation for the 1F state transition.

For the 2F transition a lag phase was reported using D_2O exchange [47] and only a small lag was found for H_2O which indicated a passive intermediate time constant of 20 μs. That such an intermediate can be reliably obtainable H_2O after smoothing and binning to 20 μs is uncertain, however the increase in this delay with D_2O substitution does support the notion of sequential kinetics during this transition. This is in line with a deprotonation event responsible for the Mn coordination change [33]. Using the Model 3 for this transition resulted in the best fit collapsing to a single kinetic, τ_1 becoming zero, and unreasonable uncertainties on all parameters such that we cannot evaluate this model based on our current uncertainties and bin size. The 3F transition as a single rate yields a longer than expected time constant and discussed later. For the 4F transition we also find that the time constants are consistent with those reported previously and 5F time constant is similar to that found in 1F though slightly smaller.

Table 7.2.
S-state time constants determined experimentally for electron transfer in μs. Errors given are in the 68% confidence interval.

Single First Order Reaction Fits		
	τ_1 (μs)	ΔI_{B-A}
1F	311 (+27/-26)	-0.052 (+/-0.0008)
2F	380 (+60/-50)	-0.023 (+/-0.0008)
3F	3600 (+490/-400)	0.052 (+0.004/-0.003)
4F	76 (+65/-53)	-0.0083 (+/-0.0007)
5F	228 (+43/-40)	-0.022 (+/-0.0007)

In Figure 7.4 the best fits for models 1-4 for the 3F transition are shown. Model 1 of a single first order reaction has larger residuals in the first ms of the data leading to a worse fit quality, an observation supported by comparing AIC and BIC values obtained for the best fits in Table 7.3. As both AIC and BIC for Model 1 are quite high

in comparison to the other models we exclude this model from serious consideration. Through AIC and BIC analysis, the data are best fit by models 2 and 4 which collapse to become the same function. These seem to account best for the reduced fluorescence during the first 0.5-1 ms. Model 3, while it has slightly higher AIC and BIC values, is still considered here as a viable representation of the data due to the large level of noise in the system.

In Model 2, where two independent single reactions occur, the values obtained for the best fit are rather extreme. If Model 2 were an accurate representation of the physical system, the changes in absorption, ΔI_{B-A}, caused by the intermediate would be larger than that of S1-S2. Use the value within the 68% confidence interval
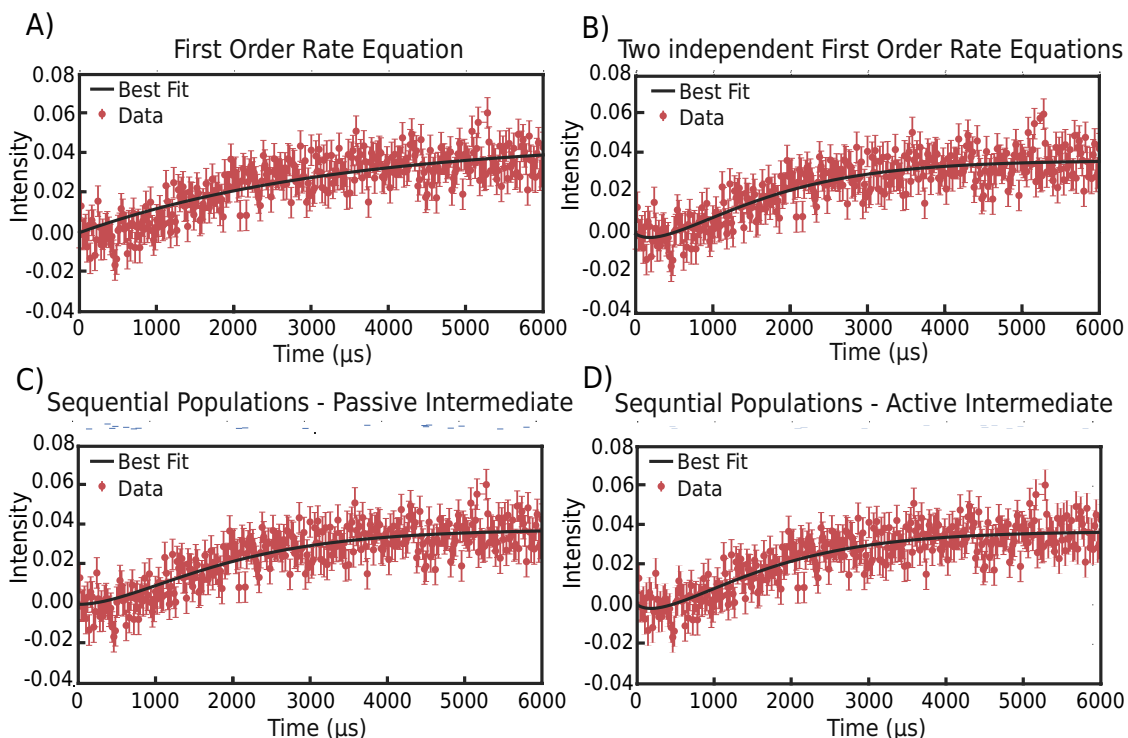
Figure 7.4. Best fits found for the four models considered, namely: A) single first order rate equation, B) two single first order rate equations, C-D) sequential populations without and with an intermediate that changes absorption respectively. Note the fits for B) and D) collapse to the same function. The 3F transition shown here is binned to 20 μs.

Table 7.3.
The best fit parameters and their uncertainties are shown for the 3F transition using models 1-4. Uncertainties correspond to a 68% confidence interval.

Single First Order Reaction (AIC-43 BIC-50)			
	$\tau 1$ (μs)	ΔI_{B-A}	
Best Fit	3600	0.052	
Uncertainty	+490/-400	+0.004/-0.003	
Two First Order Reactions (AIC-0 BIC-14)			
	$\tau 1$ (μs)	$\tau 2$ (μs)	ΔI_{B-A}	ΔI_{D-C}
Best Fit	590	1000	-0.08	0.1
Uncertainty	+260/-360	+360/-280	+0.05/-0.13	+1.2/-0.05
Sequential - Passive Intermediate (AIC-10 BIC-21)			
	$\tau 1$ (μs)	$\tau 2$ (μs)	ΔI_{C-A}	
Best Fit	1000	1000	0.038	
Uncertainty	+360/-280	+350/-290	+/-0.001	
Sequential - Active Intermediate (AIC-0 BIC-14)			
	$\tau 1$ (μs)	$\tau 2$ (μs)	ΔI_{B-A}	ΔI_{C-B}
Best Fit	590	1000	-0.014	0.036
Uncertainty	+780/-230	+360/-660	+0.004/-0.032	+/-0.001

of -0.03, or even at 95% with -0.017 (not shown in Table 7.3), then the absorption change is still large enough the second single rate cannot be explained by a small population undergoing an S2-S3 transition. This leaves a strong change in absorption on the same scale as that of oxidation. While full oxidation of a Mn atom may occur during the S3-S0 transition to obtain Mn^V, this oxidation state assignment is not supported by the lack of a strong pre-edge feature in previous work [1]. This would indicate that either S3 is not in the Mn_4^{IV} state or that other changes are responsible for this change in absorption. While several factors are shown to affect the electronic

structure, and thus ionization energy levels of the electrons, they are typically weaker changes than that observed for full oxidation. Given these results, we conclude that Model 2 could be plausible, though no physical picture can currently explain this behavior and more data would be required to confirm this result.

Model 3 includes a lag phase caused by the formation of a passive intermediate. This model, and that of Model 1, were the only ones suggested by the only other group to publish TR-XAS of PSII [1, 47]. As can be seen in Table 7.3, the AIC and BIC values for the fit are much improved over that of the single first order rate model. Even so, the model doesn't freely fit the time constant found previously for this transition, $\tau 1 = 300$ μs and $\tau 2 = 1.6$ ms. While we consider the small differences in pH, 0.3, unable to account for these drastic changes, we do consider the differences in x-ray excitation energy to be a more plausible explanation source for the discrepancy. In Dr. Michael Haumann's 2005 paper [1], the isobestic point for the second flash, 6556 eV, to eliminate any interference with sample that didn't advance on the second flash. Here, we used 6551 eV. A discussion of the effects of a convolution of states is considered later. Given the noise, size of the binning and smoothing performed on the data, it is unclear if the oxidation, or reduced signal intensity, occurs at that energy point as well. While we do not rule out the possibility of consistent findings, we also consider alternative models with lower AIC and BIC values.

Model 4 is a good balance between a good fit and reasonable values. This model suggests an active intermediate which causes small changes to the absorption, -0.014 as the best fit, -0.01 as σ and -0.007 for two σ. This is much less than a full oxidation and could be interpreted as changes in the electronic structure surrounding the Mn atoms. While a more plausible model for the 3F transition, the fit parameters are widely varying and require more data to narrow the range of possible values for the free parameters. Without a narrowing this range of expected values, it would be difficult to suggest the proper mechanism for the intermediate, though we do not exclude the possibility deprotonation as suggested by the previous work.

To check if Model 3 combined with a sub-population undergoing S2-S3 after the third flash is feasible, Model 5 was also evaluated. The fits to model five when the S2-S3 component was not constrained led to a negative shift of 0.6 the magnitude obtained for the 2F transition. This suggests nearly equal advancement after the second and third flashes which is not possible with an advancement of 83%. When Model 5 was constrained so that the amplitude of the 2F contribution was constrained to be ~19% of that found during 2F, the time constant obtained for the fit was more than 2 sigma away from that obtained during 2F. In conjunction with the fit not not freely choosing parameters that fit the physical model, the AIC and BIC values were also much higher than those obtained either by Model 2 or Model 4, suggesting this is indeed a worse fit to the data.

Table 7.4.
The best fit parameters are shown for model 5 using the constraints on the time constant and amplitude for the 2F contribution during 3F.

Sequential - Passive Intermediate With S2 (AIC-5 BIC-24)					
	$\tau 1$ (μs)	$\tau 2$ (μs)	ΔI_{C-A}	τ_{S2} (μs)	ΔI_{E-D}
Best Fit	930	900	0.041	280	-0.0044
Uncertainty	+290/-60	+/-60	+/-0.001	+100/R	R/-0.0006

[R] Best fit value found was the constraint used

7.6 Conclusions

Through this TRXAS work we were able to prove a methodology for recording changes in x-ray absorption for metalloproteins at the μs time scale. We also show that the sample delivery system, which has been subsequently improved, enables an efficient measurement in a tight interaction region in a reproducible way.

From these studies we show good advancement (approximately 83%) of PSII without the need for preflash and achieving similar S3-S0 transition percents to preflashed

data. This is extremely important validation for ongoing time resolved work performed at synchrotrons and XFEL sources. We also verify the results obtained for TRXAS for both the S0-S1 and S1-S2 state transitions. Our data supports the 2F state transition as a single reaction, though the possibility of a short lived intermediate is not excluded. For the 3F transition we give some support to models containing an intermediate. Given our quality of data we do not believe we can exclude the passive intermediate model reported previously [1] but we do note that fits to our data do indicate that an active intermediate is preferred. We acknowledge the fact that there will be some convolution of S-state before 3F and give reasonable arguments why these effects alone are not likely to explain the data.

8. Time Resolved X-ray Emission Spectroscopy of Photosystem II

8.1 Overview of Kβ Emission Spectroscopy of Photosystem II

Non-resonant Kβ XES can provide information on the spin state, structural changes, covalency and ligand type of target atoms in a sample. Splitting of the two Kβ mainlines in 3d transition metals is mainly due to the spin state of the central atom, which can be used as a probe of the oxidation state for high spin systems, such as the Mn cluster in photosystem II (PSII) (see Section 3.2.4).

For TRXES presented here, both Kβ mainlines are recorded at specific points in time to capture the different states of PSII. The abilities of the new three crystal spectrometer was demonstrated and a feasibility study was conducted to understand what level of data was required to find statistically significant shifts based on the expected shift size. This was used to evaluate the capability of a synchrotron to determine if a statistically significant S_2 to S_3 transition could be reasonably obtained. This transition has had conflicting reports on the level of first moment shift and is important for the oxidation state model, see Section S2-S3.

In addition, D_2O exchange was used. A D_2O exchange experiment may not be able to distinguish between the kinetic models used in 7.4 depending on the kinetic isotope effects, it could be used to evaluate the claim of deprotonation during the S2-S3 transition by the existence of a lag phase. While such a lag phase was not detectable in data reported in Chapter 7 for H_2O, Zaharieva et al. reported a 26 μs delay for H_2O and a 117 μs delay in D_2O [47] using TRXAS. Capturing this difference with TRXES may give a more useful insight into the nature of this delay in oxidation.

Additionally, previous TRXES measurements showed a reduction in the first 50 μs [106] which may show a kinetic isotope effect. We also present a feasibility study for studies of this transition.

The goals of the work presented in this chapter were the following:

- Demonstrate the capability of instrumentation developed in Chapters 6.

- Conduct a feasibility study for new work with PSII using the new detection system and evaluate if the following are obtainable:

  - Statistically significant shifts between the S2-S3 state that are robust.

  - Validation of a lag phase between the S2-S3 state.

  - Understanding isotopic effects S2-S3 and S3-S0 using D_2O exchange.

8.2 Experimental Setup

8.2.1 Beamline Parameters

Table 8.1.
Beamline parameters for x-rays used for TRXES of PSII.

	Beamline Parameters
Excitation Energy	Peak energy 7.85 keV, FWHM 500 eV
X-ray Spot Size	$\sim$45x100μm^2
Pulse Length	22μs
Photon Flux	1.5x10^{11}
Dose per Pulse	$\sim$7 x 10^7 photons/μm^2
Repetition Rate	$\sim$20Hz

A laser pump, x-ray probe emission setup is described using the Advanced Photon Source at Argonne National Lab, beamline 14ID-B [117]. The laser delivers a 527

nm pulse to the sample at 10 Hz. A power density for a laser pulse was 11 mJ/mm^2 was obtained by coupling the light into a fiber optic and focusing the emitted light onto the sample in a $\sim$220 μm diameter spot. X-ray triggering of a 22 μs pulse train is used in conjunction with laser triggering to ensure proper excitation of PSII. The short pulses were delivered using a high heat load chopper and ms shutter to allow only a small pulse train through. Overlap of the two signals were established using a phosphor screen in the interaction region.

This setup uses a wide photon energy range, with a grazing angle mirror to create a high energy cutoff, known as a pink beam. This allows a higher dose to be delivered in a very short amount of time, which has been shown previously to increase the damage threshold for photosystem II [97]. Two sets of Kirkpatrick-Baez (KB) mirrors where used. These mirrors are dynamically bent with one mirror focusing the beam in the vertical direction and the second in the horizontal to improve focusing while a second set is used to collimate the beam. The lowest energy setting for the U27 undulator, corresponding to an 11.7mm gap was used during calibration of the spectrometer.

8.2.2 Timing

Triggering and timing of the laser and x-ray pulses are controlled using a field programmable gate array. The x-ray temporal width is first shortened using a high heat load chopper to remove x-rays between probe exposures. The separate pulse trains are then isolated by millisecond shutter to ensure the proper time of arrival of the x-rays. The timing of the laser with the x-ray shutter are verified using a diode at the interaction region. An x-ray delay of 500 μs after one and two flashes was recorded, while 50 μs, 200 μs, 500 μs and 40 ms delays were recorded after three flashes. The dark adapted S1 state with no laser flash was also recorded.

8.2.3 Sample Preparation and Delivery

Sample preparation deviated from that reported in Appendix A in that the last re-suspension and centrifugation was done in a sucrose buffer with D_2O at a pD of 6.0. At the beamline, the thylakoid membrane fragments were stored as a pellet on dry ice until thawed in an ice water bath and mixed with a 1 to 1 volume D_2O sucrose buffer (with 500 μM PPBQ) to pellet. The sample was then loaded in a syringe into the system described in Chapter 6. To incorporate the sample delivery system with the spectrometer, the sample delivery system was mounted upside down, or vertically flipped, from the orientation shown in Chapter 6. There was no noticeable difference in performance in either orientation.

8.2.4 Spectrometer

The integration of the spectrometer described in Chapter 6 was relatively simple. Two eyelets were used at the front of the spectrometer to ensure a proper location for the x-ray interaction point. The sample position was then located using a 3-D printed alignment tool which was inserted in the dowel pin holes previously used by the eyelets on the spectrometer. This tool allowed the center plane of the spectrometer to be established without the need for scanning the sample up/down stream. A high resolution camera was then used to maintain the interaction region by using a short (50 μm) focal depth. A Pilatus 100k is then stepped toward the spectrometer to find the maximum focus of the three crystal analyzers.

Calibration of the double crystal Si(111) monochromator was done using a single point calibration from the absorption edge of an iron foil. Elastic scatter from the sample was then used to calibrate the spectrometer in 2-3 eV steps. The scattering peak positions were then interpolated using 4th order polynomial to convert pixel position to emission energy.

8.2.5 Data Collection

Here we describe the collection of three different time points during the Kok cycle. These time points include:

- F0 (S1) - no Laser Exposure

- F1 (S2) - 500 μs delay after a single laser flash to x-ray exposure

- F2 (S3) - 500 μs delay after the second laser flash to x-ray exposure

- F3$_{50}$ (S4$_{50}$) - 50 μs delay after the third laser flash to x-ray exposure

- F3$_{200}$ (S4$_{200}$) - 200 μs delay after the third laser flash to x-ray exposure

- F3$_{500}$ (S4$_{500}$) - 500 μs delay after the third laser flash to x-ray exposure

- F4 (S0) - 40 ms delay after the third laser flash to x-ray exposure

Each of the these S-states were recorded for each sample syringe loaded into the sample delivery system. Two images of each state were taken as a systematic cycling through to the s-states was performed. Each image captures 800 x-ray pulse exposures, each with fresh sample and each with the same delay. The first state recorded after a new syringe was loaded into the system was also cycled to prevent any systematic error.

The choice of all S-states were matched to that of previous work for comparison [106].

8.2.6 Data Analysis

For all data presented in this chapter, emission spectra were obtained using a Pilatus 100k. The images were processed by using a fourth order polynomial fit to the elastic scattering recorded in two eV steps across the detector. The pixels were then assigned energies, extracted and binned into 0.1eV. The spectra were then only

smoothed and background subtracted for visualization of the shift (described in text), all other data were processed using raw values. A first moment value was obtained for each recorded image and the analysis was done over the range of 6485-6495 eV except as noted in the text. One-way analysis of variation (ANOVA) is then used to test the null hypothesis that the first moment measurements of the two S-states represent the same population. In this way, the significance of the shift is then gauged by the confidence obtained. This is calculated as the F statistic which compares the between-group variability, MS_B, to that of variability within a group, MS_W, to obtain

$$F = \frac{MS_B}{MS_W} \tag{8.1}$$

where

$$MS_B = \frac{\Sigma_i n_i (\bar{y}_i - \bar{y})^2}{g - 1} \tag{8.2}$$

and

$$MS_W = \frac{\Sigma_i \Sigma_j (y_{ik} - \bar{y}_k)^2}{N - g} \tag{8.3}$$

where i is the index for each group, k is the index for each measurement in the corresponding group k, where n_i is the number of measurements in the ith group, N is the total number of measurements, g is the number of groups, y_{ik} is the value of the ith measurement in the kth group. Using the degrees of freedom the F statistic is then used to find the confidence interval for the null hypothesis.

Power analysis for one-way ANOVA was performed using the program G*Power. A power analysis can be used to estimate the number of measurements necessary to find a statistical significance between the measurement of two different population means. More specifically, when designing the experiment one can choose the power, or level of confidence that a false negative will not occur. A typical power is 80%, but can vary depending on the needs of the experiment. In this manner, the rejection of the null hypothesis is based on the confidence interval obtained from the F statistic. If one-way ANOVA fails to reject the null hypothesis, then this represents an 80% certainty of that rejection being correct. The equation for this analysis is

$$n = 2(Z_{1-\frac{\alpha}{2}} + Z_{1-\beta})^2 \left(\frac{\sigma}{|\mu_1 - \mu_2|} \right)^2 \tag{8.4}$$

where n is the number of total measurements required for the experiment (half in each of the two data sets being compared), α is the acceptable probability of type I error (false positive), β is the acceptable type II error (false negative), Z is the Z-score, μ is the population mean, σ is the mutual SEM. Here we use an α of 0.05, or 5%, and a beta of 0.2, or 20%.

8.3 Spectroscopic Results from Photosystem II

To demonstrate the capability of the spectrometer and sample delivery systems, we measured Mn Kβ emission from the oxygen evolving complex (OEC) of photosystem II at room temperature. The OEC, which features a unique Mn4CaO5 core, was chosen as it has a very dilute Mn content ($\sim$500 M) which damages rapidly [97]. Precautions were taken to only provide non-damaging doses of 22 μs to the sample.
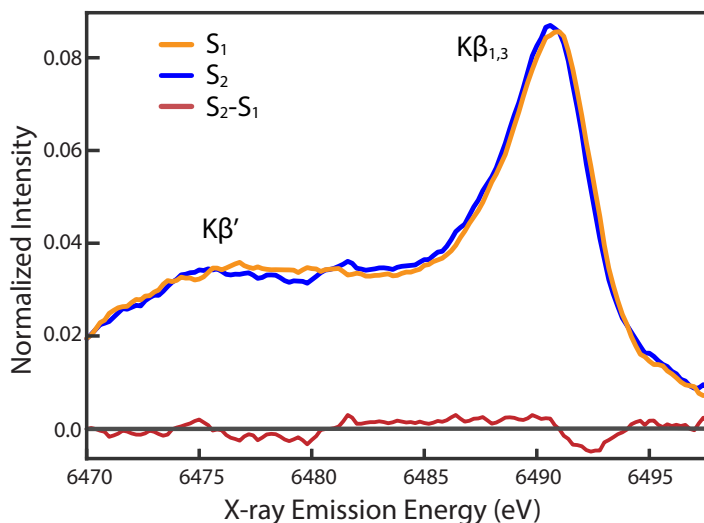
Figure 8.1. The Kβ X-ray emission spectra of the Mn atoms in the OEC is shown for the S1 and S2 states. The intensity was normalized by area under the curve between 6470-6495 eV. The difference between the two states is also shown to emphasize the visibility of a small shift.

Using TRXES, we were able to capture the shift between two different oxidation states, S1 and S2, of the oxygen-evolving complex (OEC) at room temperature. The

spectra, after smoothing using a 9 point boxcar average and a linear background subtraction, are shown in Figure 8.1. This figure shows a difference spectra indicating a shift in the $K\beta_{1,3}$ peak from S1 to S2 towards lower energy, or oxidation. This shift indicates an average higher oxidation state (reduced localized spin density) for the average Mn atom in the OEC which is in agreement with previous results [18, 28, 106].

A first moment analysis was also performed for the S1 and S2 states on raw data. Here, one-way ANOVA was used used to test the null hypothesis that the two states represent the same population, a hypothesis which is here rejected if the probability is less than 5% ($p<0.05$). In the case of S1-S2 we show that the p value is less than 0.01. This shift was observable with a small data set containing a total photon exposure of $\sim$1 seconds of integrated signal, or $<7\text{x}10^{15}$ photons, per S-state. This is between $\frac{1}{2}$ to $\frac{1}{4}$ of the photons used in each of the four individual data sets in a recent report [106] where data sets had to be combined to achieve this level of confidence. The capture of this shift with such a small data set shows the effective nature of our setup and verifies the capability of this simple system to see detect small shifts from a dilute sample using the three crystal spectrometer and to reproducibly deliver small volumes accurately with the sample delivery system.

As the FM is dependent on a fairly arbitrary energy range, a map of p-values was also obtained through one-way ANOVA analysis for the S1-S2 transition with the y-axis representing the start and x the end of the energy range used, Figure 8.2. Along with that map of the probability of rejecting the null hypothesis, a map of the shift in energy is also is shown. The shifts shown here are smaller than those reported in cryo-temperatures because these data were processed without background subtraction. The background level in a signal is known to change the absolute value of the FMs and dampen the expected shifts [106], however, background subtraction is very prone to producing misinterpretation of data and should be avoided whenever possible [28]. For this reason, the FM shifts reported here are only reported for raw data and only compared within the data sets collected for consistency.
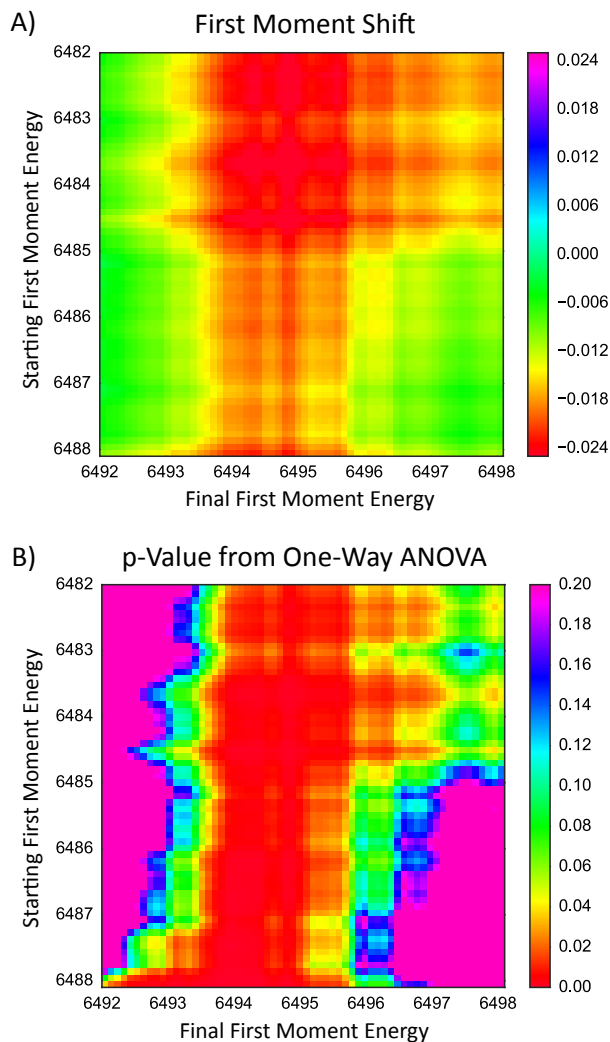
Figure 8.2. A map of A) oxidation and B) p-Value for the S2-S3 state transition are given. Each point on the map represents a different starting energy, y-axis, and ending energy, x-axis, in the calculation of the first moment.

The S2-S3 transition was also measured during the course of the two beamtimes sample data was collected to identify the capabilities of synchrotrons giving strong statistical evidence of the existence of a shift. A statistical power analysis of the data collected shows that at least 7x the data would be required to obtain 80% confidence that a type II error, or false negative, didn't occur given an observed

shift value of $\frac{1}{3}$ that of S1-S2, as has been reported for cryogenic temperature [18],. While obtaining this amount of data is itself prohibitive (representing a $\sim$6+ days of beamtime only recording S2 and S3 to find this shift), if the shift is actually closer to $\frac{1}{10}$ that of S1-S2 as our preliminary data suggests, then an order of magnitude more data would be required. We believe, therefore, that this shift is unlikely to be resolved without a significant undertaking at a synchrotron source. This analysis calls into question the significance of other reports which state FM shifts without testing for significance, particularly as smoothing and other data analysis procedures were employed which are know to affect interpretation [18, 28]. Determination of a lag phase in S2 to S3 is potentially inaccessible using this setup at synchrotron facilities, as is determining kinetic model differences as discussed in the previous chapter as these represent very small differences, $\sim\frac{1}{10} - \frac{1}{100}$ of a shift compared to S1 to S2. This requires differentiation between 2 models which are much smaller in value by a factor of 10 than that of the S2-S3 transition.

In more general terms, the power analysis for sample size requirements is expanded based on expected oxidation state changes for metalloproteins in general in Table 8.2. This was done assuming that the the S1-S2 transition represents a typical oxidation stat shift of one in four atoms and that the convolution of states and advancement is the same as found in the previous chapter. This would then mean that 0F-1F transition really only represents $\sim$60% S1-S2 which is $\frac{1}{4}$ the bulk oxidation such that the FM change is $\frac{3}{20}$ of that expected from a normal oxidation state change. The total exposure required, based on the spectrometer design and sample concentration, are presented as well. As a first order of approximation, the concentration and efficiency of the spectrometer are directly proportional to the exposure required to measure the sample. For our experiments here, the approximate Mn concentration is estimated to be 250 μM and the efficiency of the detector can compared using the crystal reflectivity and the solid angle covered by the analyzers. As an example case, a metalloprotein at 1mM concentration with two metals of the same atom would have 8x the concentration of the metal species but only experience 1/2 a bulk oxidation state shift when one

of the pair of metals is undergoing a oxidation state shift. This would mean that 8x less exposure is required that what is predicted for the 1/2 oxidation state shift. Note that the oxidation state shift is not directly proportional to the total exposure required and must be accounted for carefully.

Table 8.2.
Given our data collected from PSII we were able to calculate the necessary total sample exposure for dilute ($\sim$250 μM metal content) proteins using a three crystal spectrometer similar to that presented here. All Values are approximate and have an approximate error of 50%. Shots refer to either the pulse train used here (22 μs) or to a single pulse at an XFEL.

Exposure Required for Statistically Significant FM Shift				
ΔFM (0F-1F)	Bulk Oxidation State Change	Total X-ray Exposure	Sector 14 Shots	XFEL Shots
6.7	1	4×10^{14}	3×10^3	4×10^2
3.3	0.5	1×10^{15}	7×10^3	1×10^3
1.6	0.25	3×10^{15}	3×10^4	4×10^3
0.6	0.1	2×10^{16}	2×10^5	3×10^4
0.33	0.05	8×10^{16}	6×10^5	8×10^4
0.16	0.025	3×10^{17}	2×10^6	4×10^5
0.06	0.01	2×10^{18}	2×10^7	3×10^6

Also shown in Table 8.2 are the number of shots required using our setup at Sector 14 at the APS and the number of pulses required at an the Linac Coherent Light Source based on the typical photons per pulse (1×10^{12}). In addition to the number of pulses is the consideration of sample delivery. As our setup uses a single laser, we operate at 10 Hz for advancement, thus requiring over 0.3 s to measure each 3F state. With multiple lasers the sample can be delivered more quickly where the sample is illuminated in path to the interaction point. As some XFELs have this capability integrated, a sample measurement of the 3F state can be improved up to

36x faster, 120 Hz, than the setup used here. While this is not an inherent difference between the two facilities, it does show that in XFELs are more likely to be already equipped with the necessary tools to look at small changes in dilute samples. Some of these methods however may require more sample so a tradeoff must be considered.

In reference to the findings in Table 8.2 we suggest that for bulk oxidation state shifts smaller than 0.1, strong consideration should be taken to use an XFEL facility for the measurement. Additional information regarding XES at XFELs is considered in the next chapter.

8.4   Conclusions

Using the sample delivery system and the x-ray emission spectrometer outlined in Chapter 6 we were able to collect TRXES data using PSII at a synchrotron source. The data collected for the S1-S2 state transition shows a significant improvement in capability of the TRXES spectrometer over that used previously [106], yielding higher levels of significance with less data collected. This is consistent with the increase of 6 times the solid angle over that used previously. This larger capture of signal enables weak signals to be detected and recorded with statistical significance on a reliable basis. Additionally the sample delivery system was a significant improvement in terms of workload and manpower required at the beamline to maintain constant sample data collection and sample replacement.

The feasibility study for the S2 to S3 state transition resulted in the need for additional data, potentially beyond that which is reasonably obtainable using the current setup at a synchrotron source. We note,that this clarifies the limits of TRXES at beamlines given the exposure requirements in measuring bulk oxidative changes. Unless a specific need arises and sufficient beamtime allotments obtained, we suggest that the oxidation of 0.1 bulk oxidation be toward the limit of synchrotron work. Additionally, we note that isotopic substitution, such as that of D_2O, will result in comparing measurements at discrete time point. This results in the need to distin-

guish smaller differences between data sets which makes data collection unreasonable to obtain statistically significant differences.

Also as reported in this chapter is the need for a rigorous statistical analysis for analyzing shifts of weak signals. While the proper interpretation of weak signals is can be challenging, we emphasis that statistical methods should be used for validating statistically significant shifts between data sets. This methodology is particularly important in the context of metalloproteins where signals are almost guaranteed to be weak.

9. Sequential Ionization at X-ray Free Electron Lasers

9.1 Introduction

X-ray free electron lasers (XFELs) enable ultrafast measurements ($\sim$10-100 fs) using high energy x-ray pulses (10^{12} photons per pulse). While the ability to capture a series of snapshots during ultrafast electronic processes holds great promise, difficulties also await on the horizon for the interpretation of these signals. This includes taking snapshots of the metalloproteins to reconstruct ultrashort dynamics and catalytic changes. As is mentioned in Section 3.2.6, a multitude of nonlinear excitation processes now become accessible even when using routine XFEL parameters. These processes must be accounted for in order to properly interpret the spectroscopic signals obtained through XAS or XES at XFEL sources.

In this chapter we identify the regime where the classical spectrum, or single x-ray absorption and emission per atom, is no longer obtained owing to processes such as sequential ionization. In sequential ionization multiple single photon absorption events occur in a single atom during an XFEL pulse. We address the impact this process in 3d transition metals has on data collected using XES. Here we collected data on a representative system, Mn^{II} in solution, then created a rate equation model to describe the behavior. We address the impact of electron relaxation/no relaxation between absorption events, multiple sequential ionization events, the impact of shorter XFEL pulses, and how to get a first order estimate to the onset of sequential ionization. Even with the increase in the number of XFEL sources globally, beamtime is limited and few groups obtain multiple opportunities to conduct research. This places extreme importance on proper planning for TRXES experiments to be undertaken at these sources and emphasizes the importance of the simple estimation tool presented here for predicting the onset of sequential ionization given experimen-

tal parameters. While the research mentioned herein will impact the time resolved measurements of metalloproteins, a more broad impact is obtained with implications for all XES measurements at XFEL sources.

9.2 Mn as Model System

For work in this chapter we used Mn^{II} ions in a low Z (H, C, O) solution as a general model for XES of 3d transition metals. This model has important impact for the ongoing research conducted by XES at XFEL facilities for understanding the OEC in PSII [129]. As has been previously mentioned in this document, the OEC is very x-ray sensitive, causing damage to the electronic structure with only small doses [91,97,130]. Models for radiation damage at synchrotron sources have been based on the radicals formed and photoelectrons created due to the x-ray exposure [97]. The resulting damaged OEC results in a reduced form of Mn and structural rearrangement of atomic structure, extending Mn bond distances. This process unfolds on a time scale typical of that of normal chemical processes and can thus be outrun using fs pulses, such as those generated by XFELs [9–11,14]. As is described in brief detail in Section 3.2.6 however, XFEL pulses can also cause changes in the electronic structure as well.

9.2.1 XES Versus Crystallography at XFELs

For crystallography, it is currently believed that unaltered crystal structures can be obtained when using fs XFEL pulses. This is known as diffract before destroy and has been predicted since the year 2000 [131]. The idea is simple in that the effects of highly ionized electrons causing secondary ionizations and structural motion of atoms in response to this change in localized charge will not have time to react and create a Coulombic explosion. This suggests that the x-rays will probe the electron densities in the crystal structure with only minimal impact from delocalized photoelectrons and Auger electrons, leaving the larger atomic densities surrounding the atoms intact. It was later argued that even longer pulse durations will contribute

only to the background and not alter the crystallographic data [132]. These effects have been demonstrated through improved results in PSII geometry and better bond distances within the OEC [9–11, 33], though it is still unclear the complete effect sequential ionization has on interpretation of these results.

Spectroscopy, on the other hand, is quite different from crystallography and presents a more cautionary tale. While a study of the limits to the classical XES, or XES where each atom only absorbs no more than one photon, at XFEL sources has not previously been conducted in detail. Here XES has been used to identify new nonlinear effects obtainable at XFEL sources and to model their effects. The two main effects near the onset of x-ray intensity dependent spectral changes are sequential single photon absorption (SSPA) and electron cascade(see Section 3.2.6). Of these effects, SSPA is believe to be more largely responsible during short pulses while secondary ionization from energetic electrons is discussed in context.

9.3 Experimental Setup

9.3.1 Beamline Parameters

Research for this chapter was performed at the Coherent X-ray Imaging instrument [133] at the Linac Coherent Light Source (Menlo Park, USA) XFEL [110]. XFEL pulses were focused prior to the sample interaction region using a set of Kirkpatrick-Baez mirrors. The preset conditions using these mirrors typically results in a spot size of 1.3 μm (FWHM) which is the value used in calculations for this work, however, values could range up to 2.3 μm. An upstream gas monitor measured the pulse energy and was read out each shot. The number of photons was estimated from the pulse energy and assumed about 60% X-ray transmission efficiency through the X-ray optics to the downstream interaction point. Two beamtimes were used for the collection of this data (LJ49 and LL23) with the former consisting of data taken at 6.9keV with a pulse duration of 20 fs (Dataset 1) as well as 40 fs (Dataset 2). The latter beamtime was used to collect data were collected with 16 fs (Dataset 3) and 34 fs

(Dataset 4) x-ray pulses. The experiment was monitored using the software package OnDA [134]. During the course of the second beamtime (LL23) the micro-bunched electrons were recorded for each pulse using an X-band radio-frequency deflector [135] with background images taken every two hours for calibration.

9.3.2 Sample Preparation and Delivery

The Mn^{II} sample was prepared by dissolving $MnCl_2 \bullet (H_2O)_4$, obtained from Sigma Aldrich, in a solution of water (Dataset 1) or ethanol (Datasets 2-4) to a concentration of 1 Molar. During the beamtime both gas-dynamic virtual nozzles [136] and double flow focusing nozzles [137] were used to deliver the solution in a $\sim$5 μm diameter jet into the interaction region. The two jetting techniques only differ in the medium around the sample that maintains a constant flow of solution. Flow rates of 5-40 μl/min were used with a 40 μm diameter port in the nozzle.

Table 9.1.
The different data sets and basic parameters for each is shown.

	Data Set 1	Data Set 2	Data Set 3	Data Set 4
X-ray Photon Energy	6.9keV	6.9keV	8.7keV	8.7keV
X-ray Pulse duration	20fs	40fs	16fs	34fs
Sample Solution	Ethanol	Water	Ethanol	Ethanol

The diameter of the jet estimated to have fluctuated between 5-20 μm in diameter during data collection. The constant flow of the jet ensured fresh sample was measured during the 120 Hz operation. The liquid jet was collected below in an aluminum catcher directly below the interaction region. Powder Mn oxides were also measured using X-ray pulses. In this case, the spot size was adjusted to 100 μm FWHM and measured over a few spots during the second beamtime (LL23). This was done by

inserting a sample holder at the interaction region with the oxides sealed in Kapton tape. No spectral changes were found between X-ray exposures on the same sample.

9.3.3 X-ray Emission Detection

A von Hamos X-ray emission spectrometer [121] was used to collect both the Mn $K\beta_{1,3}$ and $K\beta'$ emission lines. Data collected at 6.9 keV and 8.7 keV were collected using the CSPAD [138] and the ePix [139] detectors respectively. Both of these detectors have gaps between modules where data could not be collected. This occurred between 6499.8-6500.3 eV emission energies for data collected with 20 fs pulses at 6.9 keV, 6490.1-6490.6 eV for data collected with 40 fs pulses at 6.9 keV and between 6483-6484 eV for all data sets obtained using 8.7 keV incident energy. For dead or missing pixels, values were linearly interpolated by two nearest data points in the final emission spectrum.

As the setup required a liquid sample catcher under the liquid jet, the spectrometer was tilted at ~15 degrees from the vertical so as to enable the recording of the emission signal. In beamtime two, LL23, $K\beta'$ was also measured unlike that of previous reports [121] due to a smaller catcher reducing geometric constraints.

Spectra were then recorded at an angle across the detection surface. These were analyzed using a bilinear interpolation [140]. This interpolation method was used to recreate the spectra by taking evenly spaced steps along the emission line as recorded by the detector and interpolating a new set of points based on proximity to the four nearest neighbors. The spectra were then calibrated based on the angles reflected from the spectrometer as a function of distance and by matching the $MnCl_2$ sample collected at a low X-ray beam intensity to that obtained at a synchrotron source.

9.4 Rate Equation Model

A rate equation model was developed to follow the excited states of atoms based on the number of 1s holes created and photons absorbed. Shown in Figure 9.1 is the

model used to understand the behavior of SSPA. Symbolically, the rate equation with j, the number of current 1s holes, and k, the total number of ionization events, can be written as

$$\frac{dS_k^j}{dt} = A^{j-1}S_{k-1}^{j-1} + D_k^{j+1}S_k^{j+1} - A^jS_k^j + D_k^jS_k^j \tag{9.1}$$

Where A is the absorption rate and D is the decay rate of the indicated state. The the absorption rate can be written as

$$A^j = \Phi\sigma_{1s}^j \tag{9.2}$$

Where Φ is the photon flux density (photons/area/time) and σ_{1s}^j is the energy dependent 1s orbital photoelectric cross section given j holes. In this figure photoabsorption is represented by arrows indicating an advancement to a vertically higher level (maximum of two 1s holes). Relaxation of the electronic system to fill a 1s hole is a vertical drop to the level below.

The 1s cross section and the decay rates were found using the program package XATOM [141–143]. The flux density was calculated by assuming an uncorrelated
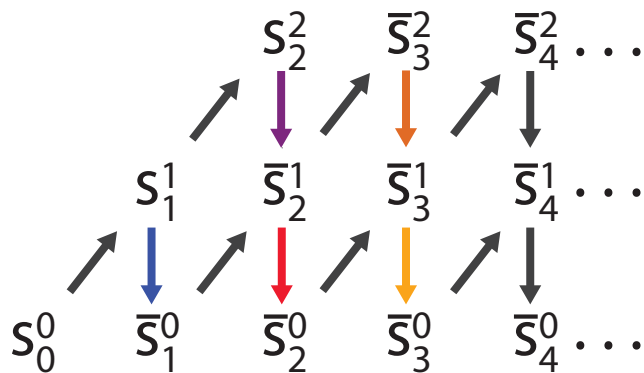
Figure 9.1. The rate equation model with each state, S, labeled by the number of 1s holes (super script) and total 1s absorption events (subscript) and the bar above indicates that there are multiple electronic configurations in this state. Arrows going up indicate 1s absorption and arrows down are electronic relaxation. Colors are referenced to differentiate emission from different electronic configurations where blue represents classical single photon absorption/emission.

bivariate Gaussian profile which was evaluated stepwise in 30 sections ranging from 0 to three times the FWHM. Each solution from the stepwise approximation was normalized by the integral percentage of x-rays in that region and summed. The system of equations generated for the model shown in Figure 9.1 were evaluated using Maple 2017. This fundamental model also used the following assumptions: 1) the x-ray intensity didn't change with sample thickness ($<$10% absorption for all samples used here), 2) absorption events caused by orbitals other than the 1s were ignored ($\sim$10% contribution in our experiments), and 3) near identical values for decay rates were found using XATOM for states representing multiple electronic configurations, which led to the use of a single decay value for each state shown in Figure 4.

The average number of ionization events that occur to each atom after a 1s hole is formed was calculated using time constants and decay rates in XATOM for the S_1^0 state. Essentially, we assumed in this calculation that all holes in the L-shell were filled by M-shell electrons immediately after 1s ionization. This was found to be a good approximation for our data considering the short time constant of these states, 0.2-2 fs. This corresponds to Figure 3.6B-III.

9.5 Results

9.5.1 X-ray Emission Spectra of Mn^{II}

In order to understand the role of sequential ionization in XES at XFEL facilities a series of four data sets were collected under the series of conditions as shown in Table 9.1. These data sets were recorded using the Mn^{II} metal ion in a low element environment. X-ray emission spectra were captured from each of the data sets using a range of pulse intensities as shown in Figure 9.2. Here, the presence of an x-ray pulse intensity dependence of the emission spectra is clearly visible. It is also clear to see that the shifts are not equal in each data set, suggesting an additional dependence on photon energy or pulse duration.

To understand the series of observed spectral shifts in each of the data sets, a theoretical model was developed. This model is based on rate equations [65, 144, 145] and a schematic is shown in Figure 9.1. The population of Mn centers that have j holes in the 1s after a series of k ionization events, S_k^j, throughout a single pulse is found by solving the resulting differential equations. In this model, the initial population is entirely in the ground state S_0^0 as a Mn^{II} with a filled 1s orbital. As
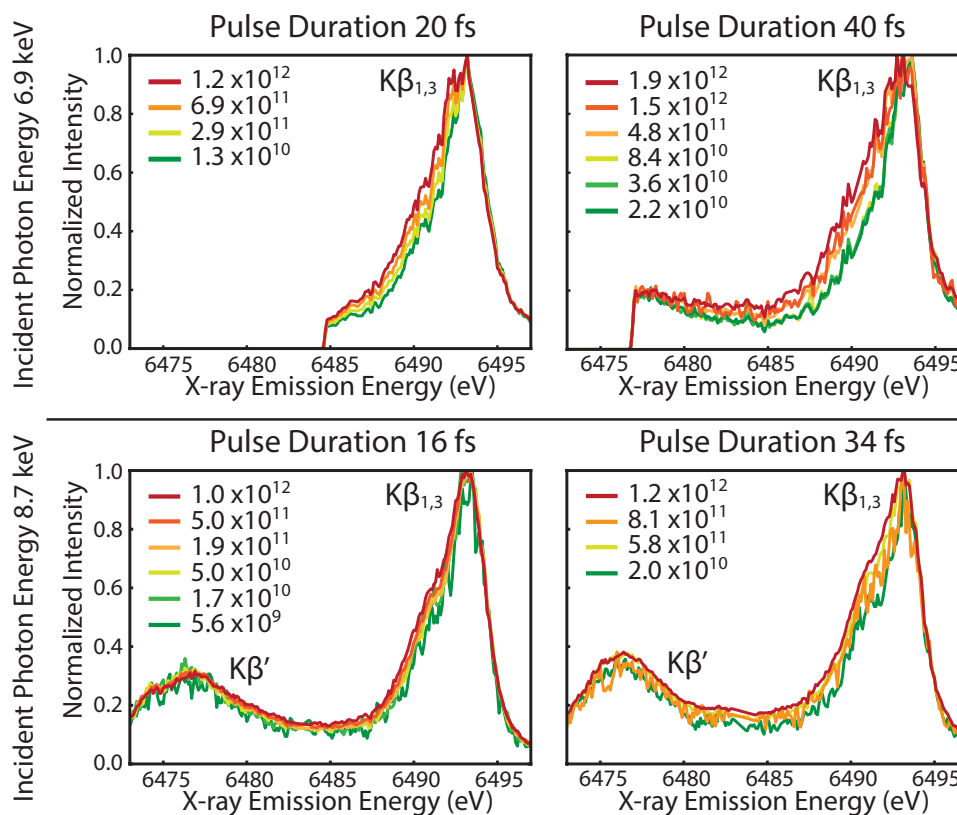
Figure 9.2. $K\beta$ emission spectra of Mn^{II} using a range of x-ray per pulse, colored green to red for increasing values. Data sets 1-4 are shown with the top two data sets representing beamtime one using 6.9 keV and the bottom beamtime two with 8.7 keV. The $K\beta$' region was only recorded during beamtime two (see methods). As can be seen visually, broadening of the low energy side of the $K\beta_{1,3}$ line is present for higher pulse intensities is visible.

the atom undergoes photoabsorption events, the population advances through the different states, as described in Section 9.4.

The model is only dependent on a few experimental factors, namely the 1s orbital cross section (dependent on incident photon energy), the photon flux density (both of which make the absorption rate), and the pulse duration. As such, a parameter, α, is used to capture all of these characteristics as an approximation to the absorption rate multiplied by time. This parameter can be expressed as,

$$\alpha = \sigma_{1s}^0 \left(\frac{0.5(PhotonsPerPulse)}{Area} \right) \approx A^j t \tag{9.3}$$

where σ_{1s} is the photoelectric cross section of the 1s orbital, half the photons per pulse is the number of photons in the FWHM of the x-ray profile and the Area is the area of the x-ray spot size. This parameter is only an approximation since it does not account for the photon flux density changes within the Gaussian profile.

One physical way to interpret this parameter is to realize that the fraction population of atoms that have absorbed a photon, P_a, is

$$P_a \approx 1 - e^{\alpha} \tag{9.4}$$

which can be further simplified as simply α when α is small by taking the first term of a Taylor series expansion. Thus, this parameter is related to the number of atoms absorbing photons. In any case, the parameter is simply used herein as a method for comparing different data sets that were collected using different incident photon energies, beam intensities, and pulse durations. As α captures much of the dependence of these effects on the data, it provides a clean method for comparison. Here we show the different values for this parameter for our data and previous work, see Table 9.2.

In Figure 9.3 the fraction of the recorded Kβ emission spectra that are emitted from the different ionization states is shown. Here we only consider up to three sequential ionization events, after which Kβ emission is largely inaccessible due to an empty 3p shell. This plot gives a visual representation of the different proportions of the recorded signal that arises from the classical singly 1s ionized state and those

that have undergone SSPA. In this figure the color scheme matches that of Figure 9.1. From this data we estimate the percent of classical fluorescence, F$_{classical}$ obtained in the linear region of low α as,

$$F_{classical} = 100\% - 34\%\alpha, \text{ where } \alpha \leq 0.25 \tag{9.5}$$

This estimation tool allows for a simple calculation of the expected effect SSPA will have on data given simple experimental parameters. While the behavior of other spectroscopic techniques may lead to slightly different effects, we note that this tool may be translatable to some extent to any XFEL based spectroscopic experiment.

In Figure 9.2 we used a first moment analysis as described in Section 3.2.5. The emission energy range used in the first moment analysis was 6485-6495 eV with the spectra being in 0.1 eV bins. Here we used the change in the first moment as the indicator for detectable shifts in the spectra. As each data set contains a low dose emission spectra, or classical spectrum, this was taken to be the initial point for

Table 9.2.
The different measurements and corresponding alpha for each.

	Pulse Duration	Photon Energy	α
Present Work	20 fs	6.9 keV	0.015 - 1.4
	40 fs	6.9 keV	0.026 - 2.2
	16 fs	8.7 keV	0.037 - 0.7
	34 fs	8.7 keV	0.013 - 0.77
Low Dose [88]	50 fs	7 keV	0.12
	100 fs	7 keV	0.037
	50 fs	9.5 keV	0.055
	100 fs	9.5 keV	0.017
Stimulated Emission [68]	10 fs	6.6 keV	2.4-18
	30 fs	6.6 keV	2.4-18

all shifts shown in Figure 9.4. These changes indicate the strength of the spectral shift, which in the single absorption picture is a change in localized spin density or oxidation state. The prediction of FM spectral shifts based on SSPA is accounted for based on the number of holes formed in the m-shell after relaxation, each of which is approximated to give a shift equivalent to that of one oxidation state. This prediction generates the models shown in Figure 9.4.

The near identical collapse of the rate equation predictions in Figure 9.4 as a result of α capturing . There are, however, more variations in the data than is observed in the model. These deviations are likely the result of the electron cascade, initiated by the initial photoelectron emission and Auger electrons. If this is true then the longer pulse durations are likely to have a larger impact as this would represent more time
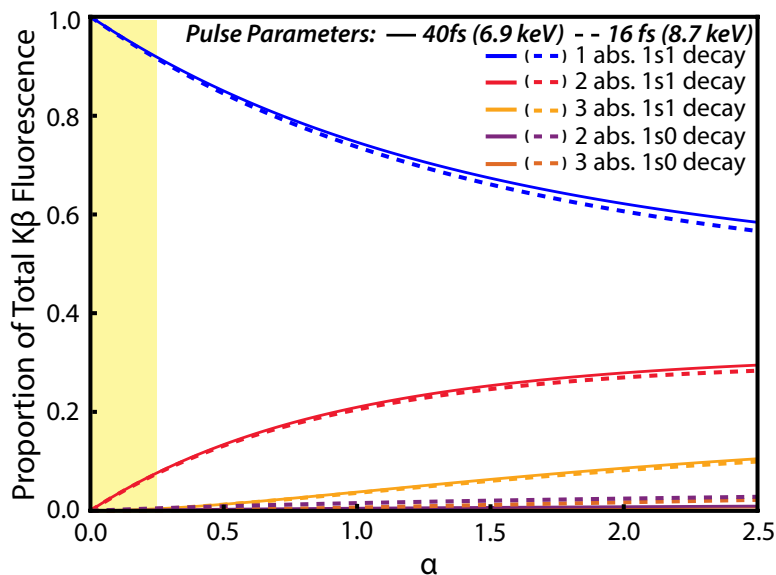
Figure 9.3. The contributions to the total Kβ fluorescence based on decay from five different states: emission from an atom with a single core hole emission after 1, 2 and 3 X-ray absorption events and a double core hole after 2 and 3 X-ray absorption events with colors matching those in Figure 9.1. The solid and dotted line representing 40 fs at 6.9 keV and 16 fs at 8.7 keV respectively. An approximately linear regime is highlighted in yellow.

for electron-electron interactions causing additional ionization events. In addition, the parameter α compensates for the energy dependence of the 1s cross section of the absorbing atom not the medium in which the ion resides. For lower energies the percent of absorption by the solvent is actually increased and could represent an increase in the number of free electrons initiating the electron cascade.

As the quality of crystallography is strongly dependent on the x-ray pulse duration, we show the dependence of pulse duration on XES for comparison. The results, shown in Figure 9.5, shows the fractional contribution to the recorded Kβ emission spectra.
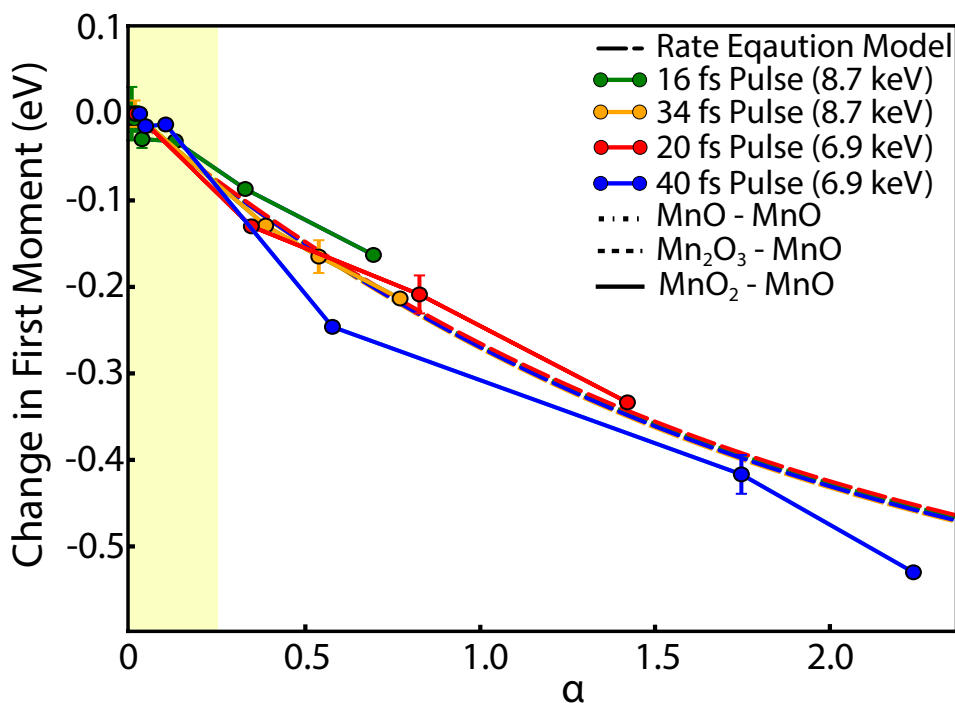
Figure 9.4. The change in first moment is shown for the four data sets. Predictions from the rate equation model for the data are represented by dashed lines with colors corresponding to the data. All rate equation predictions overlap with nearly identical predictions based on the parameter α. The highlighted region represents a nearly linear dependence of the change in first moment to α. The horizontal bars indicate the difference between the FM values of Mn^{II}, Mn^{III} and Mn^{IV} oxides from the reference Mn^{II} oxide to indicate typical FM shifts based on oxidation state. Data were randomly broken into five groups to get a SEM for the first moments.
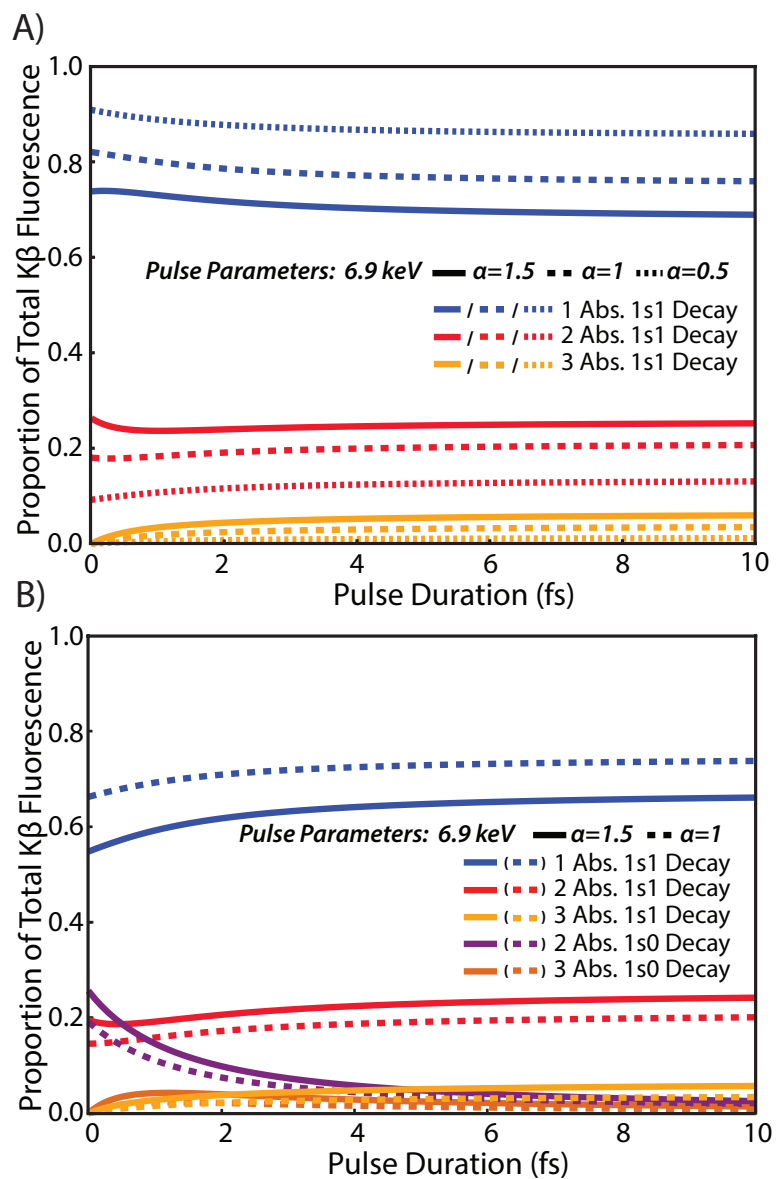
Figure 9.5. Proportions of fluorescence is shown based on current and total number of 1s holes created in the emitting atom. (A) The ratio of fluorescence from different single 1s holes (separated by color) given for different values of α (line style) and pulse duration, normalized by total single 1s hole emission (representing recorded Kβ signal sources). (B) Same as (A) except dual core hole fluorescence is shown and used in normalization (representing total Kβ fluorescent yields).

Similar to Figure 9.3, these data are also color coded based on the decay pathways presented visually in Figure 9.1. This figure illustrates the effect of durations similar in length to the time constant of the S_1^1 state, or even shorter. From this plot it is clear that the percent of emission from the single photon absorption state is largely unaffected. In Figure 9.5A, the fractional contributions to the recorded signal ignore dual core hole spectra, as it is likely to lie outside the typical XES range. Figure 9.5B does include dual core hole spectra, or hypersatellites, to show the total Kβ emission source. While this figure indicates that classical XES are not obtainable by moving to shorter pulses, it does hint that hypersatellite spectra may be a better spectroscopic tool if XFEL pulses continue to become shorter and more intense.

9.6   Discussion

Sequential ionization involves a single x-ray absorption event creating a core-hole and possibly relaxing before another x-ray is absorbed by the same atom. As shown in Figure 9.2 the Mn Kβ emission lines are affected by this process. The shifts calculated based on the rate equation model were well fit to the data and good predictors for emission line shifts, Figure 9.4. It is also clear that data sets with lower incident x-ray energy or longer pulse duration deviate more from the model. This effect is attributed to the increased number of electrons freed from the host atom and causing additional ionization events through electron-electron interactions. With lower energy incident photons but the same value of α, an increase in the number of low Z elements that cause ionization events and longer pulse durations will allow for more interactions.

From the rate equation model, spectral line shifts were calculated for Mn$^{\text{II}}$ specifically, however, other high spin systems will likely exhibit similar shifts depending on their FM dependence on oxidation. An estimation of the expected shift for transition metals was generated using the highlighted region in Figure 9.4. From this linear

regime, the dependence on the first moment shift as a function of α can be written as

$$FM_{shift} = -0.3\alpha, \text{ when } \alpha \geq 0.25 \qquad (9.6)$$

This simple calculation is a first order estimate to the FM shift expected which, when compared to the expected shift of the sample, can be used to estimate what value of α is tolerable.

Knowing this level of tolerance is quite important for systems, such as photosystem II, where small first moment shifts of $\sim$0.02eV have been reported for the S2 to S3 state transition [18]. For such a system, the threshold should be placed at an α that corresponds to a shift much less than 0.02 eV, especially when considering that this model doesn't account for effects expected from the electron cascade. As an example, one group reported their findings did not contradict a previous report of no detectable shift in the X-ray emission spectra of $MnCl_2$. In their report, an uncertainty of 0.05 eV was given for their comparison between XFEL and the unshifted synchrotron data [121] whereas the predicted shift using the rate equation model is of $\sim$0.036 eV. While this may seem like a small shift, data for PSII was also recorded using these same conditions leading to some uncertainty in the quality of the PSII data.

With the emphasis in creating shorter pulses for improved crystallographic results, XFEL sources have been trying to push the limits toward sub fs pulses. As these pulse durations are reached there may be some advantages gained in avoiding electron cascade effects, however, the predictions in Figure 9.5 show that SSPA cannot be overcome in this manner. This can be understood simply with the physical model. When a very short intense pulse causes multiple ionizations before the atom can relax, it will create a dual core hole. Since the emission from atoms in the 1s0 state are likely to be significantly shifted relative to single 1s hole spectra [146], they are not expected to overlap and contribute to shifts in the final FM. On the other hand, when the second 1s hole is filled, the emission process will be in the presence of several holes but it will still likely have overlapping spectral lines . The second decay will have a higher probability of occurring in the presence of another low lying hole in the n=2

shell given the short amount of time after dual core hole decay and single core hole decay. This is in contrast to longer pulses used here where the holes are in the n=3 level and are expected to lead to a different FM shift that that shown in Figure 3.6. Nevertheless, spectral line shifts from sequential ionization cannot be outrun and the race toward shorter X-ray pulses will not overcome these effects.

As two sources of x-ray induced spectral changes to XES are presented, we find it prudent to identify the best ways in which these sources can be mitigated. As sequential ionization is dependent on α, the choices are simply to reduce the number of photons, increasing the x-ray spot size or use a higher excitation energy. Out of these methods, only increasing the spot size will reduce spectral shifts without a corresponding loss in signal intensity. When changing the spot size is not feasible, such as in some cases of simultaneous crystallography and diffraction, then higher energy incident x-rays should be preferred. This will reduce the SSPA contribution to the emission spectra and also reduce the electron cascade effects.

As shorter pulses will also lead to fewer electron interactions this is also believed to be a valid method for reducing electron cascade effects, however, shorter pulses will likely cause an increase in stimulated emission. While not measured in our experiment, stimulated emission has been reported as a possible methodology to increase emission signals. While true, the signals obtained through this processes have in some cases shown to be shifted relative to the classical spectral data [68]. While these shifts were unexplained in that report, it is evident from a rate equation standpoint that increasing the rate of decay by providing an additional relaxation pathway through stimulated emission will only fill the 1s orbital faster and increase the chance of sequential absorption. This leads to an increase of emission from highly ionized states.

As mentioned previously, the relaxation of an atom with a dual core hole will lead to hypersatellite emission lines. As these lines are not likely to overlap with single core hole emission spectra, this may be a useful technique in consistently capturing unaltered emission data. This would be done by exposing a sample to an ultrashort

pulse that causes dual core hole ionization and ends abruptly before the holes can be filled in an emission process. Once the X-rays are past the sample, emission can then be recorded. As the first core hole is filled, a hypersatellite is emitted. As the second hole is filled, a single core hole emission spectra is emitted in the presence of other holes. If the two spectra don't overlap, then the first emission will result in a clean hypersatellite spectra. There are of course complications and limitations to this approach including limited signal from the subpopulation of the sample that actually reached the dual core hole state. Additionally, the physical picture presented is over idealized since the intense x-ray pulse will more than likely cause additional holes in orbitals other than the 1s generating altered hypersatellite spectra as well. In either case some work has been done with hypersatellites experimentally [71], but clearly more research will be required experimentally and theoretically before hypersatellites can be used as a viable spectroscopic technique.

9.7   Conclusions

With the increasing number of XFEL sources becoming available, the user base and the number of time resolved XES measurements will also increase. As these opportunities become available, the need for guiding principles for proper experimental conditions will increase. Additionally, XFEL sources are pushing time scales that have not been previously achievable with intense hard x-ray pulses. As we enter this new regime, which is pushed forward by crystallography, care must be taken to not ignore the minimal impact shorter pulses will have on preventing sequential ionization shifts in x-ray emission spectra.

In this chapter Mn^{II} $K\beta$ emission was recorded in four data sets to identify any dependence of x-ray induced shifts in the emission spectra. A rate equation model was created to calculate the percentage of the recorded emission spectra is from single photon absorption. Those predictions address the need for a simple method for estimating x-ray induced shifts resulting from sequential ionization. This will

enable uses to properly prepare for and effectively use their time at these important facilities. Additionally, the inability to escape sequential ionization using shorter pulse durations was also discussed.

10. Conclusions

Within this dissertation a range of topics were discussed and questions answered centering around time resolved x-ray spectroscopy of metalloproteins. Within this text, new instrumentation is presented, model compounds were measured, promising capabilities using TRXAS was demonstrated, potential and limitations of TRXES at synchrotrons were evaluated and the potential an pitfalls of XES at XFELs were addressed. For clarity, the discussion of each is addressed in turn, briefly describing the major points of the chapters herein.

A new spectrometer design was presented as a cost effective solution that can easily integrate into almost any beamline using a routine alinement procedure. The fabrication protocol for segmented, or diced, von Hamos optics for almost any radius of curvature or material is presented. A three crystal spectrometer design was developed at a cost of ~\$2,000 USD which is about $\frac{1}{150}$ the cost and nearly half the efficiency of a 16 analyzer spectrometer.

An automatic sample delivery system was developed and proven capable for delivering sample to a tight interaction point where both laser pump and x-ray probe occurs. The liquid sample is automatically replaced using a stepper motor and Arduino motor controller to run at 10 Hz which can likely be pushed to higher speeds with small adjustments as described. This system greatly reduced to manual effort required in sample preparation and delivery at the beamline for time resolved studies and has potential impact for applications with laboratory sources or with other techniques altogether.

Biomimetic compounds were measured using a prototype spectrometer with only one crystal. Sufficient data was recorded in only 10 seconds, yet still being able to resolve a small (0.07 eV) shift in the first moment. Using these compounds we show that beyond changes in oxidation state of a metal, XES is sensitive to the changes

in the nominal spin density which is affected by the ligands, which in this case was a deprotonation event for an hydroxyl group. This change was then compared with changes found in photosystem II in the S2-S3 state transition. While a very similar change was found in the S2-S3 transition, if Mn centered oxidation occurs during this same transition then the shift expected in the emission spectra from oxidation must be masked by other changes that increase the spin density of the Mn atoms.

Time resolved x-ray absorption spectra were taken of photosystem II for all transition states. Here we achieved a high advancement of photosystem II, ∼83%, and show a similar S3-S0 contribution to absorption changes in the 3F as that of preflashed data. We also compare the different S-state models with those reported earlier. In particular, we compare the S3-S0 transition of our data with that of the only other group to preform these measurements [1, 47]. We address the possibilities of other models not previously considered that match the data better than the model suggested, though more data would be required before conclusive statements could be made. The setup developed, along with the sample delivery system, prove to be an reliable method for conducting time resolved measurements of metalloproteins without the need for a specialized beamline.

Given the development of a new spectrometer and sample delivery system, we test the capabilities of these systems in TRXES. This proved to be a more complex endeavor as metal concentrations in metalloproteins is often quite low and XES is also a low signal measurement. Despite this challenge, we were able to collect a small data set from which we were able to identify a statistically significant S1-S2 transition at room temperature. While this had be achieved previously, it took much more data than what was used here. Additionally, we show the data requirements to find statistically significant shifts of other magnitudes and give the guidance of ∼0.1 bulk oxidation state shift being toward the limit of synchrotron capability. Alternative methods for increasing this capability are discussed including using an XFEL source.

The combination of intense and ultrashort x-ray pulses at XFEL facilities provides the capability to measure TRXES of fundamental processes that could otherwise not

be seen. For metalloproteins this both means a needed increase in signal intensity and the capability to capture short lived intermediate states. Despite these advantages, caution still must be taken so as to avoid misinterpretation of spectroscopic results. Once an atom is exposed to an XFEL pulse, sequential single photon ionization may occur, thus resulting in a different spectra than that expected for single photon absorption spectra. As there was no simple method for predicting this change in regime, a general tool was developed in Chapter 9 to estimate the onset of such changes and their impact to x-ray emission spectra. This metric is a useful tool to estimate the percent of the emission generated from atoms that have only absorbed one x-ray or multiple x-rays during a single pulse and the expected first moment changes that can cause. Along with this estimate were general conclusions about how to limit damage when performing experiments at these facilities. The analysis of XFEL data also lead to the discovery of continued damage with shorter x-ray pulses of the same intensity. While this is considered to be a viable method to escape most crystallographic damage, XES is clearly dependent on the electronic configuration which can become highly ionized in a single pulse. This result is believed to be important as XFEL facilities continue to move forward in development since the typical notion has been to try and create sub fs pulses. While this does have the potential in overcoming electron cascade effects by shortening the time for electron-electron interactions, it doesn't overcome spectral changes from sequential ionization.

Overall, the future of time resolved x-ray spectroscopy for metalloprotiens is bright. New tools for measurements have been developed that can enable these measurements to be more routine at synchrotron sources using simple cost effective designs. XFEL sources are also on the rise with several coming online across the globe enabling faster measurements to be made on even more dilute samples. These facilities, when used with the proper caution, will enlarge our understanding of the role metalloproteins play in maintaining oxygen in our atmosphere, providing our bodies with energy and enabling the basic functions of life.

REFERENCES

REFERENCES

[1] M. Haumann. Photosynthetic O2 Formation Tracked by Time-Resolved X-ray Experiments. *Science*, 310(5750):1019–1021, 2005.

[2] Anastasios Melis. Photosynthesis-to-fuels: from sunlight to hydrogen, isoprene, and botryococcene production. *Energy & Environmental Science*, 5(2):5531, 2012.

[3] Yasuhiro Tachibana, Lionel Vayssieres, and James R Durrant. Artificial photosynthesis for solar water-splitting. *Nature Photonics*, 6(8):511–518, 2012.

[4] Ralph L House, Neyde Yukie Murakami Iha, Rodolfo L Coppo, Leila Alibabaei, Benjamin D Sherman, Peng Kang, M Kyle Brennaman, Paul G Hoertz, and Thomas J Meyer. Artificial photosynthesis: Where are we now? Where can we go? *Journal of Photochemistry and Photobiology C: Photochemistry Reviews*, 25:32–45, 2015.

[5] Daniel J Little, I I I Milton R Smith, and Thomas W Hamann. Electrolysis of liquid ammonia for hydrogen generation. *Energy Environmental Science*, 8(9):2775–2781, 2015.

[6] U.S. Energy Information Administration. International Energy Outlook, 2016.

[7] Yuri Munekage, Mihoko Hashimoto, Chikahiro Miyake, Ken-ichi Tomizawa, Tsuyoshi Endo, Masao Tasaka, and Toshiharu Shikanai. Cyclic electron flow around photosystem I is essential for photosynthesis. *Nature*, 429(6991):579–582, 2004.

[8] Bessel Kok, Bliss Forbush, and Marion McGloin. Cooperation of Charges in Photosynthetic O2 Evolution -I. A Linear Four Step Mechanism. *Photochemistry and Photobiology*, 11(6):457–475, 1970.

[9] Michihiro Suga, Fusamichi Akita, Kunio Hirata, Go Ueno, Hironori Murakami, Yoshiki Nakajima, Tetsuya Shimizu, Keitaro Yamashita, Masaki Yamamoto, Hideo Ago, and Jian-Ren Shen. Native structure of photosystem II at 1.95 Å resolution viewed by femtosecond X-ray pulses. *Nature*, 517(7532):99–103, 2015.

[10] Iris D Young, Mohamed Ibrahim, Ruchira Chatterjee, Sheraz Gul, Franklin D Fuller, Sergey Koroidov, Aaron S Brewster, Rosalie Tran, Roberto Alonso-Mori, Thomas Kroll, Tara Michels-Clark, Hartawan Laksmono, Raymond G Sierra, Claudiu A Stan, Rana Hussein, Miao Zhang, Lacey Douthit, Markus Kubin, Casper de Lichtenberg, Long Vo Pham, Håkan Nilsson, Mun Hon Cheah, Dmitriy Shevela, Claudio Saracini, Mackenzie A Bean, Ina Seuffert, Dimosthenis Sokaras, Tsu-Chien Weng, Ernest Pastor, Clemens Weninger, Thomas Fransson, Louise Lassalle, Philipp Bräuer, Pierre Aller, Peter T Docker, Babak

Andi, Allen M Orville, James M Glownia, Silke Nelson, Marcin Sikorski, Diling Zhu, Mark S Hunter, Thomas J Lane, Andy Aquila, Jason E Koglin, Joseph Robinson, Mengning Liang, Sébastien Boutet, Artem Y Lyubimov, Monarin Uervirojnangkoorn, Nigel W Moriarty, Dorothee Liebschner, Pavel V Afonine, David G Waterman, Gwyndaf Evans, Philippe Wernet, Holger Dobbek, William I Weis, Axel T Brunger, Petrus H Zwart, Paul D Adams, Athina Zouni, Johannes Messinger, Uwe Bergmann, Nicholas K Sauter, Jan Kern, Vittal K Yachandra, and Junko Yano. Structure of photosystem II and substrate binding at room temperature. *Nature*, 540:1–22, 2016.

[11] Michihiro Suga, Fusamichi Akita, Michihiro Sugahara, Minoru Kubo, Yoshiki Nakajima, Takanori Nakane, Keitaro Yamashita, Yasufumi Umena, Makoto Nakabayashi, Takahiro Yamane, Takamitsu Nakano, Mamoru Suzuki, Tetsuya Masuda, Shigeyuki Inoue, Tetsunari Kimura, Takashi Nomura, Shinichiro Yonekura, Long-Jiang Yu, Tomohiro Sakamoto, Taiki Motomura, Jing-Hua Chen, Yuki Kato, Takumi Noguchi, Kensuke Tono, Yasumasa Joti, Takashi Kameshima, Takaki Hatsui, Eriko Nango, Rie Tanaka, Hisashi Naitow, Yoshinori Matsuura, Ayumi Yamashita, Masaki Yamamoto, Osamu Nureki, Makina Yabashi, Tetsuya Ishikawa, So Iwata, and Jian-Ren Shen. Light-induced structural changes and the site of O=O bond formation in PSII caught by XFEL. *Nature*, 543(7643):131–135, 2017.

[12] Katherine M Davis, Brendan T Sullivan, Mark Palenik, Lifen Yan, Vatsal Purohit, Gregory Robison, Irina Kosheleva, Robert W Henning, Gerald T Seidler, and Yulia Pushkar. Rapid Evolution of the Photosystem II Electronic Structure during Water Splitting. *ArXive*, 2015.

[13] Jan Kern, Roberto Alonso-Mori, Rosalie Tran, Johan Hattne, Richard J Gildea, Nathaniel Echols, Carina Glöckner, Julia Hellmich, Hartawan Laksmono, Raymond G Sierra, Benedikt Lassalle-Kaiser, Sergey Koroidov, Alyssa Lampe, Guangye Han, Sheraz Gul, Dörte Difiore, Despina Milathianaki, Alan R Fry, Alan Miahnahri, Donald W Schafer, Marc Messerschmidt, M Marvin Seibert, Jason E Koglin, Dimosthenis Sokaras, Tsu-Chien Weng, Jonas Sellberg, Matthew J Latimer, Ralf W Grosse-Kunstleve, Petrus H Zwart, William E White, Pieter Glatzel, Paul D Adams, Michael J Bogan, Garth J Williams, Sébastien Boutet, Johannes Messinger, Athina Zouni, Nicholas K Sauter, Vittal K Yachandra, Uwe Bergmann, and Junko Yano. Simultaneous femtosecond X-ray spectroscopy and diffraction of photosystem II at room temperature. *Science*, 340(6131):491–5, 2013.

[14] Christopher Kupitz, Shibom Basu, Ingo Grotjohann, Raimund Fromme, Nadia A. Zatsepin, Kimberly N. Rendek, Mark S. Hunter, Robert L. Shoeman, Thomas A. White, Dingjie Wang, Daniel James, Jay-How Yang, Danielle E. Cobb, Brenda Reeder, Raymond G. Sierra, Haiguang Liu, Anton Barty, Andrew L. Aquila, Daniel Deponte, Richard A. Kirian, Sadia Bari, Jesse J. Bergkamp, Kenneth R. Beyerlein, Michael J. Bogan, Carl Caleman, Tzu-Chiao Chao, Chelsie E. Conrad, Katherine M. Davis, Holger Fleckenstein, Lorenzo Galli, Stefan P. Hau-Riege, Stephan Kassemeyer, Hartawan Laksmono, Mengning Liang, Lukas Lomb, Stefano Marchesini, Andrew V. Martin, Marc Messerschmidt, Despina Milathianaki, Karol Nass, Alexandra Ros, Shatabdi Roy-Chowdhury, Kevin Schmidt, Marvin Seibert, Jan Steinbrener, Francesco Stellato, Lifen Yan, Chunhong Yoon, Thomas a. Moore, Ana L. Moore, Yulia Pushkar, Garth J. Williams, Sébastien Boutet, R. Bruce Doak, Uwe Weierstall,

Matthias Frank, Henry N. Chapman, John C. H. Spence, and Petra Fromme. Serial time-resolved crystallography of photosystem II using a femtosecond X-ray laser. *Nature*, 513(7517):261–265, jul 2014.

[15] Stenbjörn Styring and A William Rutherford. Deactivation kinetics and temperature dependence of the S-state transitions in the oxygen-evolving system of Photosystem II measured by EPR spectroscopy. *BBA - Bioenergetics*, 933(2):378–387, 1988.

[16] Guangye Han, Fikret Mamedov, and Stenbjörn Styring. Misses during water oxidation in photosystem II are S state-dependent. *Journal of Biological Chemistry*, 287(16):13422–13429, 2012.

[17] U Bergmann, M M Grush, C R Horne, P DeMarois, J E Penner-Hahn, C F Yocum, D W Wright, C E Dubé, W H Armstrong, G Christou, H J Eppley, and S P Cramer. Characterization of the Mn Oxidation States in Photosystem II by K X-ray Fluorescence Spectroscopy. *Journal of Physical Chemistry B*, 102(42):8350–8352, 1998.

[18] Johannes Messinger, John H Robblee, Uwe Bergmann, Carmen Fernandez, Pieter Glatzel, Hendrik Visser, Roehl M Cinco, Karen L McFarlane, Emanuele Bellacchio, Shelly a Pizarro, Stephen P Cramer, Kenneth Sauer, Melvin P Klein, and Vittal K Yachandra. Absence of Mn-Centered Oxidation in the S 2 S 3 Transition: Implications for the Mechanism of Photosynthetic Water Oxidation. *Journal of the American Chemical Society*, 123:7804–7820, 2001.

[19] Yasufumi Umena, Keisuke Kawakami, Jian-Ren Shen, and Nobuo Kamiya. Crystal structure of oxygen-evolving photosystem II at a resolution of 1.9 Å. *Nature*, 473(7345):55–60, 2011.

[20] Carina Glöckner, Jan Kern, Matthias Broser, Athina Zouni, Vittal Yachandra, and Junko Yano. Structural changes of the oxygen-evolving complex in photosystem II during the catalytic cycle. *The Journal of Biological Chemistry*, 288(31):22607–20, 2013.

[21] Fluorescent Yield.

[22] Katherine M Davis and Yulia N Pushkar. Structure of the Oxygen Evolving Complex of Photosystem II at Room Temperature. *The Journal of Physical Chemistry B*, 119(8):3492–3498, 2015.

[23] László Gerencsér and Holger Dau. Water oxidation by photosystem II: H2O-D2O exchange and the influence of pH support formation of an intermediate by removal of a proton before dioxygen creation. *Biochemistry*, 49(47):10098–10106, nov 2010.

[24] Junko Yano, Yulia Pushkar, Pieter Glatzel, Azul Lewis, Kenneth Sauer, Johannes Messinger, Uwe Bergmann, and Vittal Yachandra. High-resolution Mn EXAFS of the oxygen-evolving complex in photosystem II: Structural implications for the Mn4Ca cluster. *Journal of the American Chemical Society*, 127(43):14974–14975, 2005.

[25] Dmitriy Shevela and Johannes Messinger. Probing the turnover efficiency of photosystem II membrane fragments with different electron acceptors. *Biochimica et Biophysica Acta*, 1817(8):1208–1212, 2012.

[26] Dimitrios a Pantazis, William Ames, Nicholas Cox, Wolfgang Lubitz, and Frank Neese. Two interconvertible structures that explain the spectroscopic properties of the oxygen-evolving complex of photosystem II in the S2 state. *Angew. Chem. Int. Ed.*, 51(39):9935–9940, 2012.

[27] M Haumann, C Müller, P Liebisch, L Iuzzolino, J Dittmer, M Grabolle, T Neisius, W Meyer-Klaucke, and H Dau. Structural and oxidation state changes of the photosystem II manganese complex in four transitions of the water oxidation cycle (S0 S1, S1 S2, S2 S 3, and S3,4 S0) characterized by X-ray absorption spectroscopy at 20 K and room temperature. *Biochemistry*, 44(6):1894–1908, 2005.

[28] Ivelina Zaharieva, Petko Chernev, Gustav Berggren, Magnus Anderlund, Stenbjörn Styring, Holger Dau, and Michael Haumann. Room-Temperature Energy-Sampling Kβ X-ray Emission Spectroscopy of the Mn4Ca Complex of Photosynthesis Reveals Three Manganese-Centered Oxidation Steps and Suggests a Coordination Change Prior to O2 Formation. *Biochemistry*, 55(30):4197–4211, 2016.

[29] Wenchuan Liang, Theo A Roelofs, Roehl M Cinco, Annette Rompel, Matthew J Latimer, Wa O Yu, Kenneth Sauer, Melvin P Klein, and Vittal K Yachandra. Structural change of the Mn cluster during the S2S3 state transition of the oxygen-evolving complex of photosystem II. Does it reflect the onset of water/substrate oxidation? Determination by Mn X-ray absorption spectroscopy. *Journal of the American Chemical Society*, 122(14):3399–3412, 2000.

[30] Yulia Pushkar, Junko Yano, Kenneth Sauer, Alain Boussac, and Vittal K. Yachandra. Structural changes in the mn(4)ca cluster and the mechanism of photosynthetic water splitting. *Proceedings of the National Academy of Sciences of the United States of America*, 105(PMC2542863):1879–1884, July 2008.

[31] Nicholas Cox, Marius Retegan, Frank Neese, Dimitrios A Pantazis, Alain Boussac, and Wolfgang Lubitz. Electronic structure of the oxygen-evolving complex in photosystem II prior to O-O bond formation. *Science*, 345(6198):804–808, 2014.

[32] Thomas Corry and Patrick J. OMalley. Evidence of o-o bond formation in the final metastable s3 state of natures water oxidizing complex implying a novel mechanism of water oxidation. *J. Phys. Chem. Lett.*, 9(21):6269–6274, November 2018.

[33] Jan Kern, Ruchira Chatterjee, Iris D. Young, Franklin D. Fuller, Louise Lassalle, Mohamed Ibrahim, Sheraz Gul, Thomas Fransson, Aaron S. Brewster, Roberto Alonso-Mori, Rana Hussein, Miao Zhang, Lacey Douthit, Casper de Lichtenberg, Mun Hon Cheah, Dmitry Shevela, Julia Wersig, Ina Seuffert, Dimosthenis Sokaras, Ernest Pastor, Clemens Weninger, Thomas Kroll, Raymond G. Sierra, Pierre Aller, Agata Butryn, Allen M. Orville, Mengning Liang, Alexander Batyuk, Jason E. Koglin, Sergio Carbajo, Sbastien Boutet, Nigel W. Moriarty, James M. Holton, Holger Dobbek, Paul D. Adams, Uwe Bergmann, Nicholas K. Sauter, Athina Zouni, Johannes Messinger, Junko Yano, and Vittal K. Yachandra. Structures of the intermediates of koks photosynthetic water oxidation clock. *Nature*, 563(7731):421–425, November 2018.

[34] Per E. M. Siegbahn. A structure-consistent mechanism for dioxygen formation in photosystem ii. *Chemistry - A European Journal*, 14(27):8290–8302, November 2008.

[35] Fabrice Rappaport, Mireille Blanchard-desce, and Jérôme Lavergne. Kinetics of electron transfer and electrochromic change during the redox transitions of the photosynthetic oxygen-evolving complex. *Biochimica et Biophysica Acta*, 1184:178–192, 1994.

[36] Leonid V Kulik, Boris Epel, Wolfgang Lubitz, and Johannes Messinger. Electronic Structure of the Mn4OxCa Cluster in the S0 and S2 States of the Oxygen-Evolving Complex of Photosystem II Based on Pulse 55 Mn-ENDOR and EPR Spectroscopy. *Journal of the American Chemical Society*, 129(44):13421–13435, 2007.

[37] J Messinger, John H Robblee, Wa On Yu, K Sauer, V K Yachandra, and M P Klein. The S0 State of the Oxygen-Evolving Complex in Photosystem II Is Paramagnetic: Detection of an EPR Multiline Signal. *Journal of the American Chemical Society*, 119(7):11349–11350, 1997.

[38] John H Robblee, Johannes Messinger, Roehl M Cinco, Karen L McFarlane, Carmen Fernandez, Shelly A Pizarro, Kenneth Sauer, and Vittal K Yachandra. The Mn cluster in the S0 state of the oxygen-evolving complex of photosystem II studied by EXAFS spectroscopy: Are there three Di--oxo-bridged Mn2 moieties in the tetranuclear Mn complex? *Journal of the American Chemical Society*, 124(25):7459–7471, 2002.

[39] André Klauss, Michael Haumann, and Holger Dau. Alternating electron and proton transfer steps in photosynthetic water oxidation. *Proceedings of the National Academy of Sciences of the United States of America*, 109(40):16035–16040, 2012.

[40] Long Vo Pham, Julian David Janna Olmos, Petko Chernev, Joanna Kargul, and Johannes Messinger. Unequal misses during the flash-induced advancement of photosystem II: effects of the s state and acceptor side cycles. *Photosynthesis Research*, sep 2018.

[41] Eduardo M. Sproviero, Jos A. Gascn, James P. McEvoy, Gary W. Brudvig, and Victor S. Batista. Quantum mechanics/molecular mechanics study of the catalytic cycle of water splitting in photosystem ii. *J. Am. Chem. Soc.*, 130(11):3428–3442, March 2008.

[42] Per E. M. Siegbahn. Nucleophilic water attack is not a possible mechanism for o-o bond formation in photosystem ii. *Proc Natl Acad Sci USA*, 114(19):4966, May 2017.

[43] Per E M Siegbahn. Water oxidation mechanism in photosystem II, including oxidations, proton release pathways, O-O bond formation and O2 release. *Biochimica et Biophysica Acta*, 1827(8-9):1003–1019, 2013.

[44] Yulia Pushkar, Katherine M. Davis, and Mark C. Palenik. Model of the oxygen evolving complex which is highly predisposed to o-o bond formation. *J. Phys. Chem. Lett.*, 9(12):3525–3531, June 2018.

[45] Takumi Noguchi. Fourier transform infrared difference and time-resolved infrared detection of the electron and proton transfer dynamics in photosynthetic water oxidation. *Biochimica et Biophysica Acta*, 1847:35–45, 2015.

[46] André Klauss, Michael Haumann, and Holger Dau. Seven Steps of Alternating Electron and Proton Transfer in Photosystem II Water Oxidation Traced by Time-Resolved Photothermal Beam Deflection at Improved Sensitivity. *The Journal of Physical Chemistry B*, 119(6):2677–2689, nov 2014.

[47] Ivelina Zaharieva, Holger Dau, and Michael Haumann. Sequential and coupled proton and electron transfer events in the S2S3 transition of photosynthetic water oxidation revealed by time-resolved X-ray absorption spectroscopy. *Biochemistry*, 55(50):acs.biochem.6b01078–acs.biochem.6b01078, dec 2016.

[48] Michael Haumann, Oliver Bgershausen, Dmitry Cherepanov, Ralf Ahlbrink, and Wolfgang Junge. Photosynthetic oxygen evolution: H/d isotope effects and the coupling between electron and proton transfer during the redox reactions at the oxidizing side of photosystem ii. *Photosynthesis Research*, 51(3):193–208, March 1997.

[49] Charles G Barkla. The spectra of the fluorescent Röntgen radiations. *The London, Edinburgh, and Dublin Philosophical Magazine and Journal of Science*, 22(129):396–412, 1911.

[50] P Pfalzer, J P Urbach, M Klemm, S Horn, Marten L DenBoer, Anatoly I Frenkel, and J P Kirkland. Elimination of self-absorption in fluorescence hard-x-ray absorption spectra. *Physical Review B*, 60(13):9335–9339, 1999.

[51] Serena DeBeer George, Patrick Brant, and Edward I. Solomon. Metal and Ligand K-Edge XAS of Organotitanium Complexes: Metal 4p and 3d Contributions to Pre-edge Intensity and Their Contributions to Bonding. *Journal of the American Chemical Society*, 127(2):667–674, 2005.

[52] J. Wong, F. W. Lytle, R. P. Messmer, and D. H. Maylotte. K -edge absorption spectra of selected vanadium compounds. *Physical Review B*, 30(10):5596–5610, 1984.

[53] Frank De Groot, György Vankó, and Pieter Glatzel. The 1s x-ray absorption pre-edge structures in transition metal oxides. *Journal of Physics: Condensed Matter*, 21(21):104207, 2009.

[54] J. J. Rehr and R. C. Albers. Theoretical approaches to x-ray absorption fine structure. *Reviews of Modern Physics*, 72(3):621–654, 2000.

[55] Christopher J Pollock, Mario Ulises Delgado-Jaime, Mihail Atanasov, Frank Neese, and Serena Debeer. Kβ mainline X-ray emission spectroscopy as an experimental probe of metal-ligand covalency. *Journal of the American Chemical Society*, 136(26):9453–9463, 2014.

[56] Mario Ulises Delgado-Jaime, Serena DeBeer, and Matthias Bauer. Valence-to-core x-ray emission spectroscopy of iron-carbonyl complexes: Implications for the examination of catalytic intermediates. *Chem. Eur. J.*, 19(47):15888–15897, October 2013.

[57] György Vankó, Thomas Neisius, Gábor Molnár, Franz Renz, Szilvia Kárpáti, Abhay Shukla, and Frank M F de Groot. Probing the 3D spin momentum with X-ray emission spectroscopy: The case of molecular-spin transitions. *Journal of Physical Chemistry B*, 110(24):11647–11653, 2006.

[58] Hendrik Visser, Elodie Anxolabéhère-Mallart, Uwe Bergmann, Pieter Glatzel, John H Robblee, Stephen P Cramer, J J Girerd, Kenneth Sauer, Melvin P Klein, and Vittal K Yachandra. Mn K-edge XANES and Kß XES Studies of Two Mn-Oxo Binuclear Complexes: Investigation of Three Different OxidationStates Relevant to the Oxygen-Evolving Complex of Photosystem II. *Journal of the American Chemical Society*, 123(29):7031–7039, 2001.

[59] Henry N Chapman, Petra Fromme, Anton Barty, Thomas a White, Richard a Kirian, Andrew Aquila, Mark S Hunter, Joachim Schulz, Daniel P DePonte, Uwe Weierstall, R Bruce Doak, Filipe R N C Maia, Andrew V Martin, Ilme Schlichting, Lukas Lomb, Nicola Coppola, Robert L Shoeman, Sascha W Epp, Robert Hartmann, Daniel Rolles, Artem Rudenko, Lutz Foucar, Nils Kimmel, Georg Weidenspointner, Peter Holl, Mengning Liang, Miriam Barthelmess, Carl Caleman, Sébastien Boutet, Michael J Bogan, Jacek Krzywinski, Christoph Bostedt, Saša Bajt, Lars Gumprecht, Benedikt Rudek, Benjamin Erk, Carlo Schmidt, André Hömke, Christian Reich, Daniel Pietschner, Lothar Strüder, Günter Hauser, Hubert Gorke, Joachim Ullrich, Sven Herrmann, Gerhard Schaller, Florian Schopper, Heike Soltau, Kai-Uwe Kühnel, Marc Messerschmidt, John D Bozek, Stefan P Hau-Riege, Matthias Frank, Christina Y Hampton, Raymond G Sierra, Dmitri Starodub, Garth J Williams, Janos Hajdu, Nicusor Timneanu, M Marvin Seibert, Jakob Andreasson, Andrea Rocker, Olof Jönsson, Martin Svenda, Stephan Stern, Karol Nass, Robert Andritschke, Claus-Dieter Schröter, Faton Krasniqi, Mario Bott, Kevin E Schmidt, Xiaoyu Wang, Ingo Grotjohann, James M Holton, Thomas R M Barends, Richard Neutze, Stefano Marchesini, Raimund Fromme, Sebastian Schorb, Daniela Rupp, Marcus Adolph, Tais Gorkhover, Inger Andersson, Helmut Hirsemann, Guillaume Potdevin, Heinz Graafsma, Björn Nilsson, and John C H Spence. Femtosecond X-ray protein nanocrystallography. *Nature*, 470(7332):73–77, 2011.

[60] A Aquila, A Barty, C Bostedt, S Boutet, G Carini, D DePonte, P Drell, S Doniach, K H Downing, T Earnest, H Elmlund, V Elser, M Gühr, J Hajdu, J Hastings, S P Hau-Riege, Z Huang, E E Lattman, F R N C Maia, S Marchesini, A Ourmazd, C Pellegrini, R Santra, I Schlichting, C Schroer, J C H Spence, I A Vartanyants, S Wakatsuki, W I Weis, and G J Williams. The linac coherent light source single particle imaging road map. *Structural Dynamics*, 2(4):41701, 2015.

[61] T Katayama, T Anniyev, M Beye, R Coffee, M Dell'Angela, A Föhlisch, J Gladh, S Kaya, O Krupin, A Nilsson, D Nordlund, W F Schlotter, J A Sellberg, F Sorgenfrei, J J Turner, W Wurth, H Öström, and H Ogasawara. Ultrafast soft X-ray emission spectroscopy of surface adsorbates using an X-ray free electron laser. *Journal of Electron Spectroscopy and Related Phenomena*, 187:9–14, 2013.

[62] Henrik T Lemke, Christian Bressler, Lin X Chen, David M Fritz, Kelly J Gaffney, Andreas Galler, Wojciech Gawelda, Kristoffer Haldrup, Robert W Hartsock, Hyotcherl Ihee, Jeongho Kim, Kyung Hwan Kim, Jae Hyuk Lee,

Martin M Nielsen, Andrew B Stickrath, Wenkai Zhang, Diling Zhu, and Marco Cammarata. Femtosecond X-ray absorption spectroscopy at a hard X-ray free electron laser: application to spin crossover dynamics. *The Journal of Physical Chemistry A*, 117(4):735–740, 2013.

[63] B K McFarland, J P Farrell, S Miyabe, F Tarantelli, a Aguilar, N Berrah, C Bostedt, J D Bozek, P H Bucksbaum, J C Castagna, R N Coffee, J P Cryan, L Fang, R Feifel, K J Gaffney, J M Glownia, T J Martinez, M Mucke, B Murphy, a Natan, T Osipov, V S Petrović, S Schorb, Th Schultz, L S Spector, M Swiggers, I Tenney, S Wang, J L White, W White, and M Gühr. Ultrafast X-ray Auger probing of photoexcited molecular dynamics. *Nature communications*, 5:4235, 2014.

[64] H Öström, H Öberg, H Xin, J LaRue, M Beye, M Dell'Angela, J Gladh, M L Ng, J A Sellberg, S Kaya, G Mercurio, D Nordlund, M Hantschmann, F Hieke, D Kühn, W F Schlotter, G L Dakovski, J J Turner, M P Minitti, A Mitra, S P Moeller, A Föhlisch, M Wolf, W Wurth, M Persson, J K Nørskov, F Abild-Pedersen, H Ogasawara, L G M Pettersson, and A Nilsson. Probing the transition state region in catalytic CO oxidation on Ru. *Science*, 347(6225):978–982, 2015.

[65] L Young, E P Kanter, B Krässig, Y Li, A M March, S T Pratt, R Santra, S H Southworth, N Rohringer, L F Dimauro, G Doumy, C A Roedig, N Berrah, L Fang, M Hoener, P H Bucksbaum, J P Cryan, S Ghimire, J M Glownia, D A Reis, J D Bozek, C Bostedt, and Messerschmidt. Femtosecond electronic response of atoms to ultra-intense X-rays. *Nature*, 466, 2010.

[66] N Rohringer, D Ryan, R A London, M Purvis, F Albert, J Dunn, J D Bozek, C Bostedt, A Graf, R Hill, S P Hau-Riege, and J J Rocca. Atomic inner-shell X-ray laser at 1.46 nanometres pumped by an X-ray free-electron laser. *Nature*, 481(7382):488–491, 2012.

[67] Hitoki Yoneda, Yuichi Inubushi, Kazunori Nagamine, Yurina Michine, Haruhiko Ohashi, Hirokatsu Yumoto, Kazuto Yamauchi, Hidekazu Mimura, Hikaru Kitamura, Tetsuo Katayama, Tetsuya Ishikawa, and Makina Yabashi. Atomic inner-shell laser at 1.5-ångström wavelength pumped by an X-ray free-electron laser. *Nature*, 524(7566):446–449, 2015.

[68] T Kroll, C Weninger, R Alonso-Mori, D Sokaras, D L Zhu, L Mercadier, V P Majety, A Marinelli, A Lutman, M W Guetg, F J Decker, S Boutet, A Aquila, J Koglin, J Koralek, D P DePonte, J Kern, F D Fuller, E Pastor, T Fransson, Y Zhang, J Yano, V K Yachandra, N Rohringer, and U Bergmann. Stimulated X-Ray Emission Spectroscopy in Transition Metal Complexes. *Physical Review Letters*, 120(13), 2018.

[69] M. Hoener, L. Fang, O. Kornilov, O. Gessner, S. T. Pratt, M. Gühr, E. P. Kanter, C. Blaga, C. Bostedt, J. D. Bozek, P. H. Bucksbaum, C. Buth, M. Chen, R. Coffee, J. Cryan, L. DiMauro, M. Glownia, E. Hosler, E. Kukk, S. R. Leone, B. McFarland, M. Messerschmidt, B. Murphy, V. Petrovic, D. Rolles, and N. Berrah. Ultraintense X-Ray Induced Ionization, Dissociation, and Frustrated Absorption in Molecular Nitrogen. *Physical Review Letters*, 104(25):253002, jun 2010.

[70] L Fang, M Hoener, O Gessner, F Tarantelli, S T Pratt, O Kornilov, C Buth, M Gühr, E P Kanter, C Bostedt, J D Bozek, P H Bucksbaum, M Chen, R Coffee, J Cryan, M Glownia, E Kukk, S R Leone, and N Berrah. Double Core-Hole Production in N2: Beating the Auger Clock. *Physical Review Letters*, 105(8):83005, 2010.

[71] Nora Berrah, Li Fang, Brendan Murphy, Timur Osipov, Kiyoshi Ueda, Edwin Kukk, Raimund Feifel, Peter van der Meulen, Peter Salen, Henning T Schmidt, Richard D Thomas, Mats Larsson, Robert Richter, Kevin C Prince, John D Bozek, Christoph Bostedt, Shin-ichi Wada, Maria N Piancastelli, Motomichi Tashiro, and Masahiro Ehara. Double-core-hole spectroscopy for chemical analysis with an intense X-ray femtosecond laser. *Proceedings of the National Academy of Sciences of the United States of America*, 108(41):16912–16915, 2011.

[72] G Doumy, C Roedig, S K Son, C I Blaga, A D DiChiara, R Santra, N Berrah, C Bostedt, J D Bozek, P H Bucksbaum, J P Cryan, L Fang, S Ghimire, J M Glownia, M Hoener, E P Kanter, B Krässig, M Kuebel, M Messerschmidt, G G Paulus, D A Reis, N Rohringer, L Young, P Agostini, and L F DiMauro. Nonlinear Atomic Response to Intense Ultrashort X Rays. *Physical Review Letters*, 106(8):83002, 2011.

[73] E P Kanter, B Krässig, Y Li, A M March, P Ho, N Rohringer, R Santra, S H Southworth, L F DiMauro, G Doumy, C A Roedig, N Berrah, L Fang, M Hoener, P H Bucksbaum, S Ghimire, D A Reis, J D Bozek, C Bostedt, M Messerschmidt, and L Young. Unveiling and Driving Hidden Resonances with High-Fluence, High-Intensity X-Ray Pulses. *Physical Review Letters*, 107(23):233001, 2011.

[74] H Fukuzawa, S K Son, K Motomura, S Mondal, K Nagaya, S Wada, X J Liu, R Feifel, T Tachibana, Y Ito, M Kimura, T Sakai, K Matsunami, H Hayashita, J Kajikawa, P Johnsson, M Siano, E Kukk, B Rudek, B Erk, L Foucar, E Robert, C Miron, K Tono, Y Inubushi, T Hatsui, M Yabashi, M Yao, R Santra, and K Ueda. Deep inner-shell multiphoton ionization by intense X-ray free-electron laser pulses. *Physical Review Letters*, 110(17):1–5, 2013.

[75] D H Larsson, U Lundstrom, U K Westermark, M Arsenian Henriksson, A Burvall, and H M Hertz. First application of liquid-metal-jet sources for small-animal imaging: high-resolution CT and phase-contrast tumor demarcation. *Med Phys*, 40(2):21909, 2013.

[76] Kenji Tamasaku, Eiji Shigemasa, Yuichi Inubushi, Tetsuo Katayama, Kei Sawada, Hirokatsu Yumoto, Haruhiko Ohashi, Hidekazu Mimura, Makina Yabashi, Kazuto Yamauchi, and Tetsuya Ishikawa. X-ray two-photon absorption competing against single and sequential multiphoton processes. *Nat Photon*, 8(4):313–316, 2014.

[77] Phay J Ho, Christoph Bostedt, Sebastian Schorb, and Linda Young. Theoretical tracking of resonance-enhanced multiple ionization pathways in X-ray free-electron laser pulses. *Physical Review Letters*, 113(25):1–5, 2014.

[78] Jakub Szlachetko, Joanna Hoszowska, Jean-Claude Dousse, Maarten Nachtegaal, Wojciech Błachucki, Yves Kayser, Jacinto Sà, Marc Messerschmidt, Sebastien Boutet, Garth J Williams, Christian David, Grigory Smolentsev, Jeroen A van Bokhoven, Bruce D Patterson, Thomas J Penfold, Gregor

Knopp, Marek Pajek, Rafael Abela, Christopher J Milne, U Keller, I Schuster, K Srinivasan, O Painter, M Hori, P Emma, T Ishikawa, J Amann, L Young, K Tamasaku, G Doumy, N Rohringer, M Beye, S M Vinko, T E Glover, S Shwartz, M Fuchs, M Göppert-Mayer, W Kaiser, C G Garrett, I D Abella, T Plakhotnik, M Albota, B H Cumpston, M Rumi, J W Perry, S A Novikov, A N Hopersky, J Szlachetko, M Kavcic, C J Milne, T J Penfold, M Chergui, M Liang, R D Deslattes, O Ciricosta, N Medvedev, H O Jeschke, B Ziaja, I Badhrees, H J Sánchez, M C Valentinuzzi, C Pérez, J Tulkki, T Aberg, T Sato, A Sytcheva, S Pabst, S K Son, R Santra, H R Varma, M F Ciappina, R Rodriguez, P Lambropoulos, X Tang, F Gelmukhanov, P Sałek, T Privalov, and H Ågren. Establishing nonlinearity thresholds with ultraintense X-ray pulses. *Scientific Reports*, 6, 2016.

[79] Joel N Ullom and Douglas A Bennett. Review of superconducting transition-edge sensors for x-ray and gamma-ray spectroscopy. *Superconductor Science and Technology*, 28(8):84003, 2015.

[80] Tryggve Johansson. Über ein neuartiges, genau fokussierendes Röntgenspektrometer. *Zeitschrift für Physik*, 82(7):507–528, 1933.

[81] H H Johann. Die Erzeugung lichtstarker Rötgenspektren mit Hilfe von Konkavkristallen. *Zeitschrift für Physik*, 69(3):185–206, 1931.

[82] S Huotari, Gy Vankó, F Albergamo, C Ponchut, H Graafsma, C Henriquet, R Verbeni, and G Monaco. Improving the performance of high-resolution X-ray spectrometers with position-sensitive pixel detectors. *Journal of Synchrotron Radiation*, 12:467–472, 2005.

[83] Shinjiro Hayakawa, Akihisa Yamaguchi, Wan Hong, Yohichi Gohshi, Tokujiro Yamamoto, Kouichi Hayashi, Jun Kawai, and Shunji Goto. Wavelength dispersive X-ray spectrometer for small area X-ray fluorescence spectroscopy at SPring-8 BL39XU. *Spectrochimica Acta Part B*, 54(1):171–177, 1999.

[84] L. von Hámos. Röntgenspektroskopie und Abbildung mittels gekrümmter Kristallreflektoren. *Annalen der Physik*, 17(5):716–724, 1933.

[85] J Szlachetko, M Nachtegaal, E de Boni, M Willimann, O Safonova, J Sa, G Smolentsev, M Szlachetko, J A van Bokhoven, J-Cl Dousse, J Hoszowska, Y Kayser, P Jagodzinski, A Bergamaschi, B Schmitt, C David, and A Lücke. A von Hamos x-ray spectrometer based on a segmented-type diffraction crystal for single-shot x-ray emission spectroscopy and time-resolved resonant inelastic x-ray scattering studies. *The Review of scientific instruments*, 83(10):103105, oct 2012.

[86] Hisashi Hayashi, Masaki Kawata, Rumi Takeda, Yasuo Udagawa, Yasuhiro Watanabe, Takeshi Takano, Susumu Nanao, and Naomi Kawamura. A multi-crystal spectrometer with a two-dimensional position-sensitive detector and contour maps of resonant Kβ emission in Mn compounds. *Journal of Electron Spectroscopy and Related Phenomena*, 136(1-2):191–197, 2004.

[87] Ronnie Shepherd, Patrick Audebert, Rex Booth, Bruce Young, Jim Bonlie, Don Nelson, Steve Shiromizu, Dwight Price, Douglas Norman, Jim Dunn, Klaus Widmann, and Paul Springer. Time resolved spectroscopy of ultrashort pulse laser generated x rays using von Hámos crystal spectroscopy. *Review of Scientific Instruments*, 75(10 II):3765–3767, 2004.

[88] Roberto Alonso-Mori, Jan Kern, Richard J Gildea, Dimosthenis Sokaras, Tsu-Chien Weng, Benedikt Lassalle-Kaiser, Rosalie Tran, Johan Hattne, Hartawan Laksmono, Julia Hellmich, Carina Glöckner, Nathaniel Echols, Raymond G Sierra, Donald W Schafer, Jonas Sellberg, Christopher Kenney, Ryan Herbst, Jack Pines, Philip Hart, Sven Herrmann, Ralf W Grosse-Kunstleve, Matthew J Latimer, Alan R Fry, Marc M Messerschmidt, Alan Miahnahri, M Marvin Seibert, Petrus H Zwart, William E White, Paul D Adams, Michael J Bogan, Sébastien Boutet, Garth J Williams, Athina Zouni, Johannes Messinger, Pieter Glatzel, Nicholas K Sauter, Vittal K Yachandra, Junko Yano, and Uwe Bergmann. Energy-dispersive X-ray emission spectroscopy using an X-ray free-electron laser in a shot-by-shot mode. *Proceedings of the National Academy of Sciences of the United States of America*, 109(47):19103–19107, 2012.

[89] Manuel Sanchez del Rio and Roger J Dejus. XOP v2.4 : Recent Developments of The X-ray Optics Software Toolkit. *Proc. SPIE*, 8141:814115, 2011.

[90] K D Finkelstein, D Agyeman-Budu, A Lyndaker, C Pollock, and T Krawczyk. X-ray Emission Collected in a Novel Energy Dispersive Approach. *Journal of Physics: Conference Series*, 493:12033, 2014.

[91] Katherine M Davis, Brian A Mattern, Joseph I Pacold, Taisiya Zakharova, Dale Brewe, Irina Kosheleva, Robert W Henning, Timothy J Graber, Steve M Heald, Gerald T Seidler, and Yulia Pushkar. Fast Detection Allowing Analysis of Metalloprotein Electronic Structure by X-ray Emission Spectroscopy at Room Temperature. *Journal of Physical Chemistry Letters*, 3(14):1858–1864, 2012.

[92] B. a. Mattern, G. T. Seidler, M. Haave, J. I. Pacold, R. a. Gordon, J. Planillo, J. Quintana, and B. Rusthoven. A plastic miniature x-ray emission spectrometer based on the cylindrical von Hamos geometry. *Review of Scientific Instruments*, 83(2):023901, feb 2012.

[93] J I Pacold, J a Bradley, B a Mattern, M J Lipp, G T Seidler, P Chow, Y Xiao, Eric Rod, B Rusthoven, and J Quintana. A miniature X-ray emission spectrometer (miniXES) for high-pressure studies in a diamond anvil cell. *Journal of Synchrotron Radiation*, 19(2):245–251, 2012.

[94] Swarup Chattopadhyay, Robert A Geiger, Guochuan Yin, Daryle H Busch, and Timothy A Jackson. Oxo-and hydroxomanganese(IV) adducts: A comparative spectroscopic and computational study. *Inorganic Chemistry*, 2010.

[95] Domenick F. Leto and Timothy A. Jackson. Mn K-edge X-ray absorption studies of oxo- and hydroxo-manganese(IV) complexes: Experimental and theoretical insights into pre-edge properties. *Inorganic Chemistry*, 53(12):6179–6194, 2014.

[96] Guochuan Yin, James M McCormick, Maria Buchalova, Andrew M Danby, Kent Rodgers, Victor W Day, Kevyn Smith, Chris M Perkins, David Kitko, John D Carter, William M Scheper, and Daryle H Busch. Synthesis, characterization, and solution properties of a novel cross-bridged cyclam manganese(IV) complex having two terminal hydroxo ligands. *Inorganic Chemistry*, 45(20):8052–8061, 2006.

[97] Katherine M Davis, Irina Kosheleva, Robert W Henning, Gerald T Seidler, and Yulia Pushkar. Kinetic modeling of the X-ray-induced damage to a metalloprotein. *Journal of Physical Chemistry B*, 117(31):9161–9169, 2013.

[98] Katherine M Davis, Mark C Palenik, Lifen Yan, Paul F Smith, Gerald T Seidler, G Charles Dismukes, and Yulia N Pushkar. X-ray Emission Spectroscopy of Mn Coordination Complexes Towards Interpreting the Electronic Structure of the Oxygen Evolving Complex of Photosystem II. *The Journal of Physical Chemistry C*, 120(6):3326–3333, 2016.

[99] Xiujuan Wu, Mi Sook Seo, Katherine M Davis, Yong-min Lee, Junying Chen, Kyung-bin Cho, Yulia N Pushkar, and Wonwoo Nam. A Highly Reactive Mononuclear Non-Heme Manganese(IV) À Oxo Complex That Can Activate the Strong C À H Bonds of Alkanes. *J. Am. Chem. Soc*, 50(Iv):20088–20091, 2011.

[100] Lin X. Chen and Xiaoyi Zhang. Photochemical Processes Revealed by X-ray Transient Absorption Spectroscopy. *The Journal of Physical Chemistry Letters*, 4(22):4000–4013, nov 2013.

[101] D. Moonshiram, Y. Pineda-Galvan, D. Erdman, M. Palenik, R. F. Zong, R. Thummel, and Y. Pushkar. Uncovering the role of oxygen atom transfer in ru-based catalytic water oxidation. *Journal of the American Chemical Society*, 138(48):15605–15616, 2016.

[102] Yulia Pushkar, Dooshaye Moonshiram, Vatsal Purohit, Lifen Yan, and Igor Alperovich. Spectroscopic analysis of catalytic water oxidation by [ruii(bpy)(tpy)h2o]2+ suggests that ruv=o is not a rate-limiting intermediate. *Journal of the American Chemical Society*, 136(34):1193811945, 2014.

[103] Dooshaye Moonshiram, Igor Alperovich, Javier J. Concepcion, Thomas J. Meyer, and Yulia Pushkar. Experimental demonstration of radicaloid character in a ruv=o intermediate in catalytic water oxidation. *Proceedings of the National Academy of Sciences*, 110(10):3765–3770, 2013.

[104] J. D. Blakemore, R. H. Crabtree, and G. W. Brudvig. Molecular catalysts for water oxidation. *Chemical Reviews*, 115(23):12974–13005, 2015.

[105] Lianpeng Tong and Randolph P. Thummel. Mononuclear ruthenium polypyridine complexes that catalyze water oxidation. *Chem. Sci.*, 7(11):6591–6603, 2016.

[106] Katherine M Davis, Brendan T Sullivan, Mark Palenik, Lifen Yan, Vatsal Purohit, Gregory Robison, Irina Kosheleva, Robert W Henning, Gerald T Seidler, and Yulia Pushkar. Rapid evolution of the photosystem II electronic structure during water splitting. *Physical Review X*, NA:Accepted, 2018.

[107] Pieter Glatzel and Uwe Bergmann. High resolution 1s core hole X-ray spectroscopy in 3d transition metal complexes - Electronic and structural information. *Coordination Chemistry Reviews*, 249:65–95, 2005.

[108] Christopher J. Pollock and Serena DeBeer. Valence-to-Core X-ray Emission Spectroscopy: A Sensitive Probe of the Nature of a Bound Ligand. *Journal of the American Chemical Society*, 133(14):5594–5601, apr 2011.

[109] Majed Chergui. Time-resolved X-ray spectroscopies of chemical systems: New perspectives. *Structural Dynamics*, 3(3):35–40, 2016.

[110] P Emma, R Akre, J Arthur, R Bionta, C Bostedt, J Bozek, A Brachmann, P Bucksbaum, R Coffee, F J Decker, Y Ding, D Dowell, S Edstrom, A Fisher, J Frisch, S Gilevich, J Hastings, G Hays, P Hering, Z Huang, R Iverson, H Loos, M Messerschmidt, A Miahnahri, S Moeller, H D Nuhn, G Pile, D Ratner, J Rzepiela, D Schultz, T Smith, P Stefan, H Tompkins, J Turner, J Welch, W White, J Wu, G Yocky, and J Galayda. First lasing and operation of an angstrom-wavelength free-electron laser. *Nature Photonics*, 4(9):641–647, 2010.

[111] T Ishikawa, H Aoyagi, T Asaka, Y Asano, N Azumi, T Bizen, H Ego, K Fukami, T Fukui, Y Furukawa, S Goto, H Hanaki, T Hara, T Hasegawa, T Hatsui, A Higashiya, T Hirono, N Hosoda, M Ishii, T Inagaki, Y Inubushi, T Itoga, Y Joti, M Kago, T Kameshima, H Kimura, Y Kirihara, A Kiyomichi, T Kobayashi, C Kondo, T Kudo, H Maesaka, X M Marechal, T Masuda, S Matsubara, T Matsumoto, T Matsushita, S Matsui, M Nagasono, N Nariyama, H Ohashi, T Ohata, T Ohshima, S Ono, Y Otake, C Saji, T Sakurai, T Sato, K Sawada, T Seike, K Shirasawa, T Sugimoto, S Suzuki, S Takahashi, H Takebe, K Takeshita, K Tamasaku, H Tanaka, R Tanaka, T Tanaka, T Togashi, K Togawa, A Tokuhisa, H Tomizawa, K Tono, S K Wu, M Yabashi, M Yamaga, A Yamashita, K Yanagida, C Zhang, T Shintake, H Kitamura, and N Kumagai. A compact X-ray free-electron laser emitting in the sub-angstrom region. *Nature Photonics*, 6(8):540–544, 2012.

[112] E S Kim and M Yoon. Beam Dynamics in a 10-GeV Linear Accelerator for the X-Ray Free Electron Laser at PAL. *IEEE Transactions on Nuclear Science*, 56(6):3597–3606, 2009.

[113] M Altarelli. The European X-ray Free-Electron Laser: toward an ultra-bright, high repetition-rate x-ray source. *High Power Laser Science and Engineering*, 3:e18, 2015.

[114] B D Patterson, R Abela, H H Braun, U Flechsig, R Ganter, Y Kim, E Kirk, A Oppelt, M Pedrozzi, S Reiche, L Rivkin, T Schmidt, B Schmitt, V N Strocov, S Tsujino, and A F Wrulich. Coherent science at the SwissFEL x-ray laser. *New Journal of Physics*, 12:35012, 2010.

[115] Michael Wulff, Anton Plech, Laurent Eybert, Rudolf Randler, Friedrich Schotte, and Philip Anfinrud. The realization of sub-nanosecond pump and probe experiments at the ESRF. *Faraday discussions*, 122:13–26, 2003.

[116] Eric M Dufresne, Bernhard Adams, Dohn A Arms, Matthieu Chollet, Eric C Landahl, Yuelin Li, Donald A Walko, and Jin Wang. TimeResolved Research at the Advanced Photon Source Beamline 7ID. In *AIP Conference Proceedings*, volume 1234, pages 181–184. AIP, 2010.

[117] T Graber, S Anderson, H Brewer, Y S Chen, H S Cho, N Dashdorj, R W Henning, I Kosheleva, G Macha, M Meron, R Pahl, Z Ren, S Ruan, F Schotte, V Srajer, P J Viccaro, F Westferro, P Anfinrud, and K Moffat. BioCARS: a synchrotron resource for time-resolved X-ray science. *Journal of synchrotron radiation*, 18(Pt 4):658–670, 2011.

[118] Adeline Bonvalet, Adeline Darmon, Jean-Christophe Lambry, Jean-Louis Martin, and Patrick Audebert. 1 kHz tabletop ultrashort hard x-ray source for time-resolved x-ray protein crystallography. *Optics Letters*, 31(18):2753–2755, 2006.

[119] Luis Miaja-Avila, Galen C O'Neil, Young I Joe, Bradley K Alpert, Niels H Damrauer, William B Doriese, Steven M Fatur, Joseph W Fowler, Gene C Hilton, Ralph Jimenez, Carl D Reintsema, Daniel R Schmidt, Kevin L Silverman, Daniel S Swetz, Hideyuki Tatsuno, and Joel N Ullom. Ultrafast Time-Resolved Hard X-Ray Emission Spectroscopy on a Tabletop. *Physical Review X*, 6(3):31047, 2016.

[120] Jannick Weisshaupt, Vincent Juvé, Marcel Holtz, ShinAn Ku, Michael Woerner, Thomas Elsaesser, Skirmantas Ališauskas, Audrius Pugžlys, and Andrius Baltuška. High-brightness table-top hard X-ray source driven by sub-100-femtosecond mid-infrared pulses. *Nature Photonics*, 8:927, 2014.

[121] Roberto Alonso-Mori, Jan Kern, Dimosthenis Sokaras, Tsu-Chien Weng, Dennis Nordlund, Rosalie Tran, Paul Montanez, James Delor, Vittal K Yachandra, Junko Yano, Uwe Bergmann, Physical Biosciences Division, and Lawrence Berkeley. A multi-crystal wavelength dispersive x-ray spectrometer. *The Review of scientific instruments*, 83(7):73114, 2012.

[122] L Anklamm, C Schlesiger, W Malzer, D Grotzsch, M Neitzel, and B Kanngiesser. A novel von Hamos spectrometer for efficient X-ray emission spectroscopy in the laboratory. *Review of Scientific Instruments*, 85(5):53110, 2014.

[123] H Legall, H Stiel, M Schnurer, M Pagels, B Kanngiesser, M Muller, B Beckhoff, I Grigorieva, A Antonov, V Arkadiev, and A Bjeoumikhov. An efficient X-ray spectrometer based on thin mosaic crystal films and its application in various fields of X-ray spectroscopy. *Journal of Applied Crystallography*, 42:572–579, 2009.

[124] Franklin D Fuller, Sheraz Gul, Ruchira Chatterjee, E Sethe Burgie, Iris D Young, Hugo Lebrette, Vivek Srinivas, Aaron S Brewster, Tara Michels-Clark, Jonathan A Clinger, Babak Andi, Mohamed Ibrahim, Ernest Pastor, Casper de Lichtenberg, Rana Hussein, Christopher J Pollock, Miao Zhang, Claudiu A Stan, Thomas Kroll, Thomas Fransson, Clemens Weninger, Markus Kubin, Pierre Aller, Louise Lassalle, Philipp Bräuer, Mitchell D Miller, Muhamed Amin, Sergey Koroidov, Christian G Roessler, Marc Allaire, Raymond G Sierra, Peter T Docker, James M Glownia, Silke Nelson, Jason E Koglin, Diling Zhu, Matthieu Chollet, Sanghoon Song, Henrik Lemke, Mengning Liang, Dimosthenis Sokaras, Roberto Alonso-Mori, Athina Zouni, Johannes Messinger, Uwe Bergmann, Amie K Boal, J Martin Bollinger Jr, Carsten Krebs, Martin Högbom, George N Phillips Jr, Richard D Vierstra, Nicholas K Sauter, Allen M Orville, Jan Kern, Vittal K Yachandra, and Junko Yano. Drop-on-demand sample delivery for studying biocatalysts in action at X-ray free-electron lasers. *Nature Methods*, 14:443, 2017.

[125] Scott C Jensen, Katherine M Davis, Brendan Sullivan, Daniel A Hartzler, Gerald T Seidler, Diego M Casa, Elina Kasman, Hannah E Colmer, Allyssa A Massie, Timothy A Jackson, and Yulia Pushkar. X-ray Emission Spectroscopy of Biomimetic Mn Coordination Complexes. *The Journal of Physical Chemistry Letters*, 8(12):2584–2589, 2017.

[126] Matthew Newville, Till Stensitzki, Daniel B. Allen, and Antonino Ingargiola. Lmfit: Non-linear least-square minimization and curve-fitting for python, 2014.

[127] Kenneth P. Burnham and David R. Anderson. Multimodel inference: Understanding aic and bic in model selection. *Sociological Methods & Research*, 33(2):261–304, 2004.

[128] Bliss Forbush, Kok Bessel, and Marion P. McGloin. Cooperation of charges in photosynthetic o2 evolution -ii. damping og flash yield oscillation, deactivation. *Photochemistry and Photobiology*, 14(3):307–321, December 1970.

[129] D J Vinyard, G W Brudvig, M A Johnson, and T J Martinez. Progress Toward a Molecular Mechanism of Water Oxidation in Photosystem II. *Annual Review of Physical Chemistry*, 68:101–116, 2017.

[130] Junko Yano, Jan Kern, Klaus-Dieter Irrgang, Matthew J Latimer, Uwe Bergmann, Pieter Glatzel, Yulia Pushkar, Jacek Biesiadka, Bernhard Loll, Kenneth Sauer, Johannes Messinger, Athina Zouni, and Vittal K Yachandra. X-ray damage to the Mn4Ca complex in single crystals of photosystem II: a case study for metalloprotein crystallography. *Proceedings of the National Academy of Sciences of the United States of America*, 102(34):12047–52, aug 2005.

[131] R Neutze, R Wouts, D van der Spoel, E Weckert, and J Hajdu. Potential for biomolecular imaging with femtosecond X-ray pulses. *Nature*, 406(6797):752–757, 2000.

[132] Anton Barty, Carl Caleman, Andrew Aquila, Nicusor Timneanu, Lukas Lomb, Thomas A White, Jakob Andreasson, David Arnlund, Saša Bajt, Thomas R M Barends, Miriam Barthelmess, Michael J Bogan, Christoph Bostedt, John D Bozek, Ryan Coffee, Nicola Coppola, Jan Davidsson, Daniel P Deponte, R Bruce Doak, Tomas Ekeberg, Veit Elser, Sascha W Epp, Benjamin Erk, Holger Fleckenstein, Lutz Foucar, Petra Fromme, Heinz Graafsma, Lars Gumprecht, Janos Hajdu, Christina Y Hampton, Robert Hartmann, Andreas Hartmann, Günter Hauser, Helmut Hirsemann, Peter Holl, Mark S Hunter, Linda Johansson, Stephan Kassemeyer, Nils Kimmel, Richard A Kirian, Mengning Liang, Filipe R N C Maia, Erik Malmerberg, Stefano Marchesini, Andrew V Martin, Karol Nass, Richard Neutze, Christian Reich, Daniel Rolles, Benedikt Rudek, Artem Rudenko, Howard Scott, Ilme Schlichting, Joachim Schulz, M Marvin Seibert, Robert L Shoeman, Raymond G Sierra, Heike Soltau, John C H Spence, Francesco Stellato, Stephan Stern, Lothar Strüder, Joachim Ullrich, X Wang, Georg Weidenspointner, Uwe Weierstall, Cornelia B Wunderer, and Henry N Chapman. Self-terminating diffraction gates femtosecond X-ray nanocrystallography measurements. *Nature photonics*, 6(1):35–40, 2012.

[133] M N Liang, G J Williams, M Messerschmidt, M M Seibert, P A Montanez, M Hayes, D Milathianaki, A Aquila, M S Hunter, J E Koglin, D W Schafer, S Guillet, A Busse, R Bergan, W Olson, K Fox, N Stewart, R Curtis, A A Miahnahri, and S Boutet. The Coherent X-ray Imaging instrument at the Linac Coherent Light Source. *Journal of Synchrotron Radiation*, 22:514–519, 2015.

[134] V Mariani, A Morgan, C H Yoon, T J Lane, T A White, C O'Grady, M Kuhn, S Aplin, J Koglin, A Barty, and H N Chapman. OnDA: online data analysis and feedback for serial X-ray imaging. *J Appl Crystallogr*, 49(Pt 3):1073–1080, 2016.

[135] D Ratner, C Behrens, Y Ding, Z Huang, A Marinelli, T Maxwell, and F Zhou. Time-resolved imaging of the microbunching instability and energy spread at the Linac Coherent Light Source. *Physical Review Special Topics - Accelerators and Beams*, 18(3), 2015.

[136] D P DePonte, U Weierstall, K Schmidt, J Warner, D Starodub, J C H Spence, and R B Doak. Gas dynamic virtual nozzle for generation of microscopic droplet streams. *Journal of Physics D-Applied Physics*, 41(19), 2008.

[137] D Oberthuer, J Knoska, M O Wiedorn, K R Beyerlein, D A Bushnell, E G Kovaleva, M Heymann, L Gumprecht, R A Kirian, A Barty, V Mariani, A Tolstikova, L Adriano, S Awel, M Barthelmess, K Dorner, P L Xavier, O Yefanov, D R James, G Nelson, D J Wang, G Calvey, Y J Chen, A Schmidt, M Szczepek, S Frielingsdorf, O Lenz, E Snell, P J Robinson, B Sarler, G Belsak, M Macek, F Wilde, A Aquila, S Boutet, M N Liang, M S Hunter, P Scheerer, J D Lipscomb, U Weierstall, R D Kornberg, J C H Spence, L Pollack, H N Chapman, and S Bajt. Double-flow focused liquid injector for efficient serial femtosecond crystallography. *Scientific Reports*, 7, 2017.

[138] P Hart, S Boutet, G Carini, M Dubrovin, B Duda, D Fritz, G Haller, R Herbst, S Herrmann, C Kenney, N Kurita, H Lemke, M Messerschmidt, M Nordby, J Pines, D Schafer, M Swift, M Weaver, G Williams, D L Zhu, N Van Bakel, and J Morse. The CSPAD megapixel x-ray camera at LCLS. *X-Ray Free-Electron Lasers: Beam Diagnostics, Beamline Instrumentation, and Applications*, 8504, 2012.

[139] G Blaj, P Caragiulo, G Carini, A Dragone, G Haller, P Hart, J Hasi, R Herbst, C Kenney, B Markovic, K Nishimura, J Pines, J Segal, C Tamma, and A Tomada. Future of ePix detectors for high repetition rate FELs. *AIP Conf. Proc. Appl. Phys. Lett*, 1741(334):40012–40099, 2016.

[140] C A Glasbey and K V Mardia. A review of image-warping methods. *Journal of Applied Statistics*, 25(2):155–171, 1998.

[141] S.-K. Son Z. Jurek, R. Santra and B. Ziaja. Xraypac – a software package for modeling x-ray-induced dynamics of matter, v. 1.01. CFEL, DESY, 2017.

[142] Sang-Kil Son, Linda Young, and Robin Santra. Impact of hollow-atom formation on coherent x-ray scattering at high intensity. *Physical Review a*, 83(3), 2011.

[143] Z Jurek, S K Son, B Ziaja, and R Santra. XMDYN and XATOM: versatile simulation tools for quantitative modeling of X-ray free-electron laser induced dynamics of matter. *Journal of Applied Crystallography*, 49:1048–1056, 2016.

[144] M G Makris, P Lambropoulos, and A Mihelic. Theory of Multiphoton Multielectron Ionization of Xenon under Strong 93-eV Radiation. *Physical Review Letters*, 102(3), 2009.

[145] N Rohringer and R Santra. X-ray nonlinear optical processes using a self-amplified spontaneous emission free-electron laser. *Physical Review a*, 76(3), 2007.

[146] F B Rosmej, R Dachicourt, B Deschaud, D Khaghani, M Dozières, and M Šmíd. Exotic x-ray emission from dense plasmas. *Journal of Physics B: Atomic, Molecular and Optical Physics*, 48(22):224005, 2015.

[147] D A Berthold, G T Babcock, and C F Yocum. A highly resolved oxygen-evolving photosystem II preparation from spinach thylakoid membranes. *FEBS Letters*, 134:231–234, 1981.

APPENDICES

A. Preparation of Photosystem II

This gives a step by step preparation for isolating PSII enriched thykaloid membranes from spinach. This is adapted from earlier work by by Berthold, Babcock and Yacom [147].

A.1 Buffers

Grind Buffer - 1600mL at pH 7.5

  1 mM EDTA

  50 mM HEPES (Bio Buffer)

  4 mM MgCl2•6H2O

  0.4 M NaCl

  Add shortly before use

  5 mM Sodium Ascorbate

  2 mg / mL BSA

Wash Buffer - 800 mL at pH 6.0

  50 mM MES (Bio Buffer)

  8 mM MgCl2•6H2O

  0.15 M NaCl

Resuspension/Incubation - Buffer 800mL at pH 6.0

  5 mM CaCl2•2H2O

  50 mM MES (Bio Buffer)

  10 mM MgCl2•6H2O

  15 mM NaCl

Sucrose Buffer - 600mL at pH 6.0

  5 mM CaCl2•2H2O

50 mM MES (Bio Buffer)

5 mM MgCl2•6H2O

15 mM NaCl

0.4 M Sucrose

A.2   Procedure

A) Blend leaves and grind buffer in a Waring blender with three short bursts on medium and grinding on low for ten seconds.

B) Filter the resulting suspension through 4 layers of cheesecloth. Squeeze the fibrous mass to maximize the volume of extracted liquid. Then use 2 layers of nylon to filter the smaller particles.

C) Centrifuge at 8000g for 10 minutes, then discard supernatant.

D) Using paintbrushes, quickly resuspend chloroplast pellet in wash buffer making sure that the pellet doesn't have any particulates unsuspended (speed is necessary to minimize exposure to free proteases).

E) Centrifuge at 8000g for 10 minutes, then discard supernatant.

F) Resuspend thylakoid pellet using minimal amounts of resuspension/incubation buffer and homogenize the suspension thoroughly and transfer to graduated cylinder. Measure volume.

G) Using the UV-Vis spectra, determine the chlorophyll concentration and total mass in the sample. Add Triton X100 to make a 25:1 chlorophyll mass ratio. Dilute with resuspension/incubation butter to obtain a chlorophyll concentration of 2mg/mL.

H) Allow the Triton to stir for 30 minutes to reduce the PSI content.

I) Centrifuge at 36600g for 15 minutes, then discard supernatant.

J) Resuspend the chlorophyll concentrated pellet (green) resuspension/incubation buffer and leave the white starches behind.

K) Centrifuge at 1000g for 2 minutes, then discard pellet.

L) Centrifuge at 36600g for 30 minutes, then discard supernatant.

M) Resuspend the chlorophyll concentrated pellet in resuspension/incubation buffer and leave the white starches behind.

N) Centrifuge at 36600g for 10 minutes, then discard supernatant.

O) Resuspend in the Sucrose buffer, use the UV-Vis spectra to determine the chlorophyll concentration and total mass in the sample. Extract sample for an oxygen evolution measurement.

P) Centrifuge at 36600g for 20 minutes, then discard supernatant. Store tube wrapped in Al foil in the -80c freezer.

Q) From one of the tubes extract sample for EPR to measure if any S2 multi-line signal is visible. The EPR sample is then exposed for 30min to high intensity light, while in a dry ice cooled ethanol bath, to transition to S2 after the initial measurement.

R) Oxygen evolution is done using a Clark type electrode. Turnover rates are determined though a calibration of the air saturated and depleted (adding hydrosulfate) water.

B. DFT Coordinates

Table B.1.: DFT Coordinates for $Mn^{IV}(OH)_2(Me_2EBC)]^{2+}$

Mn	-0.02694	-0.02973	-0.60239
O	0.357139	-1.3878	-1.72995
H	0.376889	-1.22379	-2.69183
O	-0.45909	1.207503	-1.84814
H	-0.49712	0.943376	-2.78719
N	-2.0167	-0.80317	-0.44425
N	-0.3469	1.522408	0.827025
N	0.339159	-1.26093	1.097846
N	2.084193	0.640485	-0.45748
C	-2.62574	-1.01403	-1.79509
H	-1.94857	-1.611	-2.4127
H	-3.57812	-1.55469	-1.67865
H	-2.82166	-0.04855	-2.27258
C	2.500248	1.020357	-1.84904
H	3.527816	1.414293	-1.82402
H	2.477691	0.13358	-2.49281
H	1.824034	1.783422	-2.24656
C	-2.95866	0.052863	0.369516
H	-3.9787	-0.2934	0.137113
H	-2.79535	-0.15474	1.434296
C	-1.81025	-2.14476	0.199966
H	-2.78699	-2.58544	0.46244

H	-1.33486	-2.79138	-0.54881
C	-2.836	1.54152	0.070105
H	-3.76136	2.034095	0.406171
H	-2.78349	1.699492	-1.01472
C	-0.93914	-2.0029	1.429716
H	-1.46175	-1.45259	2.222444
H	-0.69425	-2.99046	1.848531
C	3.082548	-0.38916	0.068361
H	4.004385	-0.27454	-0.52065
H	3.349145	-0.11642	1.09795
C	2.629589	-1.83937	-0.01396
H	3.494181	-2.4574	0.276111
H	2.401372	-2.09429	-1.05444
C	1.458499	-2.26634	0.886914
H	1.00197	-3.15987	0.44334
H	1.815816	-2.54545	1.892499
C	2.102455	1.872403	0.417121
H	2.459348	1.595771	1.415705
H	2.828605	2.599595	0.020586
C	0.735984	2.517934	0.491501
H	0.460462	2.951936	-0.47765
H	0.739516	3.326868	1.24185
C	0.67556	-0.33595	2.233443
H	0.527222	-0.85911	3.193645
H	1.739883	-0.10046	2.177438
C	-0.19037	0.920363	2.2041
H	0.213438	1.674105	2.900623
H	-1.19893	0.681318	2.562327
C	-1.67355	2.270156	0.755526

| H | -1.94207 | 2.543725 | 1.787262 |
| H | -1.49482 | 3.207535 | 0.215643 |

Table   B.2.:   DFT   Coordinates   for [Mn^{IV}(O)(OH)(Me$_2$EBC)]$^+$

Mn	-0.04168	-0.02517	-0.6524
O	0.367911	-1.45519	-1.73169
H	0.247588	-1.13405	-2.64649
O	-0.42067	1.058098	-1.87088
N	-2.00213	-0.81	-0.45126
N	-0.36119	1.560354	0.811974
N	0.342142	-1.23747	1.174209
N	2.066933	0.638792	-0.50671
C	-2.58422	-1.06923	-1.80084
H	-1.92981	-1.75909	-2.34192
H	-3.58715	-1.51488	-1.69243
H	-2.64393	-0.12762	-2.35672
C	2.469119	0.961001	-1.91043
H	3.478279	1.40596	-1.91628
H	2.475262	0.03545	-2.49759
H	1.733913	1.642536	-2.35169
C	-2.95092	0.072602	0.311212
H	-3.97432	-0.27044	0.084139
H	-2.79928	-0.09195	1.3868
C	-1.79709	-2.11745	0.249693
H	-2.7721	-2.56667	0.510727
H	-1.29214	-2.77762	-0.46794

C	-2.79816	1.550224	-0.03845
H	-3.74346	2.066775	0.1915
H	-2.62418	1.653628	-1.11778
C	-0.94224	-1.94171	1.496055
H	-1.48037	-1.35536	2.25416
H	-0.74016	-2.92295	1.956348
C	3.05848	-0.36936	0.054562
H	3.981131	-0.2913	-0.54154
H	3.335109	-0.05717	1.071478
C	2.597299	-1.82373	0.042336
H	3.473362	-2.43787	0.307514
H	2.306411	-2.09459	-0.9791
C	1.461574	-2.22794	1.003228
H	1.017029	-3.15183	0.609975
H	1.860077	-2.46451	2.007449
C	2.080746	1.893241	0.323139
H	2.454137	1.652209	1.326546
H	2.789664	2.623266	-0.10194
C	0.707486	2.531824	0.410478
H	0.407162	2.903081	-0.57804
H	0.739458	3.380566	1.11886
C	0.675681	-0.26682	2.255611
H	0.545793	-0.73333	3.250771
H	1.738232	-0.02617	2.172845
C	-0.18317	0.999084	2.191918
H	0.234524	1.762458	2.873389
H	-1.18708	0.769225	2.571553
C	-1.68915	2.285008	0.72131
H	-2.01606	2.51936	1.747451

H   -1.51599   3.246642   0.222026